Max-Planck-Institut für Meteorologie
Max Planck Institute for Meteorology

MAX-PLANCK-GESELLSCHAFT

Towards the Assessment of the Aerosol Radiative Effects A Global Modelling Approach

Philip Stier

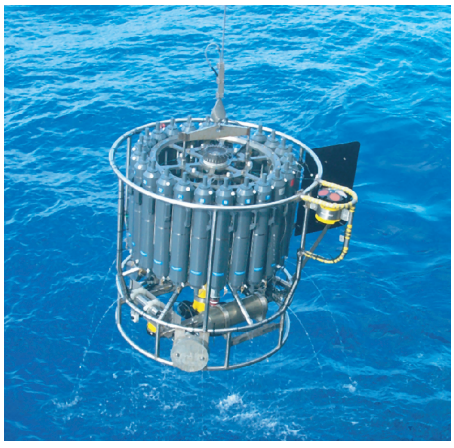

Berichte zur Erdsystemforschung 9/2005

Reports on Earth System Science

Hinweis

Die Berichte zur Erdsytemforschung werden vom Max-Planck-Institut für Meteorologie in Hamburg in unregelmäßiger Abfolge herausgegeben.

Sie enthalten wissenschaftliche und technische Beiträge, inklusive Dissertationen.

Die Beiträge geben nicht notwendigerweise die Auffassung des Instituts wieder.

Die "Berichte zur Erdsystemforschung" führen die vorherigen Reihen "Reports" und "Examensarbeiten" weiter.

Notice

The Reports on Earth System Science are published by the Max Planck Institute for Meteorology in Hamburg. They appear in irregular intervals.

They contain scientific and technical contributions, including Ph. D. theses.

The Reports do not necessarily reflect the opinion of the Institute.

The "Reports on Earth System Science" continue the former "Reports" und "Examensarbeiten" of the Max Planck Institute.

Anschrift / Address

Max-Planck-Institut für Meteorologie
Bundesstrasse 53
20146 Hamburg
Deutschland

Tel.: +49-(0)40-4 11 73-0
Fax: +49-(0)40-4 11 73-298
Web: www.mpimet.mpg.de

Layout:

Bettina Diallo, PR & Grafik

Titelfotos:
vorne:
Christian Klepp - Jochem Marotzke - Christian Klepp
hinten:
Katsumasa Tanaka - Christian Klepp - Clotilde Dubois

Berichte zur Erdsytemforschung 9/2005

Ein globaler Modellierungsansatz zur Abschätzung der Aerosol-Strahlungseffekte

Towards the Assessment of the Aerosol Radiative Effects A Global Modelling Approach

Dissertation zur Erlangung des Doktorgrades der Naturwissenschaften
im Fachbereich Geowissenschaften der Universität Hamburg
vorgelegt von

Philip Stier
aus München

Hamburg 2004

Reports on Earth System Science 9/2005

ISSN 1614-1199

Philip Stier
Max-Planck-Institut für Meteorologie
Bundesstrasse 53
20146 Hamburg
Germany

Als Dissertation angenommen
vom Fachbereich Geowissenschaften der Universität Hamburg

auf Grund der Gutachten von
Prof. Dr. Hartmut Graßl
und
Dr. Johann Feichter

Hamburg, den 2. Februar 2005
Professor Dr. Helmut Schleicher
Dekan des Fachbereiches Geowissenschaften

ISSN 1614-1199

Towards the Assessment of the Aerosol Radiative Effects
A Global Modelling Approach

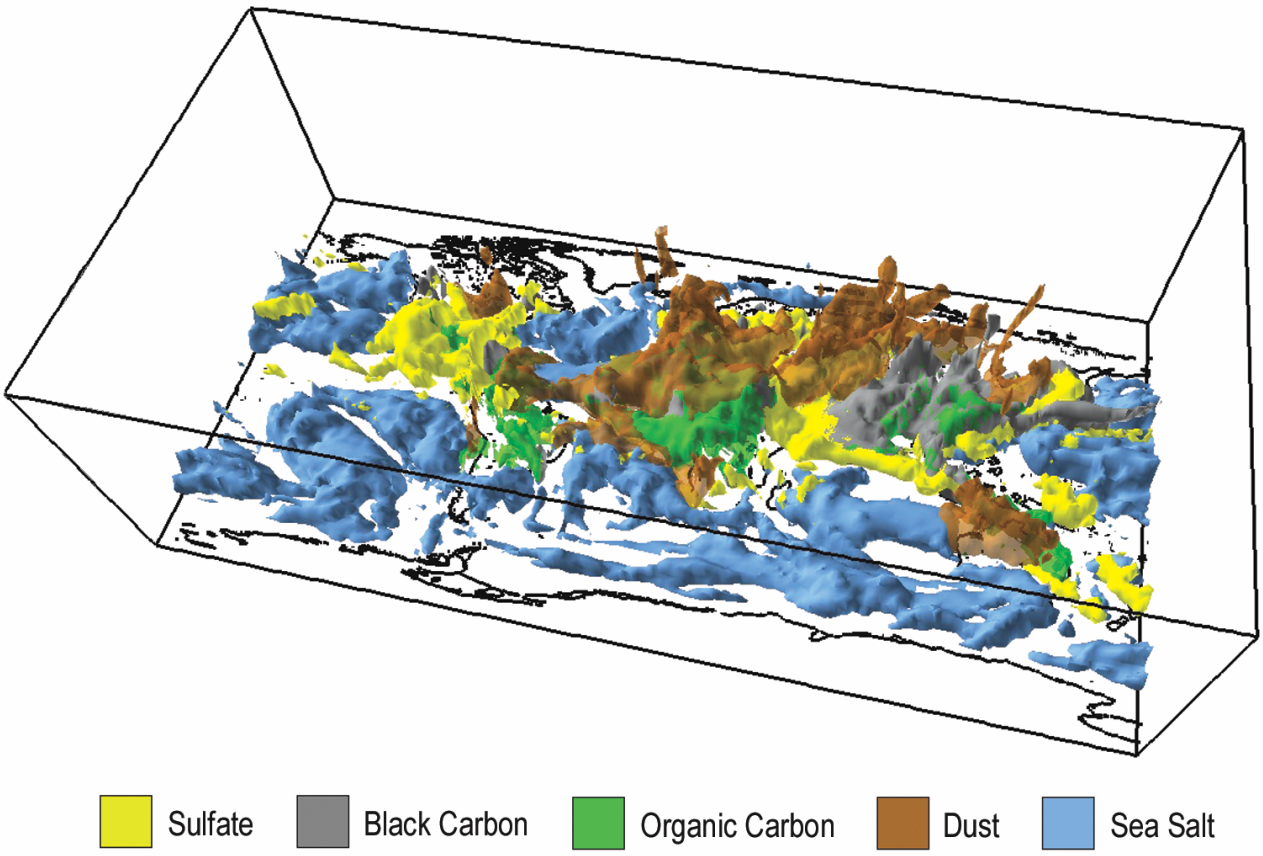

Philip Stier

Hamburg 2004

Contents

Abstract

Aerosols play an important role in the global climate system. However, their effects on the radiation budget and even their global distribution and composition are not understood satisfactorily. The objective of this study is to advance the understanding about the global tropospheric aerosol system as basis for higher accuracy estimates of the anthropogenic aerosol effects.
In traditional global aerosol models, aerosol size-distribution and mixing-state are prescribed. This limits local representation and applicability to different climatic regimes. To overcome these deficiencies, the global aerosol-climate model ECHAM5-HAM has been developed. In the aerosol module HAM, the aerosol distribution is represented by an ensemble of interacting internally and externally-mixed log-normal aerosol modes with prognostic treatment of aerosol size-distribution, mixing-state, and composition. In the current setup, the major global aerosol compounds sulfate (SU), black carbon (BC), particulate organic matter (POM), sea salt (SS), and mineral dust (DU) are included. The simulated global annual-mean aerosol burden (life-time) for the year 2000 are for SU: 0.80 Tg(S) (3.9 days), for BC: 0.11 Tg (5.4 days), for POM: 0.99 Tg (5.4 days), for SS: 10.5 Tg (0.8 days), and for DU: 8.28 Tg (4.6 days). An extensive evaluation with in-situ and remote sensing measurements underscores that the model results are generally in good agreement with observations of the global aerosol system. The simulated global annual-mean aerosol optical depth (AOD) is at 0.14 in excellent agreement with an estimate derived from AERONET sun-photometer measurements (0.14) and a composite derived from MODIS-MISR satellite retrievals (0.16). Although on a regional basis the differences are not negligible, the main patterns of aerosol optical depth are reproduced.
The response to changes in anthropogenic emissions was analysed in a series of simulations with ECHAM5-HAM. Traditionally, additivity is assumed in the assessment of the aerosol climate impact as the underlying bulk aerosol models are largely constrained to linearity. HAM establishes degrees of freedom for non-linear responses of the aerosol system. Simulated aerosol column mass burdens respond non-linearly to changes in anthropogenic emissions, manifested in alterations of the aerosol life-times. Specific emission changes induce modifications of aerosol cycles with unaltered emissions, indicating a microphysical coupling of the aerosol cycles. The additivity of the aerosol system is analysed by comparing the response of a simulation with emission changes to several compounds with the total of the responses of individual simulations in each of which one of the emission changes was introduced. Close to the anthropogenic source regions, deviations from additivity are found at up to 30 % and 15 % for the accumulation mode number burden and aerosol optical thickness, respectively. The results challenge the traditional approach of assessing the climate impact of aerosols separately for each component and demand for integrated assessments and emission strategies.
First applications of ECHAM5-HAM towards the assessment of the aerosol radiative effects are presented. A measure of radiative perturbations (P_L), similar to instantaneous forcing on the large-scale but with degrees of freedom to locally adjust to feedback processes, is introduced. The total anthropogenic direct and semi-direct radiative perturbation P_L is negative with global annual-mean values for clear-sky of -0.49 $W\,m^{-2}$ and for total-sky of -0.12 $W\,m^{-2}$.
As basis for the assessment of the indirect aerosol effects, an extended microphysical parameterisation for stratiform clouds has been introduced into ECHAM5-HAM and coupled to the aerosol system via two optional activation schemes. The preliminary evaluation of the simulated cloud parameters shows generally a good agreement with satellite retrieved cloud data. Further sensitivity studies and an extensive evaluation are required before quantitative conclusions on the indirect aerosol radiative effects can be drawn.

Zusammenfassung

Aerosole spielen eine bedeutende Rolle im globalen Klimasystem. Dennoch ist ihr Effekt auf die globale Strahlungsbilanz sowie die globale Verteilung und Zusammensetzung nur unzureichend verstanden. Zielsetzung dieser Studie ist es, das Verständnis des globalen troposphärischen Aerosolsystems, als Basis für präzisere Abschätzungen der anthropogenen Aerosoleffekte, zu verbessern.

In traditionellen globalen Aerosolmodellen werden die Aerosolgrössenverteilung und der Aerosolmischungszustand vorgeschrieben. Um diese Defizite zu beheben, wurde das globale Aerosol-Klimamodell ECHAM5-HAM entwickelt. Im Aerosolmodul HAM ist die Aerosolverteilung durch ein Ensemble aus interaktiven, intern und extern gemischten, log-normalen Aerosolmoden repräsentiert, mit prognostischer Behandlung der Aerosolgrössenverteilung, des Mischungszustandes und der Zusamensetzung. Die derzeitige Modellkonfiguration beinhaltet die wichtigsten globalen Aerosolkomponenten Sulfat (SU), Ruß (BC), partikuläre organische Kohlenstoffverbindungen (POM), Seesalz (SS) und Mineralstaub (DU). Die simulierten globalen jährlichen Aerosolmassen (atmosphärischen Verweildauern) für das Jahr 2000 sind für SU: 0,80 Tg(S) (3,9 Tage), für BC: 0,11 Tg (5,4 Tage), für POM: 0,99 Tg (5,4 Tage), für SS: 10,5 Tg (0,8 Tage) und für DU: 8,28 Tg (4,6 Tage). Eine umfangreiche Evaluierung mit In-situ- und Fernerkundungsmessungen zeigt, dass die Modellergebnisse im Allgemeinen in guter Übereinstimmung mit Beobachtungen des globalen Aerosolsystems sind. Das simulierte Jahresmittel der Aerosol-Optischen-Dicke (AOD) stimmt mit 0,14 exzellent mit einer Abschätzung aus AERONET Sonnenphotometermessungen (0,14) und einer aus MODIS-MISR Satellitenauswertungen abgeleiteten Kompilation (0,16) überein. Obwohl die Differenzen auf regionaler Basis nicht vernachlässigbar sind, werden die wesentlichen Muster der Aerosol-Optischen-Dicke reproduziert.

Die Reaktion auf Modifikationen anthropogener Emissionen wurde in einer Serie von Sensitivitätsstudien mit ECHAM5-HAM untersucht. Herkömmlicherweise wird in der Abschätzung der klimatischen Effekte von Aerosolen Additivität angenommen, da die zugrundeliegenden Aerosolmodelle weitgehend auf Linearität beschränkt sind. HAM hingegen etabliert Freiheitsgrade für nichtlineare Reaktionen des Aerosolsystems. Die simulierten Aerosolmassen reagieren nichtlinear auf Modifikationen anthropogener Emissionen, aufgezeigt durch Änderungen der atmosphärischen Verweildauer. Emissionsänderungen induzieren Modifikationen in Aerosolzyklen deren Emissionen unverändert sind, ein Indiz für eine mikrophysikalische Koppelung der Aerosolzyklen.

Die Additivität des Aerosolsystems wurde durch einen Vergleich der Reaktion einer Simulation mit Emissionsänderungen von mehreren Komponenten, mit der Summe der Reaktionen von einzelnen Simulationen, in denen jeweils eine der Emissionsänderungen eingebracht wurde, analysiert. In der Umgebung der anthropogenen Quellgebiete erreichen die Abweichungen von Additivität bis zu 30 % für die Akkumulationsmodus-Teilchenanzahl und 15 % für die Aerosol-Optische-Dicke. Die Ergebnisse stellen den traditionellen Ansatz der Betrachtung des klimatologischen Effektes von Aerosolen, separat für jede Komponente, in Frage und verlangen nach integrativen Betrachtungen und Emissionsstrategien.

Erste Anwendungen von ECHAM5-HAM zur Bewertung der Aerosolstrahlungseffekte werden präsentiert. Ein Maß für Strahlungsperturbation (P_L), angelehnt an "instantaneous Forcing", aber mit Freiheitsgraden für lokale Anpassungen an Rückkoppelungsprozesse, wird definiert. Die totale anthropogene direkte und semi-direkte Strahlungsperturbation P_L ist negativ, mit einem jährlichen globalen Mittelwert -0,49 $\mathrm{W\,m^{-2}}$ im unbewölkten und -0,12 $\mathrm{W\,m^{-2}}$ im bewölkten Fall.

Als Grundlage für die Analyse der indirekten Aerosoleffekte wurde eine erweiterte mikrophysikalische Parametrisierung für stratiforme Wolken in ECHAM5 eingeführt und mittels zweier optionaler Aktivierungsschemata an das Aerosolsystem gekoppelt. Die vorläufige Evaluierung der simulierten Wolkenparameter zeigt im Allgemeinen eine gute Übereinstimmung mit satellitenabgeleiteten Wolkendaten. Weitere Sensitivitätsstudien und eine intensive Evaluierung sind notwendig, bevor quantitative Aussagen über die indirekten Aerosoleffekte getroffen werden können.

Chapter 1

Introduction

Aerosol is defined as a suspension in air of liquid or solid particles. Atmospheric aerosol particles origin from a variety of natural and anthropogenic sources. Aerosol particles are either emitted in particulate form, referred to as primary aerosol, or formed in the atmosphere via gas-to-particle conversion, referred to as secondary aerosol. The size of atmospheric aerosol particles ranges from secondary-produced molecular clusters in the nanometer range to primary particles of several tens of micrometers. The main components of atmospheric aerosols are mineral soil dust, sea salt, carbonaceous aerosols, sulfates, ammonium, and nitrates. Atmospheric aerosols play an important role in the earth system and are one of the major uncertainties in the assessment of climate change.
In this chapter, a brief review of the current knowledge about the global aerosol system is given. The relevant aerosol sources, transformation processes, and sinks are discussed and the importance of aerosols for the various compartments of the earth system is highlighted. Based on a discussion of the representation of these processes in previous global aerosol models, the need for advanced models for the assessment of the aerosol effects is demonstrated. This motivates the development of a microphysical global aerosol-climate model with realistic representation of the aerosol system. The objectives of this study are discussed and their accomplishment throughout this study are outlined.

1.1 Sources of Atmospheric Aerosols

The main aerosol production mechanisms are combustion processes, wind-driven emissions of suspendable particles from land surfaces, wind-driven emission of evaporating droplets from the ocean surface, and the emission of gaseous aerosol precursors. In the following, an overview over the relevant aerosol sources is given. A quantitative description of a state of the art emission estimate for the year 2000 is discussed in Section 2.2.3 and summarised in Table 2.2.

Mineral soil dust is emitted by wind-driven mobilisation of erodible soil dust particles. Estimates of the global annual dust source are highly uncertain and lie in the range of $1000 - 5000\ \mathrm{Tg\,yr^{-1}}$ (Raes et al., 2000; Penner et al., 2001). The main source regions are deserts, dry lakes and river beds, and arid zones with anthropogenically disturbed vegetation. When the surface friction velocity exceeds a minimum threshold, particles with radii $r < 30\ \mu$m become suspended in air and transported upwards by turbulent eddies (Bagnold, 1941; Marticorena and Bergametti, 1995). Recent estimates attribute approximately $10 - 60$ % of the current total dust emissions to the contribution of anthropogenically disturbed soils (Sokolik and Toon, 1996; Wolf and Hidy,

1997; Mahowald and Luo, 2003; Tegen et al., 2004).

Sea salt aerosol is produced by wind-induced formation of sea spray and its subsequent (partly) evaporation. Global estimates of the annual sea salt source depend crucially on the assumed upper cut-off of the emission size distribution and lie therefore in the wide range of $1000 - 30000\ \mathrm{Tg\,yr^{-1}}$ (Raes et al., 2000; Schulz et al., 2004). The main sea salt production mechanisms are the evaporation of film and jet droplets caused by bubble bursting and, at high wind speeds, by the evaporation of droplets displaced from the wave tops. Sea salt aerosol is a natural component of the global aerosol system with negligible anthropogenic impacts.

Carbonaceous aerosols can be subdivided into two major groups. Organic carbonaceous aerosols, often referred to as particulate organic matter (POM) are the dominant contributor and origin from diverse primary and secondary sources. Elemental carbon, often referred to as black carbon (BC), origins from incomplete combustion processes. The largest source of carbonaceous aerosols are combustion processes from vegetation fires and the burning of biomass, such as fossil-fuels, bio-fuels and agricultural waste. In combustion processes POM and BC are typically co-emitted and form agglomerates of small spherical particles, referred to as soot (c.f. Figure 1.1). Secondary organic aerosols (SOA) are formed from the atmospheric oxidation of hydrocarbons yielding compounds with low volatility. At suitable atmospheric conditions these volatile organic carbons (VOC) condensate on pre-existing aerosol particles. However, measurements and theory indicate that organic vapours may also play an important role in the nucleation of new aerosol particles (Marti et al., 1997; Kulmala et al., 2004). The dominant precursors of secondary organic aerosols are biogenic VOC attributable to the group of mono-terpenes. However, several thousand VOC have been identified and the yields of SOA via complex chemical pathways are highly uncertain (Kanakidou et al., 2004). Actual global estimates of the SOA formation lie in the range of $12 - 70\ \mathrm{Tg\,yr^{-1}}$ (Kanakidou et al., 2004). A number of other primary organic aerosols sources are known. Pollen, bacteria, and plant debris could contribute substantially to the organic aerosol mass (Jaenicke and Matthias-Maser, 1993; Wiedinmyer et al., 2004) and are potentially of importance as ice nuclei (Carney et al., 1975; Maki and Willoughby, 1978). Oceanic biogeochemistry produces surface-active organic compounds that could become suspended in air via bubble bursting effects (Blanchard and Syzdek, 1970; O'Dowd et al., 2004). However, quantitative estimates of the source distribution are yet to be established.

Sulfate is produced in the atmosphere by chemical reactions from gaseous precursors. The main anthropogenic precursor of sulfate is SO_2 from fossil-fuel use, industry and bio-fuels. The main natural precursors are SO_2 from volcanic sources and dimethyl sulfide (DMS) from biogenic sources. The predominant contribution of DMS is produced by the marine biosphere and emitted wind-driven from the ocean surface. There are various pathways for the conversions of the precursors into sulfate. A fraction of SO_2 is removed from the atmosphere before oxidation, a fraction is oxidised to sulfate in the gas phase and another fraction is oxidised to sulfate in cloud droplets and then partly removed by rain-out and partly evaporated as aerosol. There are few observational constraints on the partitioning among these processes on the global scale, so that it has to be estimated from global models of the sulfur cycle. In an intercomparison of 11 global sulfate models, in average 42 % of the emitted SO_2 are deposited, 12 % are oxidised in the gas phase and 45 % are oxidised in the aqueous phase (Penner et al., 2001). The main oxidation pathways of SO_2 to sulfate are the OH oxidation in the gas phase and the oxidation by H_2O_2 and O_3 in the aqueous phase (e.g. Seinfeld and Pandis (1998)). DMS reacts in the gas phase with the OH radical and other partners, most importantly the NO_3 and bromide oxide (BrO) radicals, yielding SO_2, methanesulfonic acid (MSA), and dimethylsulphoxide (DMSO). The exact pathways are still uncertain (Pham et al., 1995; Boucher et al., 2003).

The form of sulfate in the aerosols depends on the environmental conditions. With increasing availability of gaseous ammonia, sulfate is neutralised from sulfuric acid (H_2SO_4) to intermediate compounds, such as ammonium bisulfate (NH_4HSO_4), to ammonium sulfate ($(NH_4)_2SO_4$). The global annual source for ammonium is estimated as 34 $Tg\,yr^{-1}$ (Adams et al., 1999).
Nitrate aerosols are formed in ammonia rich conditions with abundances of ammonia in excess to neutralise all sulfuric acid to ammonium sulfate, the preferred form of sulfate. The excess of ammonia is available to form ammonium nitrate (NH_4NO_3) aerosols. In ammonia poor conditions, there is insufficient ammonia to neutralise the available sulfate to ammonium sulfate. Therefore, no excess ammonia is available to form ammonium nitrate (e.g. Seinfeld and Pandis (1998)). The global annual source of nitrate is estimated as 11 $Tg\,yr^{-1}$ (Raes et al. (2000), estimated from Adams et al. (1999)).
The heterogeneity of aerosol particles from primary and secondary sources is pictured in Figure 1.1.

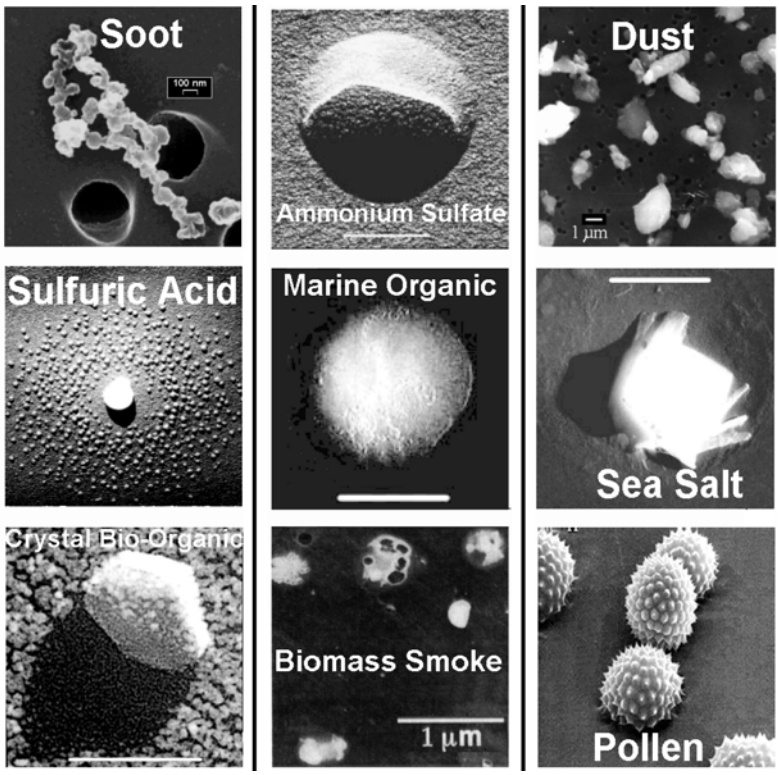

Figure 1.1: Electron-microscopic pictures of aerosol particles of various origin. First row displays aerosols in the Aitken mode size-range ($0.005 < r < 0.05$ μm), second row in accumulation mode size-range ($0.05 < r < 0.5$ μm), third row coarse mode size range (0.5 μm $< r$). From Brasseur et al. (2003).

1.2 Microphysical Evolution of Aerosols

Observations of atmospheric aerosol particles reveal that their size-distribution generally can be represented by a superposition of log-normal modes. Following Whitby (1978), these modes are typically distinguished as the nucleation mode (particles with radii $r < 0.005$ μm), the

Aitken mode ($0.005 < r < 0.05$ μm), the accumulation mode ($0.05 < r < 0.5$ μm), and the coarse mode (0.5 μm $< r$). A multitude of aerosol components can reside within each of these size ranges, as separate particles or as particles with mixed composition. The two extremes of this aerosol mixing state are referred to as external and internal mixtures. The external mixture describes a mixture of particles each of which is made of solely one compound while the internal mixture refers to the assumption that all particles contain a uniform mixture of the individual components. The size-distribution, composition and mixing state of aerosols are determined by their state at the moment of emission or formation and a combination of subsequent microphysical and chemical transformation processes.
The main formation and transformation processes related to atmospheric aerosol are illustrated in Figure 1.2.

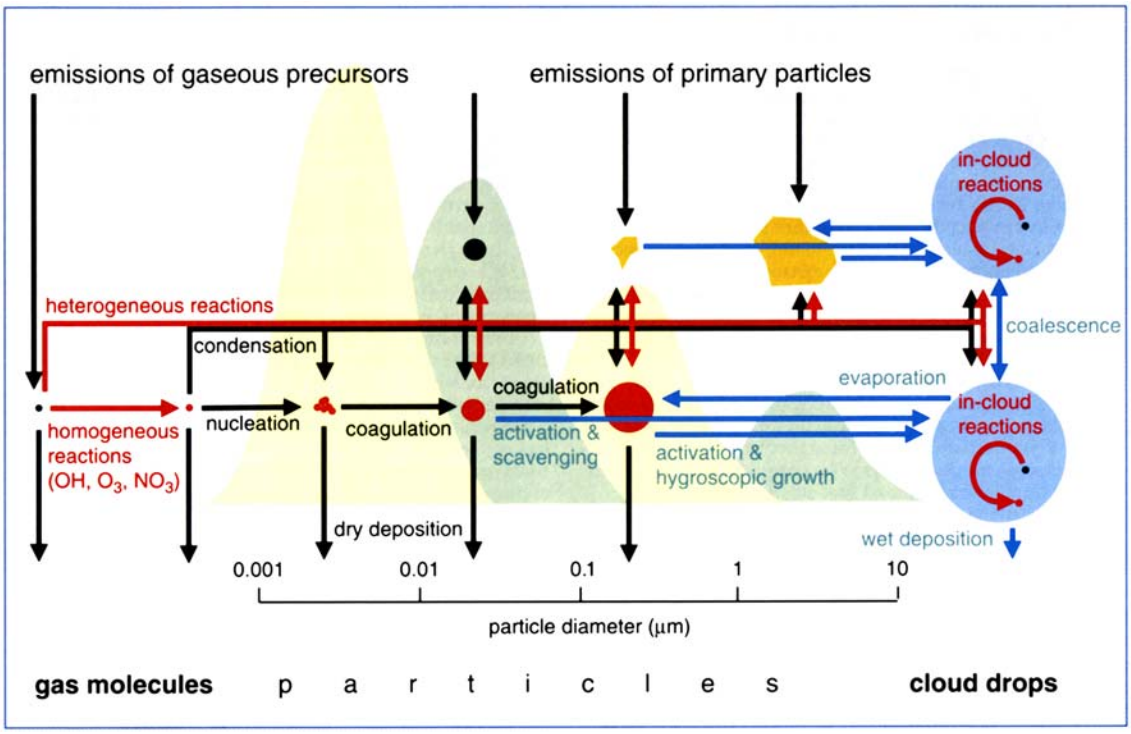

Figure 1.2: Illustration of the microphysical and chemical processes affecting the size-distribution and composition of atmospheric aerosols. From Brasseur et al. (2003).

Natural primary emissions, such as mineral dust, sea salt, and pollen, have typically sizes in the accumulation and coarse mode range. Primary emissions of carbonaceous aerosols from anthropogenic combustion processes have typically sizes in the Aitken and accumulation mode range.

Secondary particles are nucleated via formation of thermodynamically stable molecular clusters and subsequent growth (Kulmala, 2003). A number of nucleation pathways including the binary nucleation of the sulfuric acid - water system (Wilemski, 1984), ternary nucleation additionally considering ammonia (Korhonen et al., 1999), ion-induced nucleation (Arnold, 1982), including organic (O'Dowd et al., 2002a) and iodide precursors (O'Dowd et al., 2002b) are known. However, their relative importance under atmospheric conditions is still not fully elucidated.
Aerosol particles grow by coagulation with other aerosols (Fuchs, 1964) and condensation of

available vapours (Fuchs, 1959) such as sulfuric acid or organic vapours. When particles grow larger than the mean free path length of the condensing molecule, condensation becomes diffusion limited. Additionally, coagulation reduces the number of available particles for coagulation so that the coagulational growth is slowed down. Therefore, it takes days to weeks before nucleated particles under background conditions reach the accumulation mode size-range. Under polluted conditions the growth to the accumulation mode size range can occur within a day (Raes et al., 2000). With increasing aerosol size, the coagulational growth becomes inefficient as the collision with particles of the same size becomes unlikely and the coagulation with small particles does only slowly increase the particle radius. (To double the particle radius it requires to eightfold the particle mass, a process that requires to collect a large number of small particles.) Hence, under atmospheric conditions and sink-strength, nucleated particles and particles emitted in the Aitken and accumulation mode size range do not grow into the coarse mode size range and therefore accumulate in the size range $0.05 < r < 0.5$ μm, termed accumulation mode. Atmospheric coarse-mode particles are generally of primary origin.

Water uptake by aerosols is an important process as it affects their ambient size-distribution, composition, chemical and radiative properties. Particles containing inorganic salts grow with increasing ambient relative humidity, when the humidity reaches the deliquescence relative humidity (DRH), spontaneously by water uptake from the surrounding air. With decreasing ambient humidity, the particles release the up-taken water not until a relative humidity well below the DRH, the so called efflorescence relative humidity (ERH). Other aerosol species, such as sulfuric acid, do not show deliquescence behaviour, but can be highly hygroscopic and uptake water masses of severalfold of their own mass (e.g. Pruppbacher and Klett (1997)).

When aerosols at a given supersaturation reach the critical radius of activation, they become activated and grow spontaneously, limited only by the availability of water vapour. The critical radius of activation can be derived from the Köhler theory (Köhler, 1921) and depends crucially on the aerosol composition. By this mechanism, small aerosol particles of 0.05 μm radius can grow to small cloud droplets of 5 μm and larger, multiplying their mass by more than a billion. Aerosols with a radius larger than the critical radius of activation at a given supersaturation are referred to as cloud condensation nuclei (CCN). Additionally, aerosols can be embedded into cloud droplets by coagulational processes and by their formation in the aqueous-phase of cloud droplets.

In-cloud processing of aerosols modifies the aerosol size-distribution, composition, and mixing state (Flossmann et al., 1985; Bower and Choularton, 1993; Hoppel et al., 1994; Wurzler et al., 2000). It can be assumed that each cloud droplet is formed from one CCN and additionally aerosols are embedded into cloud water by other processes such as coagulation (c.f. Section 1.3). As collision-coalescence processes dominate the growth of cloud droplets to larger sizes, these processes will also mix the respective CCN or their solutes. Upon evaporation or sublimation of cloud or precipitation water, the aerosols in the droplets will be released in the cloud-free atmosphere and the resulting aerosol distribution will be shifted towards larger sizes and internal mixture. Pruppacher and Jaenicke (1995) estimate that on average each aerosol particle observed far from the source has been cycled three times through cloud processing.

Also condensational and coagulational growth processes will shift the mixing state towards internal mixtures in the presence of several aerosol components. Contrariwise, primary emissions and secondary particle formation maintain an externally mixed state of the system. Therefore, it is appropriate to describe the aerosol distribution by a superposition of several modes with varying mixing states.

1.3 Sinks of Atmospheric Aerosols

The removal processes of aerosols and their precursors determine for given source strengths the atmospheric aerosol life-time and burden and therefore their radiative effects. Dry and wet deposition processes determine the total removal.
Dry deposition to the surface is typically approached in form of a serial resistance analogue (Hicks et al., 1987) in which the resistances represent the turbulent transport through the surface layer (aerodynamic resistance), the diffusion through the thin quasi-laminar layer above the surface (quasi-laminar boundary layer resistance), and a combination of the various surface uptake processes (surface resistance). For aerosols additionally the gravitational settling throughout the atmospheric column needs to be taken into account which acts as parallel resistance to the dry deposition. The surface resistance for aerosols is generally assumed zero, corresponding to the neglect of resuspension.
Wet deposition of atmospheric gases and aerosols involves the transfer of the respective component to the aqueous phase and the subsequent deposition of the hydro-meteors at the surface. Hydro-meteors in this context refers to cloud-droplets, rain-drops, and ice crystals. The dominant transfer process of aerosol mass to the aqueous phase is the activation of cloud condensation nuclei. In particular for the small particles, the collection by falling droplets, Brownian diffusion, thermophoresis, photophoresis, and diffusiophoresis contribute to the transfer to the hydro-meteors. For the in-cloud scavenging, once the particles are embedded or dissolved in cloud droplets their fate depends on the cloud microphysical processes and the resulting precipitation efficiency. A fraction of the aerosol is embedded in the formed precipitation and falls towards the surface, a fraction of the precipitation re-evaporates and releases the aerosol content in lower altitudes, and a fraction is deposited at the surface. The falling precipitation will also collect aerosol particles, referred to as below-cloud scavenging.
The atmospheric aerosol load is in a dynamic equilibrium between source and sink processes that determines their life-time. The sink processes are so efficient that aerosols do not accumulate in the atmosphere, resulting in aerosol life-times ranging from minutes for coarse particles to several days for lower-tropospheric fine particle. Upper tropospheric aerosol particles have life-times of several weeks and stratospheric aerosol a life-time of approximately one to three years (Seinfeld and Pandis, 1998). The short life-time of aerosols is the cause of the large spatio-temporal variability of their distribution and effects, with maxima in proximity of the sources.

1.4 The Role of Aerosols in the Earth System

Aerosols play an important role in the global climate system. Aerosol particles directly modify the global radiation budget, by scattering and absorption of solar and thermal radiation (Ångström, 1962; McCormic and Ludwig, 1967), referred to as direct aerosol effect. The overall effect of an aerosol plume, cooling or warming, depends on the composition, the size-distribution, and the mixing state, as well as on the albedo of the underlying surface or clouds. With increasing absorption of the components, the increase in planetary albedo by enhanced backscattering of solar radiation, the cooling effect, is outweighted by the absorption and associated warming. Some aerosol components, such as ammonium sulfates, sea salt and aerosol water are almost exclusively scattering and therefore associated with cooling (Hess et al., 1998; Shettle and Fenn, 1979; Downing and Williams, 1975). Black carbon, in contrast is a strong absorber in the visible wavelengths and therefore associated with warming (Hess et al., 1998). Organic carbonaceous compounds are predominantly scattering and only weakly absorbing (Koepke et al., 1997). Other

components, such as mineral dust, are predominantly scattering in the visible wavelengths and absorbing in the ultraviolet and infrared wavelengths, depending on the regional composition (Sokolik and Toon, 1996). However, the calculation of the radiative properties is complicated by the dependence on the size-distribution, mixing state, and the arrangement of the individual components in mixed particles (Jacobson, 2000; Lesins et al., 2002).

Aerosols additionally modify the global radiation budget indirectly, by modification of cloud properties. An increase of aerosols acting as cloud condensation nuclei yields higher cloud droplet number concentrations (CDNC) with smaller radii, increasing the cloud albedo (Twomey, 1974, 1977), referred to as first indirect effect. Additionally, higher CDNC potentially decrease the precipitation efficiency of clouds resulting in a longer lifetime and a subsequent increase of the planetary albedo (Albrecht, 1989), referred to as second indirect effect. Absorbing aerosols heat the atmosphere potentially evaporating cloud droplets (Graßl, 1975; Hansen et al., 1997), referred to as semi-direct effect. Suitable aerosols act as ice-nuclei with the potential to enhance the precipitation formation in mixed phase clouds (Lohmann, 2002), decreasing the cloud lifetime and therefore the global albedo, referred to as glaciation indirect effect. Aerosols could reduce the droplet size of convective clouds and suppress the precipitation formation (Rosenfeld, 1999; Khain et al., 2001) with potential implications for the radiation balance and the global circulation (Nober et al., 2003).

Aerosol scattering and absorption reduces the incoming short-wave radiation at the surface (Gilgen et al., 1998) which is only partly offset by enhanced downwelling long-wave radiation. This reduction is partly balanced by reductions in outgoing surface long-wave radiation and partly by reductions in the fluxes of latent and sensible heat, hence accompanied by reductions of evaporation and evapotranspiration, dampening the hydrological cycle (Liepert et al., 2004; Feichter et al., 2004).

The concept of "radiative forcing" has been employed in the Intergovernmental Panel on Climate Change (IPCC) assessment reports as a measure of externally imposed perturbations in the Earth's radiative energy budget. "The radiative forcing of the surface-troposphere system due to the perturbation in or the introduction of an agent is the change in net irradiance at the tropopause after allowing for stratospheric temperatures to re-adjust to radiative equilibrium, but with surface and tropospheric temperatures and state held fixed at the unperturbed values." (Ramaswamy et al. (2001) in IPCC (2001)). This definition is restricted to external perturbations without any surface or tropospheric feedbacks in operation. Therefore, it cannot account for e.g. the cloud-lifetime effect and the semi-direct aerosol effects that involve internal changes in the cloud water content. The global annual mean surface temperature response to a given forcing ΔF defines the climate sensitivity parameter λ (Dickinson, 1982; WMO, 1986; Ramaswamy et al., 2001)

$$\lambda = \frac{\Delta T_S}{\Delta F} \tag{1.1}$$

as a first order measure for the relative climatic impact of different radiative perturbations. While the sensitivity parameters are model specific, for each model it is considered approximately constant for a wide range of forcings (Ramaswamy et al., 2001). In Ramaswamy et al. (2001) aerosol radiative forcings were estimated from modelling studies performed separately for a number of aerosol species. The resulting estimates are depicted in Figure 1.3. For sulfate the best estimate of the direct radiative forcing was -0.4 $\mathrm{W\,m^{-2}}$, for aerosols from biomass burning -0.2 $\mathrm{W\,m^{-2}}$, for fossil-fuel BC +0.2 $\mathrm{W\,m^{-2}}$, for fossil-fuel organic carbonaceous aerosols -0.1 $\mathrm{W\,m^{-2}}$, for mineral dust the uncertainty range was given as -0.6 to +0.4 $\mathrm{W\,m^{-2}}$. It is

important to point out that for all aerosol components the uncertainty associated with the aerosol radiative forcing exceeds the forcing itself. Due to the high uncertainties, for mineral dust and the first-indirect effect no best estimate of the forcing is given.

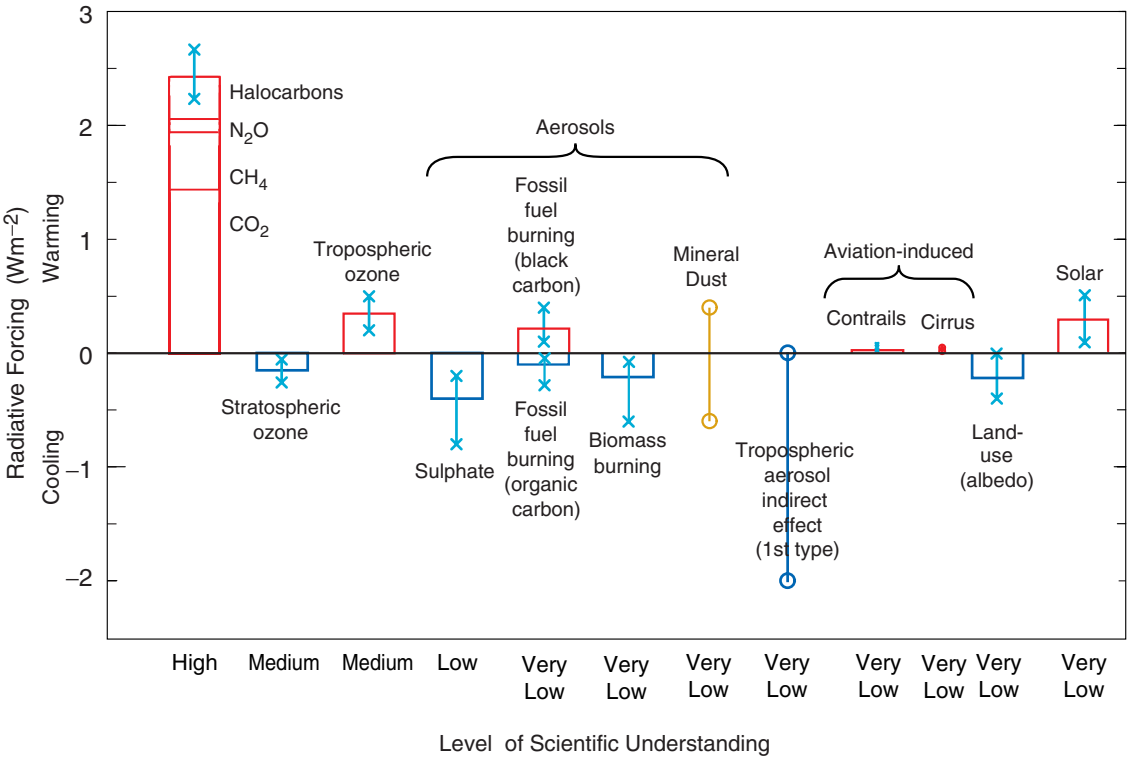

Figure 1.3: Global annual mean radiative forcings [$\mathrm{W\,m^{-2}}$] for the year 2000 with respect to the year 1750 due to a number of agents. The rectangular bars denote the best estimate values, the lines indicate the uncertainty range. From Ramaswamy et al. (2001) in IPCC (2001).

However, the underlying concept of additivity, i. e. that individual forcings can be linearly added to obtain the total forcing and total surface temperature response is not self-evident. In fact, this assumption in Ramaswamy et al. (2001) is based on a small number of simulations limited to greenhouse gases and sulfate aerosols. In a recent study, Feichter et al. (2004) show in a global simulation with more relevant aerosol components interactively coupled to the hydrological cycle, that the global warming for combined greenhouse gas and aerosol forcing is significantly smaller than the sum of the individual temperature changes. Additionally, it should be kept in mind that the aerosol radiative properties are highly non-linear functions of size-distribution, composition, mixing-state, and the arrangement of the individual components in mixed particles. As observations suggest that the global aerosol system has a large internally-mixed contribution (Murphy et al., 1998; Bates et al., 1998; Seinfeld et al., 2004), a linear variation of the aerosol radiative properties to perturbations in the aerosol system, such as emission changes, appears unlikely. The linearity of the response of the aerosol system to anthropogenic disturbances is investigated in Section 3.4.

Even if additivity is presumed, due to the large uncertainties associated with the individual forcings, a linear addition of the forcings to derive the total aerosol radiative forcing might not be appropriate (Boucher and Haywood, 2001). However, from Figure 1.3 it is discernible that the total aerosol radiative forcing is most likely negative. Based on the individual forcings

given in Ramaswamy et al. (2001), Boucher and Haywood (2001) derive a 75-97 % probability of the total radiative forcing to be positive with a mean radiative forcing ranging from +0.68 to +1.34 $\mathrm{W\,m^{-2}}$. This constitutes a significant reduction of the underlying best guess greenhouse gas forcing of +2.43 $\mathrm{W\,m^{-2}}$. The presumably negative present day total aerosol forcing potentially masks a part of the warming due to the positive greenhouse gas forcing.

In addition to the direct radiative effects of aerosols and their climate effects via the hydrological cycle, they interact via heterogeneous and multi-phase reactions with the chemistry of the atmosphere, affecting the atmospheric composition and the radiative effects of chemical species, such as ozone (Crutzen, 1996; Ravishankara, 1997; Andreae and Crutzen, 1997).

The depositions of aerosols has distinct impacts on the global ecosystems. Deposition of mineral dust in the ocean plays an important role in the biogeochemical cycle of the oceans. It provides trace elements such as iron that is considered an important micro-nutrient for the marine biogeochemistry (Martin and Fitzwater, 1988; Johnson et al., 1997). The marine biogeochemistry in turn is affecting the climate system via the emissions of aerosol precursors such as DMS and organic particulate matter with potential feedbacks via aerosol cloud interactions (Charlson et al., 1987). Also for terrestrial ecosystems the input of trace elements by dust deposition is of essential importance. For example, it has been proposed that the vegetation of the Amazon basin is highly dependent on Saharan dust deposition as it provides phosphorus, necessary for the maintainance of long-term productivity (Swap et al., 1992; Okin et al., 2004). However, aerosol deposition is not only beneficial for the global ecosystems. Oxidation processes in the atmosphere produce a variety of acids such as HNO_3 and HCl residing in the gas phase and such as sulfate and nitrate residing in the aerosol phase. Dry and wet deposition of these acids is referred to as acid deposition or generally simplified as "acid rain". Acid deposition by anthropogenic pollution can cause serious environmental problems such as acidification of surface waters with disturbances of aquatic ecosystems and disturbances to vegetation and forests (e.g. Likens and Bohrmann (1974)). While in Europe and North America mitigation strategies for acidification-related aerosol precursors constrained the problem (Stoddard et al., 1999), acidification leads to increasingly serious environmental issues in Asia (Li and Gao, 2002).

Beside the environmental effects associated with atmospheric aerosols, it is now generally accepted that enhanced aerosol concentrations in polluted areas pose a risk to human health (Dockery et al., 1993; Lippmann, 2000). In addition, toxic pollutants, such as DDT, condense on aerosol particles so that their transport and deposition are largely determined by the aerosol pathways (van Pul et al., 1998; Unsworth et al., 1999).

Despite the demonstrated importance of atmospheric aerosols for the earth system, the quantitative understanding and evaluation of their effects is still insufficient (e.g. Penner et al. (2001); Ramaswamy et al. (2001); Ramanathan et al. (2001); Heintzenberg et al. (2003)). In IPCC (2001) the level of scientific understanding is considered "very low" for all aerosol radiative effects except for sulfate for which it is considered "low". One reason for that deficiency is the inherent complexity of the global aerosol system outlined in the preceding paragraphs. The other main reason for the insufficient understanding of the global aerosol system is that the short life-time of aerosols causes large spatio-temporal inhomogeneities. Thus, in-situ observations that provide the most detailed insight into the aerosol system, are representative of limited spatial and temporal scales. Remote sensing data from ground-based lidar and sun-photometers provides valuable information but suffers from similar sampling issues. Up to now, operational remote sensing data from space only provides integral aerosol properties and the retrievals rely on a-priori information about the aerosol system and internal aerosol models.

A limitation of aerosol remote sensing data is that the anthropogenic signal is per se not distinguishable from the natural signal. Therefore, assumptions about the size and composition of anthropogenic aerosols are typically imposed to derive the anthropogenic contribution (e.g. Christopher and Zhang (2004)). Nonetheless, considerable insight into the anthropogenic aerosol effects can be gained from the analysis of long-term satellite data over regions with known changes of anthropogenic emissions. Krüger and Graßl (2002) demonstrated the indirect aerosol effect with a decrease of the planetary albedo over Europe, analysing trends attributable to the emission reductions from the late eighties to the late nineties. In Krüger and Graßl (2004) they showed for the same period that the increasing absorption over China, attributable to emission increases, lead to a decrease of the planetary albedo over China.

1.5 Global Aerosol Modelling

Global aerosol models can help to increase the understanding about the complex global aerosol system for past, present, and future conditions. Furthermore, they permit to identify the effects of specific aerosol components and aerosol sources, natural or anthropogenic, on the global climate system.

The first global aerosol models simulated the distribution of the mass of one of the major aerosol components: sulfate, black carbon, particulate organic matter, sea salt, and mineral dust. Langner and Rhode (1991), Feichter et al. (1996), and Rasch et al. (2000) simulated the global sulfur cycle. A range of studies (e.g. Cooke et al. (1996); Liousse et al. (1996); Cooke et al. (1999)) simulated the distribution of carbonaceous aerosols. The mineral dust cycle has been investigated e.g. in Tegen and Lacis (1997); Ginoux et al. (2001) and the sea salt distribution e.g. in Guelle et al. (2001). Succeedingly, global aerosol models incorporated more aerosol components as external mixtures (Haywood et al., 1997b; Lohmann et al., 1999a; Chin et al., 2002). All of these models are bulk mass models with highly parameterised treatment of the aerosol processes. For the parameterisation of each of the sink processes, for the aerosol radiative properties, and for the parameterisation of the indirect aerosol effects, assumptions about the aerosol mixing-state and size-distribution have to be made. As these parameterisations are typically derived independently, inconsistencies in the implicit assumptions of aerosol properties are common.

The size-distribution of single aerosol components has been investigated, for mineral dust by Tegen and Lacis (1997) and for sea salt by Gong et al. (2002), predicting the evolution of aerosol size-classes with size-dependent sources and sinks.

The complexity of the processes and computational constraints caused a furcation in the model development. On the one hand models with advanced chemistry and thermodynamics evolved (Nenes et al., 1998; Adams et al., 1999) with a focus on the chemical composition. On the other hand microphysical models developed with a focus on the prediction of the size distribution and with less detail on the aerosol composition. Probably the most detailed aerosol description in a global model has been presented by Jacobson (2001b) including microphysical and thermodynamical detail. However, it is computationally too demanding for transient simulations.

Sectional aerosol models discretise the aerosol size-distribution into discrete bins and predict the evolution of the aerosol particles for each bin. With a fine discretisation, sectional aerosol models provide a detailed description of the aerosol size-distribution. Adams and Seinfeld (2002) simulate the size-distribution of sulfate aerosol with a 30-bin sectional microphysical aerosol model. However, also the aerosol mixing-state affects their microphysical, chemical and radia-

tive properties and therefore their cycling and climatic effects. The computational burden of multicomponent sectional aerosol models with size-resolved description of the mixing state is with current computational resources too demanding for the long-term transient climate simulations of the global aerosol system.
Up to now, no aerosol modules for global circulation models existed, that are suitable for long-term integrations and simulate the size-distribution and mixing state of fully interacting multicomponent aerosols. The application of computationally efficient aerosol microphysical schemes that maintain the balance in complexity between the numerous processes in general circulation models is a requirement for long-term transient aerosol-climate simulations.
Modal aerosol models in which the size-distribution is represented by analytical functions provide the required computational efficiency. Instead of the simulation of the evolution of a large number of discrete bins, it is sufficient to simulate the evolution of the moments describing the respective analytical function. As observed aerosol size-distributions can typically be represented by a superposition of log-normal distributions, the log-normal distribution is generally chosen for the representation of the aerosol size-distribution in modal aerosol models (Whitby et al., 1991). On the global scale, Wilson et al. (2001) represent the size-distribution in a multicomponent aerosol model by a superposition of eight partly interacting log-normal modes. Ghan et al. (2001a,b) use a global aerosol module with four internally mixed log-normal modes, neglecting externally mixed contributions, to estimate the direct and indirect radiative aerosol forcing.

Although global aerosol models provide the unique possibility to isolate the anthropogenic contribution to the effects of aerosols in the earth system, the associated uncertainties are high. Ten out of eleven global aerosol models that have participated in the 2001 IPCC intercomparison workshop (Penner et al., 2001) are based on a bulk mass approach that has several crucial limitations:

- Almost all processes relevant for the global aerosol system, such as their sinks and radiative properties, their water uptake and chemical reactivity, depend on the aerosol size-distribution, composition, and mixing state. However, the size-distribution and mixing state are no prognostic parameters in bulk models and therefore have to be prescribed.
- There is no justification that these assumptions are applicable under different climatic and environmental conditions. In fact, the observed large internally-mixed aerosol population is a clear indicator that the mixing state and the size-distribution are not constant for different levels of emissions.
- A violation of these assumptions affects the estimates of the aerosol radiative effects. In particular the indirect effects, in bulk models parameterised as function of the prognosed aerosol mass, are highly sensitive to changes in the size-distribution.
- As the mixing state is no prognostic parameter, the estimates of global radiative effects are based on the assumption of additivity of the radiative effects of externally mixed aerosol populations.
- The neglect of microphysical growth processes does not allow to investigate the role of nucleation as secondary particle source.
- Aerosol water uptake in most bulk models is only diagnosed for the calculation of the aerosol radiative properties. However, aerosol water contributes significantly to the aerosol mass, affecting the sink processes and global distribution.

1.6 Objectives of This Study

The primary objective of this study is to advance the understanding about the global tropospheric aerosol system as basis for higher accuracy estimates of the anthropogenic aerosol effects.

This objective is approached threefold:

First, to overcome the deficiencies and constraints of traditional global aerosol models used for the assessment of the aerosol radiative effects, the global aerosol-climate model ECHAM5-HAM (Stier et al., 2004) has been developed, based on following objectives:

- Mechanistic treatment of the relevant aerosol microphysical processes based on a prognostic approach for aerosol composition, size-distribution, and mixing state
- Reduction of the number of externally imposed parameters allowing the application in a wide range of climate regimes
- Interactive calculation of relevant natural aerosol and aerosol precursor sources
- Realistic aerosol representation as basis of a mechanistic coupling with the other components of a fully coupled earth system model
- Computational efficiency for long term climate simulations

Second, limitations of the underlying assumptions of the traditional approach for the assessment of the aerosol radiative effects are addressed. Building on the established degrees of freedom of the ECHAM5-HAM aerosol-climate model, the internal dynamics of the aerosol system as a response to anthropogenic disturbances is analysed to address one of the key questions:

- Is the response of the aerosol system to anthropogenic disturbances as linear and additive as traditionally assumed?

Third, methods and first applications of ECHAM5-HAM towards the assessment of the aerosol radiative effects are introduced.

1.7 Outline

This study is organised around three main sections, Chapters 2-4, of which Chapter 2 and Chapter 3 are journal publications. This structure implicates minor recurrences. Each Chapter is followed by an intermediate summary and conclusions. The overall outline of this study is as follows.

In Chapter 2 the development and evaluation of the ECHAM5-HAM aerosol-climate model is presented. This chapter has been published in *Atmospheric Chemistry and Physics Discussions* (Stier et al., 2004). As part of ECHAM5-HAM, the microphysical core M7 is described that has been adapted from the original box-model version, tested, and enhanced in co-operation with the box-model authors Elisabetta Vignati[1] and Julian Wilson[1] and has been published in Vignati et al. (2004).

[1]Institute for Environment and Sustainability, European Commission, Ispra, Italy

The internal dynamics of the aerosol system as a response to anthropogenic disturbances, introduced in form of emission changes, is analysed in Chapter 3. A series of simulations with the ECHAM5-HAM model is performed with specific changes of the anthropogenic emissions. The focus of the analysis is on the non-linear responses of the aerosol mass and number distributions and of the optical thickness, the coherence of the different aerosol cycles and the deviation of the results from additivity. This chapter has been submitted for publication in *Journal of Climate*.

First applications of ECHAM5-HAM to derive the aerosol radiative effects are presented in Chapter 4. For the analysis of the radiative effects, an alternative concept to radiative forcing is introduced, allowing for local-scale internal responses to external perturbations while constraining the large scale dynamics. An extension of the ECHAM5 stratiform cloud scheme and two methods for the aerosol-cloud coupling for the assessment of the indirect aerosol effects are introduced. First results from the aerosol-cloud coupling are presented and evaluated.

Chapter 5 concludes the main findings and gives an outlook to ongoing and future research activities.

Chapter 2

The Aerosol-Climate Model ECHAM5-HAM[1]

Abstract

The aerosol-climate modelling system ECHAM5-HAM is introduced. It is based on a flexible microphysical approach and, as the number of externally imposed parameters is minimised, allows the application in a wide range of climate regimes. ECHAM5-HAM predicts the evolution of an ensemble of microphysically interacting internally- and externally-mixed aerosol populations as well as their size-distribution and composition. The size-distribution is represented by a superposition of log-normal modes. In the current setup, the major global aerosol compounds sulfate (SU), black carbon (BC), particulate organic matter (POM), sea salt (SS), and mineral dust (DU) are included. The simulated global annual mean aerosol burdens (lifetimes) for the year 2000 are for SU: 0.80 Tg(S) (3.9 days), for BC: 0.11 Tg (5.4 days), for POM: 0.99 Tg (5.4 days), for SS: 10.5 Tg (0.8 days), and for DU: 8.28 Tg (4.6 days). An extensive evaluation with in-situ and remote sensing measurements underscores that the model results are generally in good agreement with observations of the global aerosol system. The simulated global annual mean aerosol optical depth (AOD) is with 0.14 in excellent agreement with an estimate derived from AERONET measurements (0.14) and a composite derived from MODIS-MISR satellite retrievals (0.16). Regionally, the deviations are not negligible. However, the main patterns of AOD attributable to anthropogenic activity are reproduced.

2.1 Introduction

Atmospheric aerosols play an important role in the global climate system. Aerosol particles influence the global radiation budget directly, by scattering and absorption (Ångström, 1962; McCormic and Ludwig, 1967), as well as indirectly, by the modification of cloud properties (Twomey, 1974; Graßl, 1975; Twomey, 1977; Albrecht, 1989; Hansen et al., 1997; Lohmann, 2002), with feedbacks to the hydrological cycle (Lohmann and Feichter, 1997; Liepert et al., 2004). Furthermore, heterogeneous reactions on the aerosol surface and in liquid aerosol particles interact with the chemistry of the atmosphere (Ravishankara, 1997; Andreae and Crutzen, 1997; Crutzen, 1996; Dentener and Crutzen, 1993). Pollutants, such as DDT, condense on aerosol

[1]Published as: Stier, P., J., Feichter, S. Kinne, S. Kloster, E. Vignati, J. Wilson, L. Ganzeveld, I. Tegen, M. Werner, M. Schulz, Y. Balkanski, O. Boucher, A. Minikin, A. Petzold, *Atmospheric Chemistry and Physics*, **5**, 1125-1156, 2005.

particles so that their transport and deposition are largely determined by the aerosol pathways (van Pul et al., 1998; Unsworth et al., 1999). Moreover, the deposition of aerosol in the ocean plays an important role in the biogeochemical cycle of the oceans (Vink and Measures, 2001; Johnson et al., 1997).

Nevertheless, the quantitative comprehension of the role of aerosols is still insufficient (e.g. Penner et al., 2001; Ramanathan et al., 2001; Heintzenberg et al., 2003).

To increase the understanding of this complex system, the ECHAM5 General Circulation Model (GCM) (Roeckner et al., 2003) has been extended by a complex aerosol model allowing long-term, i.e. depending on the model resolution centennial to millennial scale, transient climate simulations. A major objective is to quantify the aerosol radiative effects and their impacts on the global climate system for present day and future conditions.

Most previous studies of the global aerosol system (e.g. Langner and Rhode, 1991; Feichter et al., 1996; Roelofs et al., 1998; Lohmann et al., 1999a; Rasch et al., 2000; Chin et al., 2002) have simulated the global distribution of the mass of one or more of the major aerosol components: sulfate (SU), elemental carbon, henceforth denoted as black carbon (BC), particulate organic matter (POM), sea salt (SS), and mineral dust (DU). In these studies aerosol is either represented by an external mixture (e.g. Lohmann et al., 1999a; Tegen et al., 1997) or by an internal mixture with a fixed ratio of the individual components (e.g. Haywood et al., 1997b). An internal mixture refers to the assumption that all particles contain a uniform mixture of the individual components whilst an external mixture describes a mixture of particles each of which is made of solely one compound. However, observations show (e.g. Murphy et al., 1998; Bates et al., 1998; Seinfeld et al., 2004) that the mixing state of the global aerosol system is highly variable with a large internally mixed contribution and varying ratios among constituents. This important property of the global aerosol system can not be accounted for with the conventional bulk modelling approach, solely based on aerosol mass. Another drawback of the bulk modelling approach is that in order to calculate direct and indirect radiative effects, as well as the sinks of the aerosol mass itself, implicit assumptions about the aerosol size distribution have to be imposed. Many feedback cycles are highly sensitive to aerosol number and therefore to the size-distribution. In short, a comprehensive analysis of aerosol-climate interactions, including feedback processes, requires knowledge of the size-distribution, the composition, and the mixing state and therefore size-segregated, microphysical, multicomponent aerosol modules suitable for long-term integrations.

Tegen and Lacis (1997) simulated the size-distribution and radiative properties of mineral dust in a GCM with size-dependent sources and sinks without interaction among the size classes. Adams and Seinfeld (2002) predicted the size-distribution of sulfate aerosol with an interactive approach. A number of studies, (e.g. Tegen et al., 1997; Jacobson, 2001a; Takemura et al., 2000), incorporated partly size-segregated aerosol modules with several components into global aerosol models, neglecting the microphysical interaction among the components. Only recently, size-segregated, interactive multicomponent aerosol modules are embedded into global models allowing to simulate the mixing state explicitly. Wilson et al. (2001) represent the size-distribution in a multicomponent aerosol model by a superposition of eight partly interacting log-normal modes. Ghan et al. (2001a,b) use an interactive modal size-segregated multicomponent module to estimate the direct and indirect radiative aerosol forcing. Gong et al. (2003) describe the development of a size-segregated aerosol module and apply it to the simulation of the global sea-salt distribution (Gong et al., 2002). They have the option to treat fresh emissions as external mixture with a fixed aging time, assuming that the aging only occurs in the emission grid box.

In the development of the ECHAM5-HAM aerosol model the attempt was made to minimise the number of externally imposed parameters. Aerosol size-distribution and composition are prognostic parameters. The modal setup allows to predict the evolution of an ensemble of interacting internally- and externally-mixed aerosol populations. The sink processes as well as the aerosol optical properties are calculated in dependence of size and composition. This setup allows the prediction of the aerosol radiative effects directly from the prognostic variables and provides the necessary parameters for the aerosol-cloud coupling. Computational efficiency of this aerosol model permits the application in long-term climate studies.
Section 2.2 describes the setup of the ECHAM5-HAM model. Results from a simulation for the year 2000 and their evaluation are presented in Section 2.3. Section 2.4 concludes the discussion and presents an outlook to future developments.

2.2 Model Description

2.2.1 The ECHAM5 General Circulation Model

The atmospheric general circulation model ECHAM5 is the fifth-generation climate model developed at the Max Planck Institute for Meteorology, evolving from the model of the European Centre for Medium-Range Weather Forecasts (ECMWF). ECHAM5 solves prognostic equations for vorticity, divergence, surface pressure and temperature expressed in terms of spherical harmonics with a triangular truncation. Water vapour, cloud liquid water, cloud ice and trace components are transported with a flux form semi-Lagrangian transport scheme (Lin and Rood, 1996) on a Gaussian grid. ECHAM5 contains a new microphysical cloud scheme (Lohmann and Roeckner, 1996) with prognostic equations for cloud liquid water and ice. Cloud cover is predicted with a prognostic-statistical scheme solving equations for the distribution moments of total water (Tompkins, 2002). Convective clouds and convective transport are based on the mass-flux scheme of Tiedtke (1989) with modifications by Nordeng (1994). The solar radiation scheme (Fouquart and Bonnel, 1980) has 4 spectral bands, 1 for the visible and ultra-violet, and 3 for the near-infrared. The long-wave radiation scheme (Mlawer et al., 1997; Morcrette et al., 1998) has 16 spectral bands. ECHAM5 has the capability to perform nudged simulations, i.e. to relax the prognostic variables towards an atmospheric reference state, such as forecast or re-analysis data from operational weather forecast models.

2.2.2 The Modal Concept

A fine discretisation of the wide aerosol spectrum is with current computational resources not efficient for the long term global prediction of interactive multicomponent aerosol distributions and their mixing state. Thus, the aerosol spectrum in HAM is represented by the superposition of seven log-normal distributions:

$$n(\ln r) = \sum_{i=1}^{7} \frac{N_i}{\sqrt{2\pi}\ln\sigma_i} \exp\left(-\frac{(\ln r - \ln \bar{r_i})^2}{2\ln^2\sigma_i}\right) \tag{2.1}$$

Each mode i of the aerosol number distribution can be described by the three moments aerosol number N_i, the number median radius $\bar{r_i}$, and the standard deviation σ_i. In HAM it is assumed that the standard deviation is constant and set to $\sigma = 1.59$ for the nucleation, Aitken, and accumulation modes and to $\sigma = 2.00$ for the coarse modes (Wilson et al., 2001). Thus, it is possible to calculate the median radius of each mode from the corresponding aerosol number and

aerosol mass, which are transported as tracers. The modes of the aerosol model are composed either of compounds with no or low water-solubility, henceforth denoted as insoluble mode, or by an internal mixture of insoluble and soluble compounds, henceforth denoted as soluble mode. The composition of each internally mixed mode can be modified by aerosol dynamics, e.g. coagulation, by thermodynamical processes, e.g. condensation of sulfate on pre-existing particles, and by cloud processing. In this study we describe an implementation of the aerosol model with following components: sulfate, black carbon, organic matter, sea salt, and mineral dust. However, ECHAM5-HAM is flexible to be extended to more compounds. Table 2.1 illustrates the modal setup and the underlying mixing concept. The seven modes are grouped into four geometrical size classes, ranging from the nucleation, Aitken, and accumulation modes to the coarse mode size range. Each mode has a varying median radius and fixed mode boundaries used for the repartitioning between the modes as described in Section 2.2.7. Three of the modes are constituted solely of insoluble compounds, four of the modes contain at least one soluble compound. The modal setup is designed to allow an externally mixed contribution of initially insolubly emitted species.

Modes $\bar{r}$ [μm]	**Soluble / Mixed**	**Insoluble**
Nucleation $\bar{r} \leq 0.005$	N_1, M_1^{SU}	
Aitken $0.005 < \bar{r} \leq 0.05$	N_2, M_2^{SU}, M_2^{BC}, M_2^{POM}	N_5, M_5^{BC}, M_5^{POM}
Accumulation $0.05 < \bar{r} \leq 0.5$	N_3, M_3^{SU}, M_3^{BC}, M_3^{POM}, M_3^{SS}, M_3^{DU}	N_6, M_6^{DU}
Coarse $0.5 < \bar{r}$	N_4, M_4^{SU}, M_4^{BC}, M_4^{POM}, M_4^{SS}, M_4^{DU}	N_7, M_7^{DU}

Table 2.1: The modal structure of HAM. N_i denotes the aerosol number of the mode i and M_i^j denotes the mass of compound $j \in \{SU, BC, POM, SS, DU\}$ in mode i. The ranges for $\bar{r}$ give the respective mode boundaries (see Section 2.2.7).

2.2.3 Emission Module

With the exception of the sulfur compounds, all emissions are treated as primary emissions, i.e. the compounds are assumed emitted as particulate matter. This is a realistic assumption for most of the treated species. However, it is only a proxy for the particulate fraction of organic matter. The prognostic treatment of the aerosol size-distribution requires the knowledge of the emission size-distribution. Additionally, the application of emissions in a GCM implies the assumption of homogeneous mixing across the model grid box with a typical scale of more than 100 km. The emissions of dust, sea salt and oceanic dimethyl sulfide (DMS) are calculated online. Terrestrial biogenic DMS emissions are prescribed. For all other compounds, emission strength, distribution, and height are based on the AEROCOM (http://nansen.ipsl.jussieu.fr/AEROCOM/) emission inventory for the aerosol model inter-comparison experiment B (Frank Dentener, *in preparation*) representative for the year 2000. This emission inventory is henceforth denoted as ACB.

Species	Source	Reference	Tg yr^{-1}
DMS	Marine Biosphere	Kettle and Andreae (2000) Nightingale et al. (2000)	23.4
	Terrestrial Biosphere	Pham et al. (1995)	0.3
SO_2	Volcanoes	Andres and Kasgnoc (1998) Halmer et al. (2002)	14.6
	Vegetation Fires	van der Werf et al. (2003)	2.1
	Industry, Fossil-Fuel, Bio-Fuels	Cofala et al. (2005)	54.2
Total sulfur			94.6
BC	Vegetation Fires	van der Werf et al. (2003)	3.0
	Fossil-Fuel	Bond et al. (2004)	3.0
	Bio-Fuels	Bond et al. (2004)	1.6
Total BC			7.7
POM	Biogenic	Guenther et al. (1995)	19.1
	Vegetation Fires	van der Werf et al. (2003)	34.7
	Fossil-Fuel	Bond et al. (2004)	3.4
	Bio-Fuels	Bond et al. (2004)	9.1
Total POM			66.3
SS	Wind driven	Schulz et al. (2004)	
Accumulation			54.3
Coarse			4977.8
Total			5032.1
DU	Wind driven	Tegen et al. (2002)	
Accumulation			7.5
Coarse			654.9
Total			662.4
alternative:		Balkanski et al. (2004)	
Total			787.1

Table 2.2: Global annual aerosol and aerosol-precursor emissions in Tg yr^{-1} and Tg(S) yr^{-1} for sulfuric species.

The emission scenario is summarised in Table 2.2 and explained in more detail in the following paragraphs.

Sulfur Emissions We consider natural DMS emissions from the marine biosphere. The emission flux is calculated interactively from DMS seawater concentrations of Kettle and Andreae (2000) utilising the ECHAM5 10 m wind speed to derive the air-sea exchange rate following Nightingale et al. (2000). Terrestrial biogenic emissions in form of DMS are applied from Pham et al. (1995). Non-eruptive volcanic sulfur emissions are taken from Andres and Kasgnoc (1998) supplemented by eruptive emissions with locations following Halmer et al. (2002) and a total strength recommended by GEIA (http://www.geiacenter.org). Non-eruptive emissions are distributed between the volcano height and one third below, eruptive emissions are distributed 500 to 1500 m above the volcano height (ACB). Anthropogenic sulfur emissions are considered from fossil-fuel and bio-fuel emissions (Cofala et al., 2005) and from vegetation fires (van der Werf et al., 2003). Emissions from industry, power-plants, and shipping are distributed between 100 and 300 m above surface (ACB). Vegetation fires inject emissions in heights well above the surface. We account for that, following ACB, by prescribing emission profiles derived from measured ecosystem specific injection heights (David Lavoué, *pers. comm.*), ranging from 0 to

6 km. Except for DMS, we assume 97.5 % of all sulfuric emission in the form of SO_2 and 2.5 % in the form of primary sulfate (ACB). 50 % of ship-, industrial-, and power-plant emissions are attributed to the accumulation mode with a number median radius $\bar{r} = 0.075$ μm and $\sigma = 1.59$ and 50 % to the coarse mode with $\bar{r} = 0.75$ μm and $\sigma = 2.00$ (estimated from ACB recommendation of $\bar{r} = 0.5$ μm and $\sigma = 2.0$). Other primary sulfate emissions are attributed with 50 % to the Aitken mode with $\bar{r} = 0.03$ μm and $\sigma = 1.59$ and with 50 % to the accumulation mode with $\bar{r} = 0.075$ and $\sigma = 1.59$.

Carbonaceous Emissions Fossil-fuel and bio-fuel emissions for black and organic matter are used from Bond et al. (2004) assuming an emission size distribution with a number median radius of $\bar{r} = 0.03$ μm and $\sigma = 1.59$ (adapted to ECHAM5-HAM standard deviation from ACB recommendation $\bar{r} = 0.015$ μm and $\sigma = 1.8$). For carbonaceous emissions from vegetation fires (van der Werf et al., 2003) we assume $\bar{r} = 0.075$ μm and $\sigma = 1.59$ (adapted from ACB values $\bar{r} = 0.04$ μm and $\sigma = 1.8$) and injection heights as described in Section 2.2.3. The biogenic monoterpene emissions of Guenther et al. (1995), are scaled by the factor 0.15 to estimate the production of Secondary Organic Aerosol (SOA) from biogenic sources (ACB). Black carbon emissions are assumed insoluble. 65 % of all POM emissions are assumed soluble (Mayol-Bracero et al., 2002) and emitted in the respective soluble mode, the insoluble fraction in the insoluble Aitken mode. The insoluble fraction of SOA is assumed to condense on the insoluble Aitken mode and the soluble fraction on the soluble Aitken and accumulation modes at the point of emission. For the conversion of the carbon mass of POM into the total mass of POM, a factor of 1.4 is applied (ACB). Considering the associated uncertainties and the simplified bulk treatment, hygroscopic growth of organic aerosols is currently neglected.

Sea salt emissions Sea salt aerosol is produced by wind-induced formation of sea spray and its subsequent (partly) evaporation (e.g. Schulz et al., 2004). Numerous emission source functions have been developed, parameterising the emission flux as a function of the 10 m wind speed. Guelle et al. (2001) show that the emission source function can best be represented by a combination of the approach of Monahan et al. (1986) for the small particle range and of Smith and Harrison (1998) for the coarse particle range. Following their approach we merge the source functions smoothly in the size range 2 - 4 μm dry radius and fit the combined source function by two lognormal distributions. The mass median radii as a function of wind speed decrease with increasing wind speed of 1 to 40 m s^{-1} from 0.284 to 0.271 μm and from 2.25 to 2.15 μm for the two modes, respectively (Schulz et al., 2004).

Dust Emissions For the emission of mineral dust, two optional schemes have been implemented into HAM: the scheme of Tegen et al. (2002) and the scheme of Balkanski et al. (2004). Both schemes are coupled online, i.e. they calculate the emission of mineral dust in dependence of the ECHAM5 wind speed and hydrological parameters. Freshly emitted dust is assumed insoluble. Tegen et al. (2002) derive preferential dust source areas from an explicit simulation of paleological lakes. In addition, lower dust emissions can occur in other non-vegetated regions. The emission flux is then calculated from 192 internal dust size-classes and the explicit formulation of the saltation process following Marticorena and Bergametti (1995). Balkanski et al. (2004) have associated threshold velocities derived by Marticorena and Bergametti (1995) to the mineralogical composition of the different soil types of the Food and Agriculture Organization of the United Nations (http://www.fao.org) over the same region. This allowed to extend the domain to obtain a global dust source formulation (Claquin, 1999). In addition, regional source

strength were deduced for 12 arid regions by adjusting model optical depth to optical depth deduced from TOMS aerosol indices (Hsu et al., 1999).
For the implementation of the Tegen et al. (2002) scheme into ECHAM5-HAM, we fitted a multi-annual global mean of the emission size classes grouped into 24 bins with a superposition of three log-normal size-distributions. Considering the short life-time and the negligible contribution of the super-coarse mode to the radiative effect, we neglect the super-coarse mode emissions and apply the emission into the insoluble accumulation and coarse modes with mass-median radii of 0.37 μm and 1.75 μm and standard deviations of 1.59 and 2.00, respectively. For the Balkanski et al. (2004) scheme we also neglect the super-coarse mode emissions and emit into the insoluble coarse mode with a mass-median radius of 1.25 μm and a standard deviation of 2.00.
A full description and comparison of the results of the two dust schemes is beyond the scope of this paper. Thus, unless otherwise quoted, we will focus henceforth on the results from the Tegen et al. (2002) scheme.

2.2.4 Chemistry Module

The chemistry module is based on the sulfur cycle model as described by Feichter et al. (1996) treating the prognostic variables dimethyl sulfide (DMS), sulfur dioxide (SO_2) and sulfate (SO_4^{2-}). Three dimensional monthly mean oxidant fields of OH, H_2O_2, NO_2, and O_3 are prescribed from calculations of the comprehensive MOZART chemical transport model (Horowitz et al., 2003). In the gas phase, DMS and SO_2 are oxidised by hydroxyl (OH) and DMS reacts with nitrate radicals (NO_3). In the aqueous phase the oxidation of SO_2 by H_2O_2 and O_3 are considered. The aqueous phase concentration of SO_2 is calculated according to Henry's law, accounting for dissolution effects.
Gas-phase produced sulfate is attributed to the gaseous phase and allowed to condense on pre-existing particles or to nucleate by the aerosol microphysics module M7 (see Section 2.2.7). In the current model version, in-cloud produced sulfate is distributed to the available pre-existing accumulation mode and coarse mode aerosol particles according to the respective number concentrations. A more detailed treatment of in-cloud aerosol processing is subject of ongoing research activities and will be described in forthcoming publications.

2.2.5 Deposition Module

Dry Deposition

The net surface fluxes, calculated by subtracting the dry deposition fluxes from the respective emission fluxes, provide the lower boundary conditions for the implicit vertical diffusion scheme of ECHAM5. The dry deposition flux is calculated as the product of the surface layer concentration and the dry deposition velocity:

$$F_d = C \rho_{air} v_d \tag{2.2}$$

where C is the tracer mass or number mixing ratio, ρ_{air} is the air density, and v_d is the dry deposition velocity. The dry deposition velocities are calculated based on a serial resistance approach.
For gases, v_d is calculated from the aerodynamic, quasi-laminar boundary layer, and surface resistance according to the "big leaf" concept (Ganzeveld and Lelieveld, 1995; Ganzeveld et al., 1998) for the ECHAM5 fractional surface cover types (snow/ice, bare soil, vegetation, wet skin, water and sea ice) of each grid box. The surface resistances are generally prescribed except of

some specific resistances, e.g. the SO_2 soil resistance as a function of soil pH, relative humidity, surface temperature, and the canopy resistance. The latter is calculated from ECHAM5's stomatal resistance and a monthly mean Leaf Area Index (LAI) inferred from a NDVI (Normalised Differential Vegetation Index) climatology (Gutman et al., 1995) and the Olson (1992) ecosystem database.
For aerosols we have implemented the dry deposition velocity model that has previously been applied to develop a sulfate aerosol dry deposition parameterisation (Ganzeveld et al., 1998). In contrast to using prescribed sulfate mass size distributions, which were used to develop the sulfate aerosol dry deposition parameterisation, we use in this study the explicitly calculated modal number and mass parameters to calculate the aerosol dry deposition velocity as a function of particle radius, density, turbulence, and surface cover properties. The dry deposition model calculates the bare soil and snow/ice aerosol dry deposition velocities according to Slinn (1976), over water according to Slinn and Slinn (1980), whereas the vegetation and wet skin aerosol dry deposition velocities are calculated according to Slinn (1982) and Gallagher et al. (2002). Over water, the effect of whitecaps in enhancing aerosol dry deposition according to Hummelshøj et al. (1992) is taken into account.

Sedimentation

Sedimentation of the aerosol particles is calculated throughout the atmospheric column. The calculation of the sedimentation velocity is based on the Stokes velocity

$$v_s = \frac{2}{9}\frac{r^2 \rho g C_c}{\mu} \tag{2.3}$$

with the Cunningham slip-flow correction factor C_c accounting for non-continuum effects (e.g. Seinfeld and Pandis, 1998):

$$C_c = 1 + \frac{\lambda}{r}\left[1.257 + 0.4\exp -\frac{1.1r}{\lambda}\right] \tag{2.4}$$

Here v_s is the sedimentation velocity, r the number or mass median radius, ρ the particle density, g the gravitational acceleration, μ the gas viscosity, and λ the mean free path of air. To satisfy the Courant - Friedrich - Lewy stability criterion, the sedimentation velocity is limited to $v_s < \frac{\Delta z}{\Delta t}$ where Δz is the layer thickness and Δt is the model timestep.

Wet Deposition

The fraction of scavenged tracers is calculated from the in-cloud content utilising the precipitation formation rate of the ECHAM5 cloud scheme. For gases, the partitioning between the air and the cloud water is calculated based on Henry's law (see e.g. Seinfeld and Pandis, 1998) whilst for aerosols it is prescribed in the form of a size- and composition-dependent scavenging parameter R. R is defined as the fraction of the tracer in the cloudy part of the grid box that is embedded in the cloud liquid/ice water. Values of R for stratiform clouds follow measurements of interstitial and in-cloud aerosol contents of Henning et al. (2004), with slight modifications, and for ice clouds are based on Feichter et al. (2004). It should be noted that for the accumulation and coarse mode R is lower for mixed phase clouds than for liquid clouds due to the growth of ice crystals at the expense of water droplets as a result of the Bergeron-Findeisen process (Henning et al., 2004). For convective clouds, few size-resolved measurement data is available. Thus,

assuming higher supersaturations and therefore activation into lower size-ranges, we increase R in convective clouds for the soluble modes, which we assume to be potential cloud condensation nuclei. The prescribed values of R are given in Table 2.3.

Mode	**Stratiform** Liquid Clouds	**Stratiform** Mixed Clouds	**Stratiform** Ice clouds	**Convective** Mixed Clouds
Nucleation Soluble	0.10	0.10	0.10	0.20
Aitken Soluble	0.25	0.40	0.10	0.60
Accumulation Soluble	0.85	0.75	0.10	0.99
Coarse Soluble	0.99	0.75	0.10	0.99
Aitken Insoluble	0.20	0.10	0.10	0.20
Accumulation Insoluble	0.40	0.40	0.10	0.40
Coarse Insoluble	0.40	0.40	0.10	0.40

Table 2.3: Scavenging parameter R for the modes of HAM

For the scavenging by stratiform clouds, the local rate of change of tracer i is calculated as:

$$\frac{\Delta C_i}{\Delta t} = \frac{R_i C_i f^{cl}}{C_{wat}} \left(\frac{Q^{liq}}{f^{liq}} + \frac{Q^{ice}}{f^{ice}} \right) \tag{2.5}$$

where C_i, C_{wat} are mixing ratios of the tracer i and total cloud water, respectively. f^{cl} is the cloud fraction, f^{liq} and f^{ice} are the liquid- and ice fraction of the cloud water. Q^{liq} and Q^{ice} are the respective sum of conversion rates of cloud liquid water and cloud ice to precipitation, via the processes auto-conversion, aggregation, and accretion.
Convective scavenging is coupled with the mass flux scheme of the convective tracer transport. In addition to the local change of the tracer tendency, the convective tracer fluxes have to be adjusted by the wet deposition. In convective updrafts the tracer mixing ratios are associated with the liquid- and ice-phase proportionally to the presence of the respective phase:

$$C_i^{liq} = C_i f^{liq} \qquad C_i^{ice} = C_i f^{ice} \tag{2.6}$$

The change in tracer mixing ratio is calculated as

$$\Delta C_i = \Delta C_i^{liq} + \Delta C_i^{ice} = C_i^{liq} R_i E^{liq} + C_i^{ice} R_i E^{ice} \tag{2.7}$$

where R_i is the scavenging parameter and E^{liq} and E^{ice} are the fractions of updraft liquid water and updraft ice water that are converted into precipitation during one timestep.
From the local ΔC_i for each layer k the local grid-box mean deposition flux $\overline{F_i^{dep}}$ and the grid-box mean tendency $\overline{\Delta C_i}/\Delta t$ are calculated:

$$\overline{F_i^{dep}} = \Delta C_i \overline{F^{up}} \qquad \frac{\overline{\Delta C_i}}{\Delta t} = \overline{F_i^{dep}} \frac{g}{\Delta p} \tag{2.8}$$

Here $\overline{F^{up}}$ is the grid-box mean updraft mass flux. The local deposition flux is integrated from the model top to the respective layer k:

$$\overline{F_i^{dep}}^{int} = \sum_{top}^{k} \overline{F_i^{dep}} \tag{2.9}$$

The mean updraft tracer flux $\overline{F_i^{up}}$ for tracer i is recalculated based on the updated updraft tracer mixing ratios:

$$\overline{F_i^{up}} = (C_i - \Delta C_i)\,\overline{F^{up}} \tag{2.10}$$

A non-negligible fraction of precipitation re-evaporates before it reaches the ground. Re-evaporation acts on the integrated tracer deposition flux $\overline{F_i^{dep}}^{int}$ proportionally to the evaporation of precipitation:

$$\Delta\overline{F_i^{dep}}^{int} = \overline{F_i^{dep}}^{int} f^{evap} \tag{2.11}$$

$$\frac{\overline{\Delta C_i}}{\Delta t} = \Delta\overline{F_i^{dep}}^{int} \frac{g}{\Delta p} \tag{2.12}$$

where f^{evap} is the evaporating fraction of precipitation, Δp is the layer thickness in pressure units, and g is the gravitational acceleration.
For aerosols, below-cloud scavenging is calculated from the ECHAM5 water- and ice- precipitation fluxes with prescribed size-dependent collection efficiencies R_i^r and R_i^s from Seinfeld and Pandis (1998) for rain and snow, normalised by the respective precipitation rate

$$\frac{\overline{\Delta C_i}}{\Delta t} = C_i^{amb} f^{precip} \left(R_i^r F^r + R_i^s F^s\right) \tag{2.13}$$

where C_i^{amb} is the mass mixing ratio of the ambient cloud free air, f^{precip} is the effective grid-box fraction affected by precipitation, and F^r and F^s are the fluxes of rain and snow, respectively. f^{precip} is estimated in the stratiform scheme by the assumption of maximum overlap of the cloudy parts of the grid box and for the convective scheme from the estimated updraft area.

2.2.6 Relative Humidity

Sub-grid scale variations in relative humidity can have a large impact on the water uptake of aerosols and their radiative forcing (e.g. Haywood et al., 1997a). As cloud processing of aerosols and cloud radiative effects predominate in the cloudy part of the grid box, it is desirable to apply ambient conditions for the aerosol microphysics and thermodynamics in the cloud free part. The usage of the grid mean relative humidity $\overline{RH} = \overline{q}/q^s$ leads to an overestimation of RH in the cloud free part of a partly clouded grid box. The cause is that it can be assumed that air in the cloudy part of the grid box is close to saturation. Here $\overline{q}$ and q^s are grid-mean and saturation specific humidities, respectively. This assumption allows to calculate the relative humidity in the cloud-free part of the grid box:

$$RH^{amb} = \frac{q^{amb}}{q^s} \tag{2.14}$$

where the ambient specific humidity q^{amb} is calculated from

$$\overline{q} = q^s f^{cl} + q^{amb}(1 - f^{cl}) \tag{2.15}$$

where f^{cl} is the cloud fraction.
Turbulent sub-grid scale fluctuations of RH are not accounted for in this study.

2.2.7 The Aerosol Microphysics Module M7

The microphysical core of the ECHAM5-HAM aerosol model is the aerosol module M7 (Vignati et al., 2004) evolving from an earlier version M3+ that has already been used and tested in global aerosol modelling studies with offline chemical transport models (Wilson et al., 2001). M7 treats the aerosol dynamics and thermodynamics in the framework of the modal structure that is described in the Section 2.2.2. Only the major processes in M7 are described here as a thorough description and evaluation of M7 can be found in Vignati et al. (2004).

Coagulation

The calculation of the coagulation coefficients is based on a parameterisation of the Brownian coagulation following Fuchs (1964). The coagulation coefficient for particles of modes i and j is:

$$K_{ij} = \frac{16\pi\tilde{r}\tilde{D}}{\frac{4\tilde{D}}{\tilde{\nu}\tilde{r}} + \frac{\tilde{r}}{\tilde{r}+\tilde{\Delta}}} \tag{2.16}$$

where $\tilde{D}$, $\tilde{\nu}$ and $\tilde{\Delta}$ are the diffusion coefficient, the thermal velocity and the mean free path length for particles with a mean radius of $\tilde{r} = \frac{\bar{r_i}+\bar{r_j}}{2}$, respectively.

Condensation

Under sulfate-limited conditions, the condensation on potentially pre-existing particles and the nucleation of new particles compete for the available gas phase sulfuric acid. The partitioning of sulfate between those processes is treated in M7 as follows:
In a first step, the total maximum amount of condensable sulfate on pre-existing particles is calculated. This process is limited by the availability of gas phase sulfate and the diffusion of the sulfate to the surface of the particles. The calculation follows the methodology of Fuchs (1959) matching the diffusion in the kinetic and continuous regimes. The distinction between condensation on insoluble and on mixed/insoluble particles is realized by the assumption of different accommodation coefficients of $\alpha = 0.3$ for the insoluble and $\alpha = 1.0$ for the soluble particles (see Vignati et al., 2004).
In the second step, the remaining gas phase sulfate is available for the nucleation of new clusters.

Nucleation

The calculation of the number of nucleated particles is based on the classical nucleation theory in the binary sulfate / water system accounting for the effects of hydratisation. From the parameters temperature (T), relative humidity (RH), as well as the gas-phase concentration of the sulfate available after the condensation the number of nucleated particles as well as the integral mass of the nucleated sulfate is parameterised following Vehkamäki et al. (2002). Compared to the earlier tested and optionally available scheme by Kulmala et al. (1998) this scheme has the advantage of an extended range of thermodynamical conditions (0.01 % $< RH <$ 100 %, 230.15 K$< T <$ 305.15 K) and the usage of a more stringent application of nucleation theory. The predicted nucleation rate is then integrated analytically to calculate the number of nucleated particles over one timestep. The corresponding nucleated mass of sulfate is then derived based on the predicted nucleation cluster size starting at four molecules.

Thermodynamics

For particles containing sulfate, the calculation of the thermodynamical equilibrium with the water vapour phase is based on a generalised form of the Kelvin equation. For computational efficiency the parameterisation is realized in form of a look-up table. The calculation of the water content of particles that contain beside sulfate insoluble components, such as dust or black carbon, is done analogous to pure sulfate particles but with the dry radii of the total compounds.
With increasing ambient relative humidity, when the humidity reaches the Deliquescence Relative Humidity (DRH), particles containing sea salt grow spontaneously by water uptake from the surrounding air. With decreasing ambient humidity, the sea salt aerosol releases the up-taken water not until a relative humidity well below the DRH, the so called Efflorescence Relative Humidity (ERH). This hysteresis phenomenon is not taken into account in the current version of M7. In fact, as sea-salt aerosol is formed from the evaporation of larger droplets, it is assumed that particles do not release their water down to $ERH = 45$ % (from Tang (1997)). The aerosol water content of particles containing sea salt in conditions of $RH > ERH$ is calculated as follows.

$$W = \sum_i \frac{c_i}{m_i} \tag{2.17}$$

Here are W the aerosol water content [$\mathrm{g\,m^{-3}}$], c_i concentration of compound i [$\mathrm{mol\,m^{-3}}$] and m_i the binary molality of compound i [$\mathrm{mol\,g^{-1}}$]. It is assumed, based on the ZSR-Relation (Zadanovskii, 1948; Stokes and Robinson, 1966), that the water activity of mixtures of electrolytes is equal to the water activity of the binary electrolyte-water mixture. The calculation of the binary molalities is done as follows

$$m_i = \left(\sum_{j=0}^{7} Y_j \ (RH)^j \right)^2 \tag{2.18}$$

where RH is the relative humidity (water activity) and Y_j are empirical coefficients from Jacobson et al. (1996).

Integration of the Aerosol Dynamics Equation

Analytical solutions are applied to integrate the aerosol dynamics equation for each mode, calculating the updated aerosol numbers and the transfer between the modes.
The aerosol dynamics equation for the soluble modes ($1 \leq i \leq ns$) can be expressed as:

$$\begin{aligned} \frac{dN_i}{dt} &= -\frac{1}{2} K_{ii} N_i^2 \\ &\quad -N_i \left[\sum_{j=i+1}^{ns} K_{ij} N_j + \sum_{j=i+ns}^{ns+ni} K_{ij} N_j \right] + \delta_{i1} c \end{aligned} \tag{2.19}$$

The first term on the right hand side represents the intra-modal coagulation, the second term the inter-modal coagulation and the third term the nucleation. Here N_i is the particle number, K_{ij} the coagulation coefficient for the coagulation of mode i and mode j, and c the nucleation

rate. The inter-modal coagulation consists of a contribution of coagulation with larger soluble modes as well as a contribution of coagulation with particles of larger insoluble modes.
For the insoluble modes, the coagulation also with smaller soluble particles is a sink as in this case the particles are transferred to the soluble/mixed mode. The coagulation with higher insoluble modes however, is considered inefficient for the insoluble modes. Therefore, the aerosol dynamics equation for the insoluble modes ($ns + 1 \leq i \leq ns + ni$) can be expressed as

$$\frac{dN_i}{dt} = -\frac{1}{2} K_{ii} N_i^2 - N_i \left[\sum_{j=1}^{ns} K_{ij} N_j \right] \tag{2.20}$$

For the insoluble dust modes, the first term on the right hand side, representing the intra-modal coagulation, is negligible and thus omitted. The second term of the right hand side, accounting for the inter-modal coagulation with soluble modes, is treated operator split in a subsequent procedure (see Section 2.2.7 and Vignati et al. (2004) for more details).
From the analytically integrated changes in the aerosol numbers, the corresponding aerosol mass concentrations are then calculated mass conserving by summing up the number of particles transferred between the modes and multiplication with the respective mean particle masses.

Transfer From the Insoluble- to the Mixed-Modes

Particles in the insoluble modes are transformed to the corresponding soluble/mixed mode by condensation of sulfate on their surface or by coagulation with particles of soluble modes. The total condensable sulfate on the respective mode (see 2.2.7) and the sulfate added to this mode by coagulation are attributed to the number of particles that can be coated with a minimal layer of sulfate. We assume a mono-layer for this minimal layer thickness (see Vignati et al., 2004). Particle numbers and masses of the coated particles, as well as the sulfate mass available through condensation and coagulation, are then transferred to the corresponding soluble mode.

Repartitioning Between the Modes

The previously described processes would cause a significant overlap between the modes. For example, nucleation mode particles typically grow by coagulation and condensation via the Aitken mode into the accumulation mode. Numerically, this leads to the fact that the mode median radius, but also the mode standard deviation, would increase steadily, associated with numerical diffusion. A mode merging algorithm (Vignati et al., 2004) is applied to repartition the particles among the modes and to confine the number median radius of each mode to the range given in Table 2.1.

2.2.8 Radiation Module

The prognostic treatment of size-distribution, composition, and mixing state allows the explicit calculation of the aerosol optical properties in the framework of the Mie theory. However, the online calculation of the aerosol optical properties is computationally expensive. Therefore, the required aerosol optical properties are pre-computed from Mie theory for 24 solar spectral bands, following Toon and Ackerman (1981), and supplied in look-up tables with the three dimensions: Mie size-parameter ($X = 2\pi r/\lambda$), and real- and imaginary part (n_r and n_i) of the refractive index. Here r is the number median radius of the log-normal mode and λ is the wavelength. The geometric arrangement of internally mixed components can be complex. Without prior

knowledge we approximate (n_r) and (n_i) for each mode by a volume weighted average of the refractive indices of the components, including the diagnosed aerosol water (WAT) (see 2.2.7). The error of this approximation on n_r is typically negligible and can reach ≈ 15 % for n_i for the extreme case of a mixture of BC and WAT (Lesins et al., 2002). Table 2.4 lists the used refractive indices for the components at $\lambda = 550$ nm. Note that for dust the derivation of n_i from AERONET measurements (Kinne et al., 2003) results in a significantly reduced absorption compared to earlier estimates (e.g. Moulin et al. (1997): $n_i = 1.0 \times 10^{-2}\ i$ at $\lambda = 550$ nm) and used in most previous studies (e.g. Schulz et al., 1998; Chin et al., 2002).

Species	Refractive Index	Reference
SU	$1.43 + 1.0 \times 10^{-8}\ i$	Hess et al. (1998)
BC	$1.75 + 4.4 \times 10^{-1}\ i$	Hess et al. (1998)
POM	$1.53 + 5.5 \times 10^{-3}\ i$	Koepke et al. (1997)
SS	$1.49 + 1.0 \times 10^{-6}\ i$	Shettle and Fenn (1979)
DU	$1.52 + 1.1 \times 10^{-3}\ i$	Kinne et al. (2003)
WAT	$1.33 + 2.0 \times 10^{-7}\ i$	Downing and Williams (1975)

Table 2.4: Complex refractive index by component at $\lambda = 550$ nm.

The table lookup procedure provides extinction cross section, single scattering albedo, and assymetry factor for each mode. The values from the 24 solar spectral bands are mapped to the 4 solar ECHAM5 bands, weighted with bottom of the atmosphere clear-sky solar fluxes. The parameters for the seven aerosol modes are combined to provide the necessary input to the ECHAM5 radiation scheme. In this study, only the effect of aerosols on the solar part of the spectrum is considered.

2.3 Results and Evaluation

The simulations are performed for the year 2000 after a spin-up period of four months. ECHAM5 is nudged to the ECMWF ERA40 reanalysis data (Simmons and Gibson, 2000). Horizontally, the resolution is T63 in spectral space with a corresponding resolution of $1.8° \times 1.8°$ on a Gaussian grid. The vertical resolution is set to 31 levels, extending from the surface up to 10 hPa. The prescribed emissions have the base year 2000.
Up to date, only limited measurement datasets of the global aerosol distribution are available. In situ measurements, in particular from aircraft campaigns, provide valuable reference cases for the model performance. However, their limited temporal and spatial extent complicate a comparison with global aerosol model simulations. Satellite measurements are currently still limited to integral properties, such as aerosol optical depth (AOD) and the Ångström parameter. The absence of continuous global measurements with a vertical extent render a full validation of the simulated global mean aerosol distribution impossible. Nevertheless, the attempt is made to evaluate the simulations by comparing a wide range of simulated parameters with available measurements.

2.3.1 Emissions

Annual mean emission distribution by species and global annual totals are depicted in Figure 2.1. The partitioning by source type is given in Table 2.2. Emissions of the sulfuric compounds sulfur dioxide, sulfate, and DMS are displayed in terms of emissions of sulfur. The local maxima of sulfuric emissions can be attributed to anthropogenic emissions in the northern hemisphere.

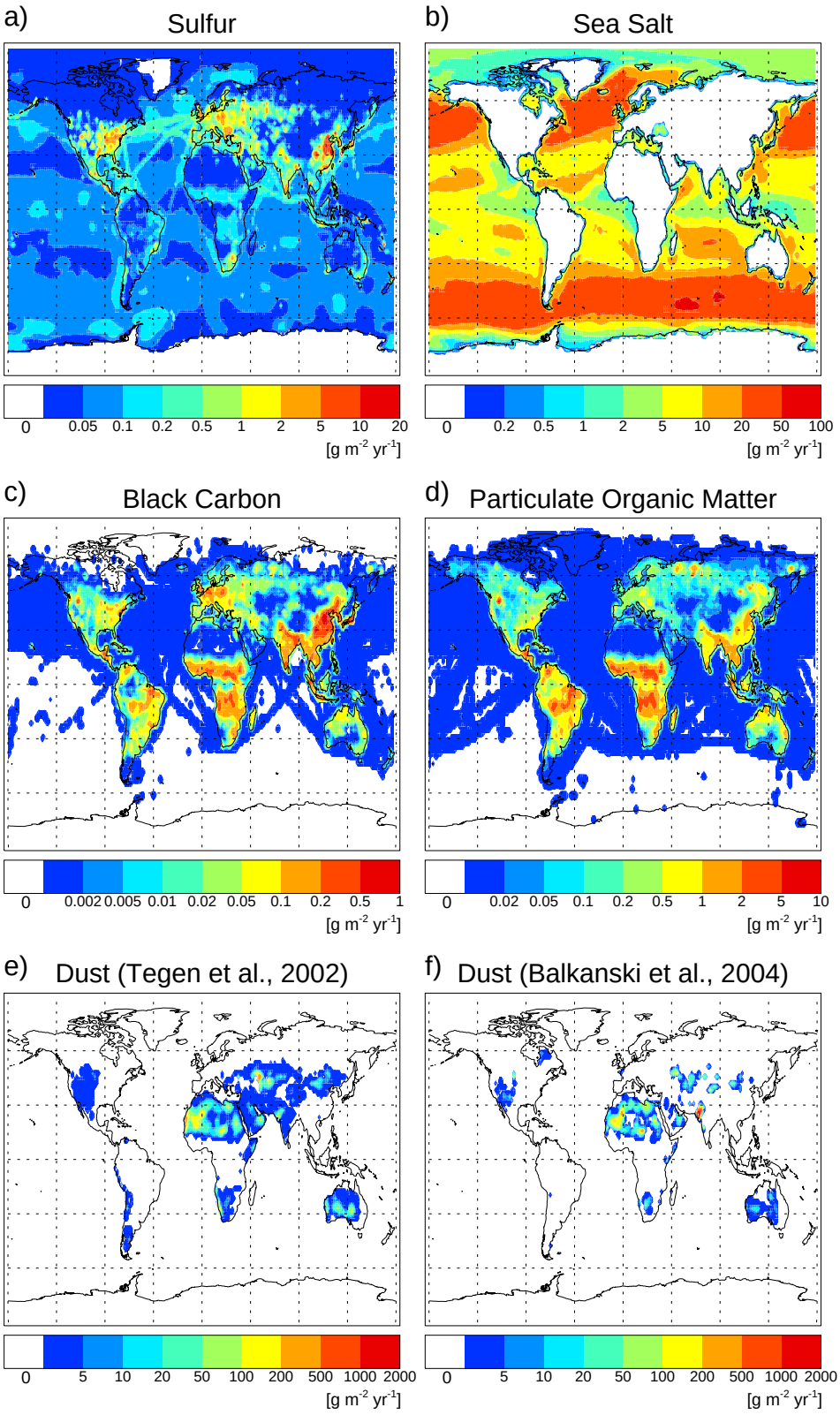

Figure 2.1: Annual mean emission distribution by species. For dust emissions results of the Tegen et al. (2002) scheme and of the Balkanski et al. (2004) scheme are displayed.

However, in the global mean, 40.9 % of total sulfuric emissions have a natural origin with 24.6 % from the marine biosphere, 15.3 % from volcanoes, and 0.95 % from the terrestrial biosphere. Vegetation fire emissions are considered here as anthropogenic. The regions of highest sea salt emissions coincide with the oceanic storm-track regions. The dominant contribution to the BC emissions is from fossil- and bio-fuel usage with 61.0 %, supplemented by vegetation fires with 39.0 %. Vegetation fires dominate the POM emissions with a contribution of 52.3 % followed by biogenic and fossil- and bio-fuel emissions with 28.8 % and 18.9 %, respectively. For mineral dust, results from the Tegen et al. (2002) and Balkanski et al. (2004) schemes are displayed. Both schemes show a region of intense dust emissions over North Africa and agree in the large scale emission patterns. However, the Balkanski et al. (2004) emissions are generally patchier. Regionally the differences are not negligible. The Balkanski et al. (2004) scheme produces a distinct maximum of dust emissions in the region of the Thar desert in North-West India and the Tegen et al. (2002) scheme higher emissions in the Caspian Sea region, eastern Asia, western South-America, and Australia.

2.3.2 Budgets and Lifetime

The components of the simulated ensemble of multiple internally-mixed aerosol modes are not independent as in classical bulk aerosol models, since microphysical processes affect the components of each internally mixed mode likewise. However, the summation of the budgets of the components over all modes gives insight in their cycling and facilitates the comparison with results from other studies. Annual mean total sources, column burden, lifetime, and sink processes as sum for each aerosol compound and precursors are listed in Table 2.5. Hereby, the lifetime is estimated as the ratio of the column burden to the total sources. The sulfate burden lies with 0.80 Tg in the range of previous estimates (Langner and Rhode (1991): 0.77 Tg; Feichter et al. (1996): 0.57 Tg; Chin et al. (1996): 0.53 Tg; Roelofs et al. (1998): 0.96 Tg, Lohmann et al. (1999b): 1.03, Rasch et al. (2000): 0.60 Tg), as lies the lifetime with 3.9 days (Langner and Rhode (1991): 5.3 days; Feichter et al. (1996): 4.3 days; Chin et al. (1996): 3.9 days). As shown in Ganzeveld et al. (1998), the usage of their serial resistance dry deposition scheme results in significantly lower SO_2 dry deposition (here 16.3 % of total sink) than in many previous studies. This yields a relatively high burden of SO_2 of 0.67 Tg, contributes to the relatively high burden of sulfate, and leaves the chemical conversion with 79.5 % as the dominating sink for SO_2. Of the gas-phase produced sulfuric acid, 99.4 % condenses on pre-existing aerosol, 0.4 % nucleates and 0.2 % is wet deposited. The DMS burden lies with 0.077 Tg in the range of previous estimates (Feichter et al. (1996): 0.102 Tg; Chin et al. (1996): 0.059 Tg). For BC and POM the simulated burdens of 0.11 Tg and 0.99 Tg, respectively, are lower than previous estimates, e.g. Lohmann et al. (1999a): 0.26 Tg, Wilson et al. (2001): 0.22 Tg, Chung and Seinfeld (2002): 0.22 Tg for BC, and e.g. Lohmann et al. (1999a): 1.87 Tg, Chung and Seinfeld (2002): 1.39 Tg for POM, respectively. This is consistent with the lower emissions of BC of 7.7 Tg compared to 11.7 Tg in e.g. Lohmann et al. (1999a) and of POM of 66.1 Tg compared to 105 Tg in Lohmann et al. (1999a). The BC and POM lifetimes are with 5.4 days comparable with previous estimates (e.g. Lohmann et al., 1999a): 6.8 days for BC and 5.1 days for POM). For sea salt, with a burden of 10.5 Tg, a comparison with other studies is prevented by the fact that the emitted mass strongly depends on the assumed upper cut-off of the emissions size distribution. Due to its size and solubility, sea salt has the shortest lifetime with 0.8 days. The simulated dust burden is 8.28 Tg. The neglect of the super-coarse mode dust aerosol impedes the comparison of the budgets to other studies and results in a relatively long lifetime of 4.6 days. Wet deposition accounts to

55.3 % of the total sink, dry deposition to 5.5 %, and sedimentation to 39.2 %.
Microphysical aging, i.e coagulation with soluble particles and sulfate coating, transfers particles from the insoluble to the soluble modes. For the initially insoluble BC, 89 % of the mass is transfered to the soluble modes before removal, with a corresponding aging time of 0.7 days. This is faster than the pure condensational aging of pure BC with 1.4 days in Wilson et al. (2001). For the insoluble fraction of POM, for which a large fraction is emitted from biogenic sources in unpolluted areas, the aging is somewhat slower so that 86 % are aged, with an aging time of 1.1 days. With 4.8 days the aging time for the larger dust particles is longer, however, still 46 % are transfered to the soluble modes, with a subsequent increase of the scavenging efficiency, before removal.

Species	Total Sources [Tg yr^{-1}]	Burden [Tg]	Lifetime [days]
SU	76.1	0.80	3.9
BC	7.7	0.11	5.4
POM	66.1	0.99	5.4
SS	5032.2	10.50	0.8
DU	662.4	8.28	4.6
SO_2	92.0	0.67	2.7
SU_{gas}	28.0	0.00088	0.01
DMS	23.4	0.077	1.2

Species	Wet Deposition [%]	Dry Deposition [%]	Sedimentation [%]	Chemistry [%]	Condensation [%]	Nucleation [%]
SU	95.1	2.8	2.1			
BC	92.2	7.5	0.3			
POM	92.4	7.3	0.3			
SS	53.8	18.7	27.5			
DU	55.3	5.5	39.2			
SO_2	4.2	16.3		79.5		
SU_{gas}	0.2	0.0			99.4	0.4
DMS				100.0		

Table 2.5: Global annual mean sources, burden, lifetime and sinks of aerosols and their precursors. Mass units of sulfuric species are in Tg(S).

2.3.3 Mass Distribution

As for budgets and lifetime, the mass distributions of the internally-mixed components are coherent. Figure 2.2 shows the annual mean vertically integrated aerosol mass (burden) for each component as sum over the modes. The maxima of the sulfate burden lie close to the sources of sulfate and its precursors in the polluted regions of the northern hemisphere. However, substantial export of sulfate occurs to low emission regions such as the Middle East and northern Africa, the North Atlantic, and the North Pacific. The pronounced export to the Middle East and northern Africa seems facilitated by the usage of the interactive dry deposition scheme. As described in Ganzeveld et al. (1998), it calculates lower dry deposition velocities for SO_2 in that region than prescribed in many other studies, resulting in higher sulfate precursor concentrations.

Additionally, the consideration of low roughness velocities over bare soils also results in low aerosol dry deposition, which is a major sink in that region, characterised by low precipitation. The burden of dust shows a distinct maximum extending from the north-western African source regions into the Atlantic. The distribution of the carbonaceous compounds BC and POM resembles the emission distribution. Despite the dominant contribution of the storm tracks to the total sea salt emissions, sea salt burdens are also high over secondary source regions. The reason is that the storm tracks coincide with the strongest sink regions due to the associated precipitation. Therefore, regions such as the subtropical bands show, despite lower emissions, considerable column burdens of sea salt. Also shown is the burden of the total diagnosed aerosol water. From comparison with the distribution of the other compounds, it becomes evident that the dominant fraction of aerosol water is associated with sea salt. However, over regions with high sulfate burden the uptake by sulfate is discernible.

To evaluate the simulated mass distributions, we compare the modelled aerosol mass concentration of the lowest model level with surface measurements for the year 2000 from the European EMEP (http://www.emep.int) and North-American IMPROVE (http://vista.cira.colostate.edu/improve/) measurement networks as well as to measurements compiled by the Global Atmosphere Watch (GAW) program (http://ies.jrc.cec.eu.int/wdca/). As most of these stations are at continental sites, we also include the comparison with a climatological compilation of multi-annual measurements at remote marine sites by courtesy of J. Prospero and D. Savoie (University of Miami), henceforth denoted as University of Miami compilation.

To ensure comparability, stations deviating in height by more than 200 m from the lowest model level are rejected. For the year 2000 measurements from the EMEP, IMPROVE, and GAW networks, we sample the daily mean model output with the measurement occurrences, i.e. we include only days with measurements in the derivation of the model monthly mean values. Monthly means derived from less than 6 measurements are rejected. For the University of Miami dataset no information on the measurement dates and number of measurements is available. Thus we use the whole model monthly mean for the comparison. A list of the measurement locations, with corresponding model and measurement annual mean and standard deviation, and the total number of measurements can be found in Appendix A. Figure 2.3 shows scatterplots for the observed and simulated monthly mean surface mass concentrations for the different networks.

The comparison of SU with the North-American IMPROVE measurement sites shows a good agreement with a slight tendency to overestimate. Out of a total of 112 samples, 74 (66 %) agree within a factor of 2 with the measurements. In comparison with the EMEP stations, distributed over Europe, the overestimation is more pronounced. However, still 182 (64 %) out of 283 samples lie within a factor of 2. SU mass concentrations agree well with the GAW (7 (58 %) out of 12) and University of Miami compilations (196 (58 %) out of 336).

For BC, measurements are only available from the North American IMPROVE network. The simulated surface BC masses show a good agreement with the measurements. Out of a total of 115 samples, 75 (65 %) agree within a factor of 2. Considering the uncertainties associated with the SOA formation, the agreement for POM with 62 out of 115 samples (54 %) within a factor of 2, is remarkable.

SS mass concentrations compare well with the remote marine measurements of the University of Miami dataset (181 (63 %) out of 288 samples lie within a factor of 2 with the measurements) with a slight positive bias. Three measurement sites with exceptionally high SS concentrations have been rejected as they are likely contaminated by local surf (Dennis Savoie, *pers. comm.*).

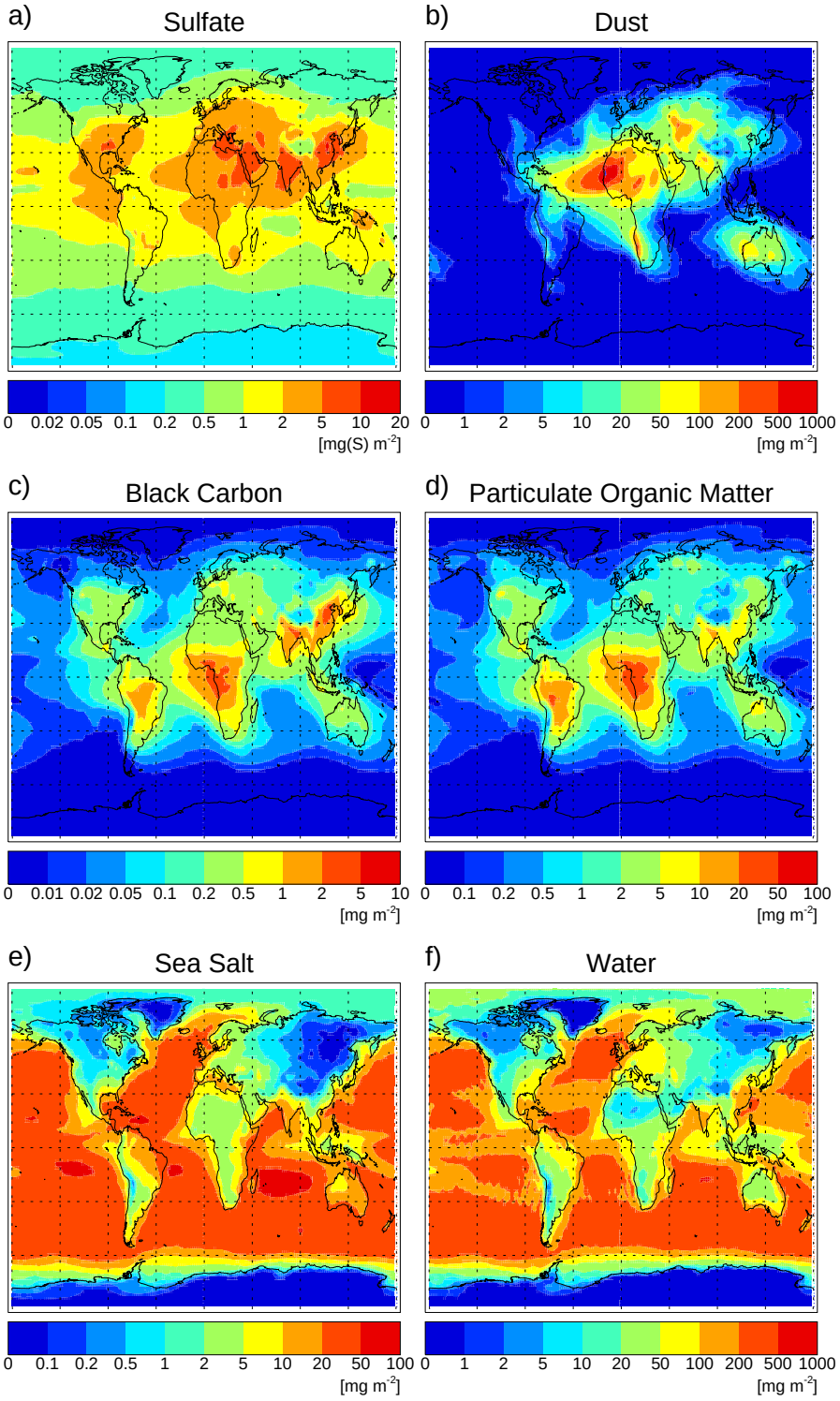

Figure 2.2: Annual mean vertically integrated column mass. The mass of sulfate is given in terms of sulfur mass.

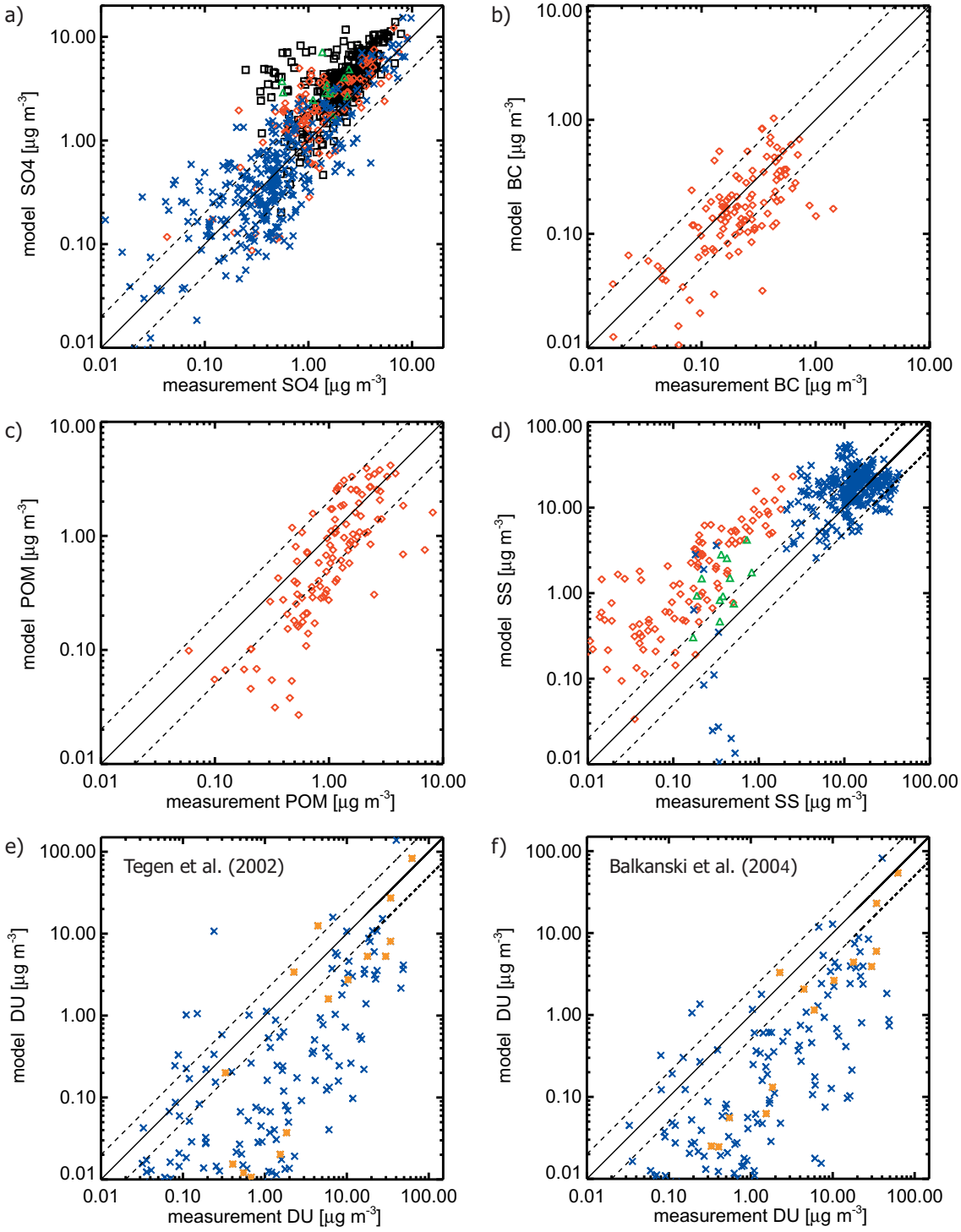

Figure 2.3: Scatter plot of simulated and measured monthly mean surface aerosol mass concentrations of a) sulfate , b) black carbon, c) particulate organic matter, d) sea salt, e) dust (Tegen et al., 2002), and f) dust (Balkanski et al., 2004). Units of sulfate are $\mu g(SO_4)$ m^{-3} and for the other compounds $\mu g\ m^{-3}$. EMEP measurements in black, IMPROVE in red, University of Miami in blue, and GAW in green. For dust, the month with the observed peak concentration is highlighted in orange. The solid line indicates the 1:1 ratio, the dashed lines the 2:1 and 1:2 ratios.

For the predominantly continental measurement sites from the IMPROVE and GAW networks, the low SS concentrations are substantially overestimated by the model, so that only 5 samples (4 %) out of 113 for IMPROVE and 3 samples (25 %) out of 12 for GAW agree within a factor of 2 with the measurements. This overestimation can possibly be attributed to numerical diffusion associated with the strong gradients of sea salt along the coast lines.

For the seasonal and inter-annual highly variable dust cycle, the comparison with the climatological University of Miami data set shows a large scatter and low agreement for both, the Tegen et al. (2002) and the Balkanski et al. (2004) emission schemes. Generally, the predicted mass concentrations are underestimated, a fact that is particularly pronounced for low dust concentrations. Out of 244 measurements, only 24 (10 %) (Tegen et al., 2002) and 15 (6 %) (Balkanski et al., 2004) lie within a factor of 2 of the measurements. The better agreement of the annual peak concentrations for each station, highlighted in orange, indicates that the distinct dust events are better captured than the lower background concentrations responsible for a large part of the scatter. It has to be stressed that in a comparison of a one year simulation with a climatological dataset a not too good agreement can be expected. Further, as shown by Timmreck and Schulz (2004) based on a study with the ECHAM4 GCM and the Balkanski et al. (2004) emission scheme, the application of the nudging technique influences the wind statistics and spatial distribution, substantially reducing the dust emissions. Other potential explanations include: the neglect of the super-coarse mode emissions, a too low emission strength particularly of the Asian dust sources dominating a large part of the Pacific measurement sites, an overestimation of sink processes, possibly due to too efficient microphysical aging, as well as the influence of non-represented local sources on the dust measurements.

2.3.4 Number Distribution

The annual-mean zonal-mean aerosol number concentration (N) for the seven modes is shown in Figure 2.4. Nucleation is favoured in regions with little available aerosol surface area, low temperatures, and high relative humidity. Thus, the maxima of the nucleation mode number concentration can be found in the upper tropical troposphere and in the remote regions of the Antarctic where convective detrainment and DMS conversion, respectively, provide sufficient sulfuric acid. Note that a large part of the nucleation mode particles have radii below the typical detection limit of 3 nm of current measurement techniques. Number concentrations of the insoluble Aitken mode are determined by primary emissions of BC and POM and therefore highest in the lower troposphere close to the source regions of biomass burning and anthropogenic emissions. The soluble Aitken mode numbers are dominated by particles growing from the nucleation in the Aitken size-range. Accumulation and coarse insoluble modes are externally mixed dust modes and reflect the zonal distribution of the dust emissions, with the largest contribution from the North African dust sources around 25° N. Accumulation mode soluble numbers are highest in the lower troposphere between 30° S and 60° N close to the sources of biomass burning and fossil fuel use. Increased levels can also be found in the upper troposphere, attributable to convective detrainment of particles and their precursors. Coarse mode soluble particles are mainly confined to the lower troposphere and can mostly be attributed to sea salt emissions. Between 15° N and 20° N a local maximum due to the contribution of aged dust particles is identifiable around 800 hPa.

To evaluate the simulated aerosol number concentrations, we compare them in Figure 2.5 to vertical profiles obtained from aircraft measurements of the German Aerospace Agency (DLR). The measurements were conducted in the “Interhemispheric differences in cirrus properties from

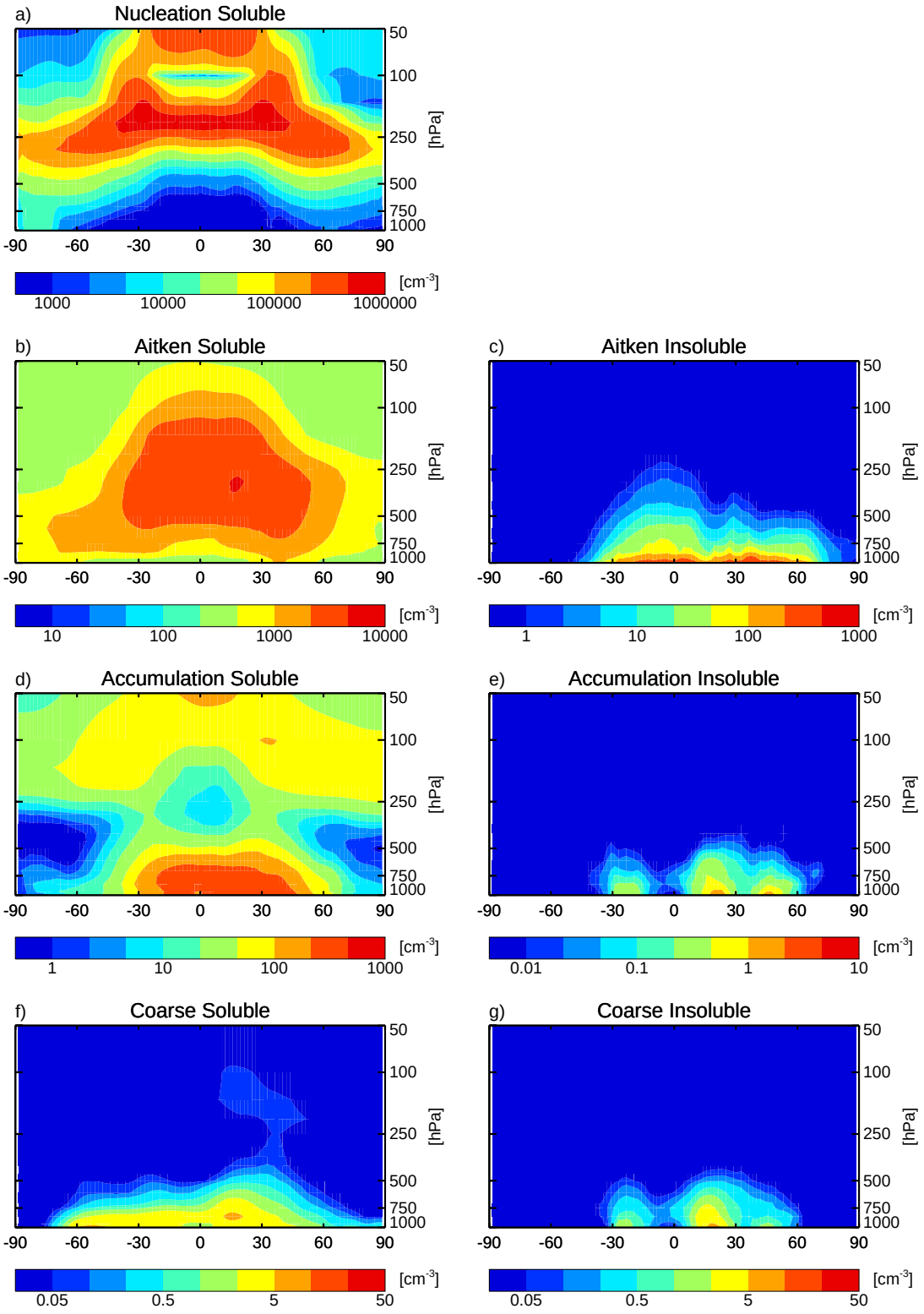

Figure 2.4: Annual-mean zonal-mean number concentration for each mode [cm^{-3} STP (1013.25 hPa, 273.15 K)].

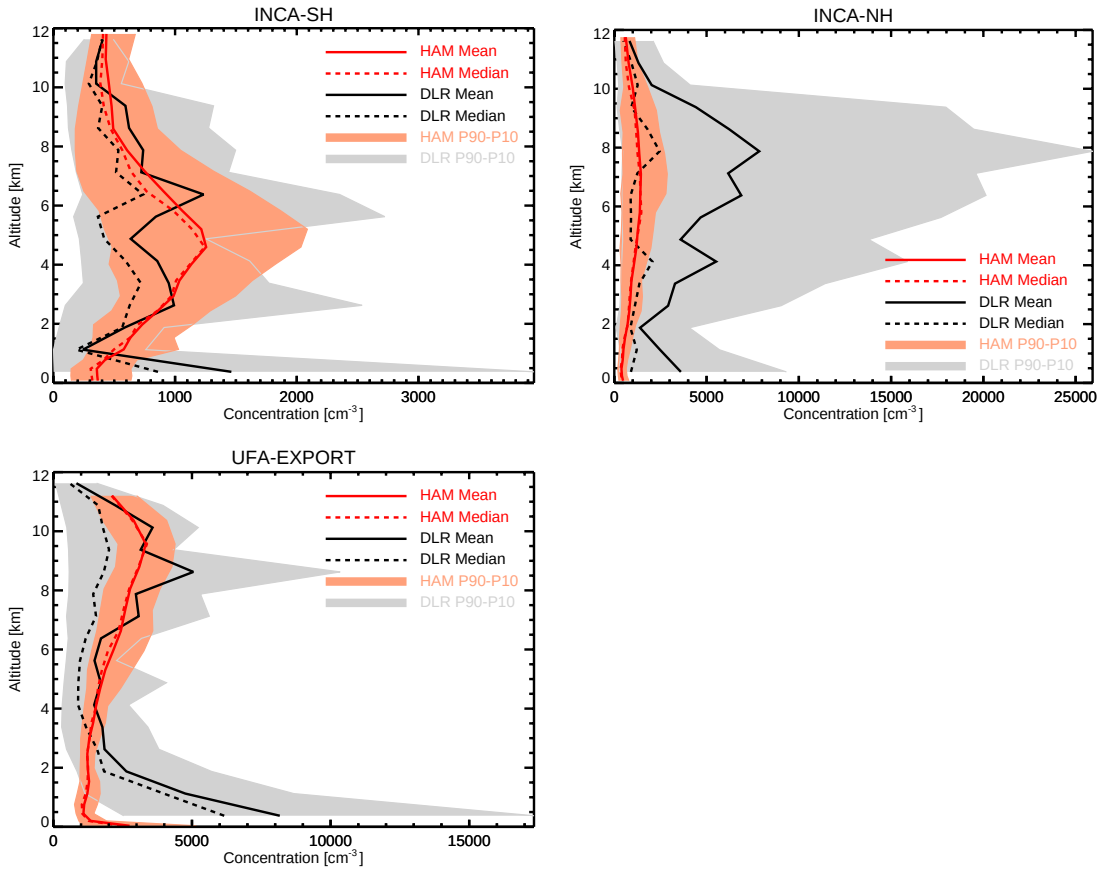

Figure 2.5: Composite profiles of aerosol number-concentration [cm^{-3} STP] from DLR aircraft measurements and ECHAM5-HAM for the INCA-SH, INCA-NH, and UFA-EXPORT measurement campaigns. ECHAM5-HAM results plotted in red, measurements in black, and the respective variability (P90-P10) in light red and gray.

anthropogenic emissions" (INCA) experiments (Minikin et al., 2003) and the UFA2/EXPORT campaign (Andreas Petzold and Andreas Minikin, *in preparation*). To avoid ambiguities in the comparison with individual flight data, we compare campaign mean and median profiles of the simulation with campaign mean and median profiles of the measurements. The model data is averaged over the grid boxes containing the measurement domain. The model aerosol numbers are the superposition of the individual modes of HAM folded with the cut-off of the measurement instruments.

The first INCA campaign was conducted in southern Chile (INCA-SH) from (23/03/2000 - 14/04/2000) in the domain (83.9°W - 69.1°W, 58.5°S - 51.0°S). The measured profile of aerosol numbers shows distinct maxima of median and mean in the mid-troposphere, between 2 and 7 km. ECHAM5-HAM well reproduces the vertical distribution of aerosol numbers. The underestimation in the lower boundary layer can be attributed to an underestimation of nucleation. The second INCA campaign was conducted in Scotland (INCA-NH) from (27/09/2000 - 12/10/2000) in the domain (8.7°W - 3.6°E, 54.6°N - 61.2°N). The median particle concentration shows a homogeneous distribution throughout the troposphere and is well captured by the ECHAM5-HAM simulation. The observations show a large variability between 2 and 10 km due to singular convective detrainment of polluted plumes (Andreas Minikin, *pers. comm.*). These events are not

reproduced in the simulation, leading to an underestimation of the model mean values in the free troposphere. Measurement over continental Europe were obtained during the UFA2/EXPORT campaign (19/07/2000 - 10/08/2000) in the domain (5.3°E - 28.8°E, 43.5°N - 56.7°N). The observed N shows a distinct maximum in the boundary layer, a mid tropospheric minimum around 5 km, and a second maximum between 7 and 11 km. The ECHAM5-HAM simulated profile of N is in good agreement with the observations throughout most of the troposphere. However, the aerosol numbers in the lower boundary layer are under-predicted. Possible explanations are an underestimation of nucleation, a too efficient growth into larger size regimes, a too large emission size-distribution, underestimation of the emissions, or overestimated surface sinks. It has to be pointed out that as no simultaneous measurements of aerosol mass are available, it is not possible to further isolate one of those causes.

The simulated variability of N, in terms of the difference of the 90^{th} percentile (P90) and the 10^{th} percentile (P10), for the polluted cases of UFA-EXPORT and INCA-NH is lower than in the measurements. In addition to the ambiguity of the comparison of grid-box mean values with local measurements, one explanation could be the usage of monthly mean emission data. The variability for the maritime southern hemispheric case INCA-SH, where interactively calculated natural emissions dominate, agrees well with the observations.

Simulated and measured dry aerosol number size-distributions are compared in Figure 2.6. Log-normally fitted median aerosol number size-distributions from a European surface measurements climatology for the period 1996 to 2001 (Putaud et al., 2003) have been averaged over the given morning and afternoon distributions as approximation of a daytime distribution. See Appendix B for a brief description of the measurement sites and Putaud et al. (2003) for a detailed description of the measurement compilation. The simulated size-distributions have been sampled at 12 UTC from the lowest model level grid-box containing the measurement location. Plotted are seasonal median and 10^{th} and 90^{th} percentiles size-distributions at standard atmospheric conditions for December-January-February (DJF) and June-July-August (JJA). It has to be stressed that the comparison of a model grid-box mean size-distribution with local surface measurements is compromised by scale differences that inevitably lead to non-negligible deviations. This becomes evident in the evaluation of the size-distributions at the Ispra and Milano measurement sites that lie within the same model grid-box. The large differences between the measured size distributions at these sites is indicative for the, in the model non-resolvable, sub-grid-scale variability.

Generally, the simulated size distributions broadly reproduce the observed characteristics ranging from highly polluted urban (Milano), to polluted near-city (Ispra and Melpitz), and more pristine rural (Hohenpeissenberg and Harwell) conditions. For the Ispra and Milano sites, the high winter accumulation mode number-concentrations are underestimated while in summer the accumulation mode is shifted to larger radii at which it is biased high. For Melpitz the simulated Aitken and accumulation mode numbers are well captured, however, nucleation mode numbers are underestimated in winter and summer. Similar deviations are also found in the comparison to the Hohenpeissenberg measurements, although the model captures part of the nucleation peak in wintertime conditions. For Harwell, the simulated aerosol numbers are significantly biased low beside the overestimation of wintertime nucleation. This can most likely be attributed to the fact that while the measurements are characteristic for local rural conditions, the model grid-box containing Harwell extends up to the coast and is not solely representable for the measurement conditions.

For all measurement sites, the nucleation mode number-concentrations are underestimated in summer. This could be indicative of an overestimation of the condensational sink, an under-

estimation of the nucleation rate, or the importance of other nucleation pathways than the simulated binary nucleation, such as ternary or ion-induced nucleation or the contribution of organic vapours.

2.3.5 Radiative Properties

Unlike the spatiotemporally constrained in-situ measurements, remote sensing data from satellites, supplemented by ground-based remote sensing, allows evaluating the model on a global scale. As the input parameters for the ECHAM5 radiation scheme are calculated by HAM explicitly in dependence of the size-distribution and composition of the modes, the resulting optical properties provide integrated information on the model performance. However, it should be kept in mind that remote sensing retrievals have uncertainties and maybe biased, in particular satellite retrievals of aerosol properties over land. Therefore, differences between model results and remote sensing products do not necessarily reflect model deficiencies.

The simulated field for the annual mean clear-sky aerosol optical depth (AOD) is displayed in Figure 2.7a. The regions with highest values of the simulated AOD are the Saharan dust plume extending into the Atlantic, biomass burning regions of Central Africa, and Asian regions with strong anthropogenic contributions, particularly regions over China and India. The simulated global annual mean optical depth at 0.14 falls in the range suggested by other global models (0.116 - 0.155) participating in the AEROCOM model inter-comparison (http://nansen.ipsl.jussieu.fr/AEROCOM/). The ECHAM5-HAM mean value is almost identical to a sampling bias corrected global average of AERONET (Kinne et al., *in preparation*) of 0.14. A similar corrected global annual average of the best available global data set, even so without coverage at high latitudes, a MODIS-MISR composite (see below), suggests a slightly larger value of about 0.16. This agreement is encouraging in light of the many retrieval uncertainties and the likelihood of AOD overestimates due to errors in cloud-screening. While, a good quantitative agreement to data on a global annual basis is encouraging, matches for distribution pattern on a regional and seasonal basis are a more meaningful test.

In comparisons to AOD simulations of Figure 2.7a, a measurement based AOD composite derived from advanced satellite retrievals is presented in Figure 2.7b. This data-set comprises a composite of monthly means based on satellite retrievals between March 2000 and February 2001. It combines the strength of different retrievals applied to multi-spectral data of the MODIS and MISR sensors on NASA's EOS TERRA platform: Over water, data of the MODIS ocean retrieval (Tanré et al., 1997) are used, while over land the multi-directional retrieval of MISR (Martonchik et al., 2002), when available, is preferred over the MODIS land retrieval (Kaufman et al., 1997). MODIS and MISR derived aerosol properties were validated against AERONET sun-photometer measurements. AOD retrieval errors are estimated at +/- 0.04 (at 10km scales) for the MODIS ocean retrieval (Remer et al., 2002) and at +/- 0.05 (at 50km scales) for the MISR land retrieval (Martonchik et al., 2004). The land retrieval of the MODIS sensor is similar uncertain at +/- 0.1 (at 10km scales) (Chu et al., 2002), often displays a significant positive bias, and fails over vegetation-poor surfaces, such as deserts. Thus, even though MISR data are approximately 5 times less frequently sampled than MODIS, the monthly statistics of the MISR land retrieval is preferred. When comparing results of this possibly best data-set to model-simulations, it should be kept in mind that the data presented in Figure 2.7b are associated with significant uncertainty, especially over land regions.

ECHAM5-HAM reproduces many patterns of the satellite composite. This includes large scale features, e.g. plumes from Asia into the Pacific or from Northern Africa into the Atlantic, as

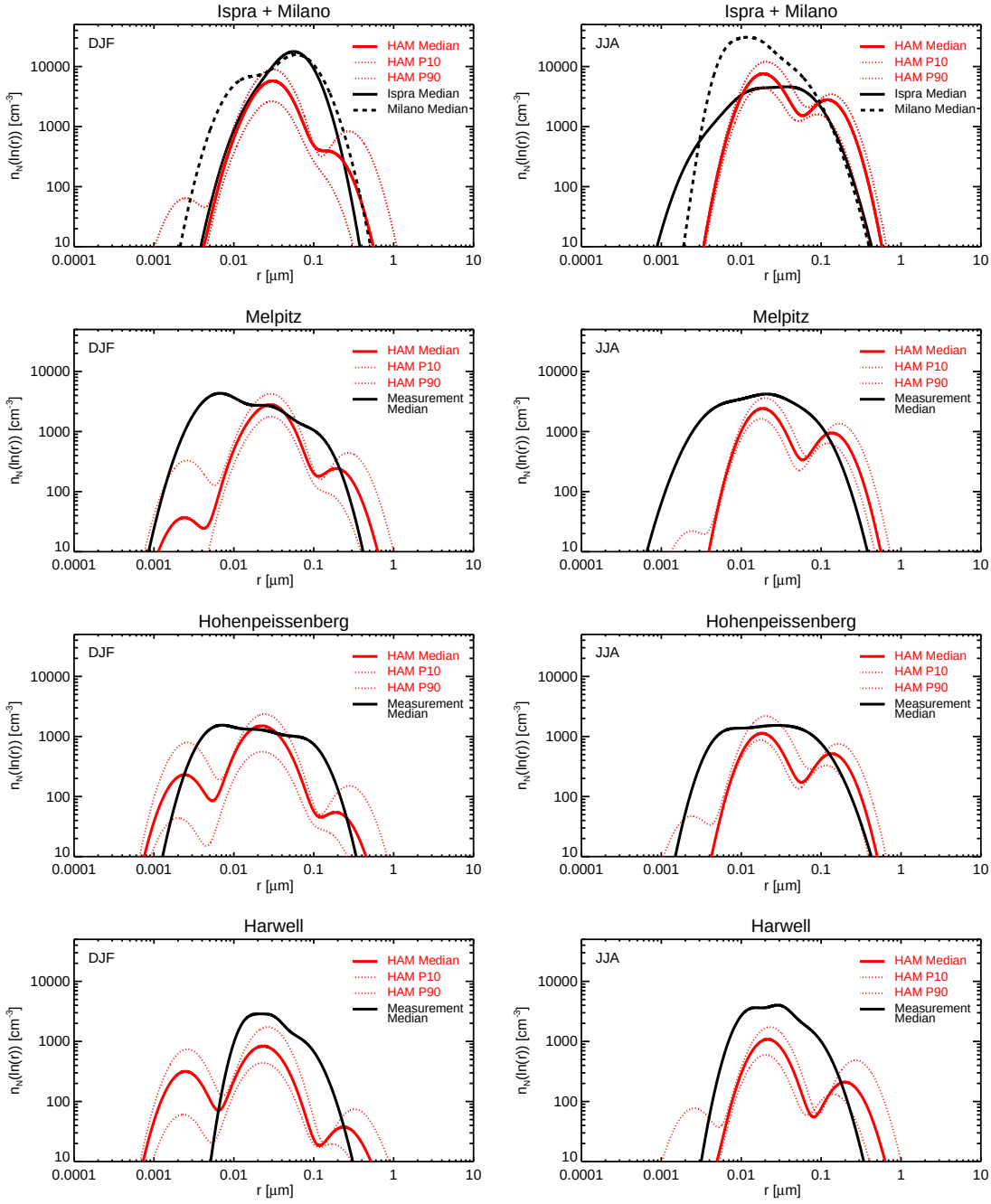

Figure 2.6: Seasonal-mean dry aerosol number size-distributions [cm^{-3} STP (1013.25 hPa, 273.15 K)] for December-January-February (DJF) and June-July-August (JJA) at the given locations. ECHAM5-HAM in red with medians as solid, and 10^{th} (P10) and 90^{th} (P90) percentiles as dotted line. Measurement medians (from Putaud et al., 2003) as black lines.

well as small scale features, e.g the east-west AOD gradients over North America and Europe or the tongue of low optical depth extending northward of the Himalaya region. In a quantitative sense, the ECHAM5-HAM AODs tend to be larger over oceans and smaller over land and at high latitudes. Higher AODs, attributable to sea salt, are most pronounced in the oceanic storm track regions and in the secondary tropical source regions centred around 15° N and S. Lower AODs over land are most prominently found from Northern Africa to the Middle East and in northern South America. Based on AERONET AOD statistics, the discrepancy in South America is attributed to retrieval error resulting in an AOD overestimate, which also contradicts the expected clean "green ocean" regime with low optical depths over Amazonia (Andreae et al., 2004). However, the discrepancy over North Africa and the Middle East is most likely caused by dust AOD underestimates of the model.
Simulated AOD discrepancies to measurements are better illustrated in seasonal and regional comparisons. In Figure 2.8 seasonal averaged AODs of ECHAM5-HAM are compared for 21 regions on a seasonal basis to four different measurement data-sets. AERONET (Holben et al., 2001), comprises (when present in selected regions) available (year 2000) AOD statistics of ground-based sun-photometry. MODIS-MISR represents the preferred satellite composite (3/2000 - 2/2001), which was already introduced in Figure 6. These two data-sets are more relevant to the model simulations, because they refer to the year 2000. The additional two data-sets are provided as (historical) reference because they represent decadal statistics on tropospheric AOD (two-year periods following the El Chichon and Mt.Pinatubo eruptions were removed). TOMS (Torres et al., 2002) is based on UV reflectance data between 1979 and 2001, while AVHRR (Mishchenko et al., 1999) is based on visible/near-IR reflectance data between 1983 and 2001. Due to an uncertain surface contribution to the visible reflection, AVHRR retrieval are only provided for ocean regions. All data in Figure 7 refer to the mid-visible reference wavelength $\lambda = 550$ nm.
Over oceans the MODIS retrieval is the best reference. The smallest pixel size helps support a better statistics and at the same time reduces the possibility of cloud contamination. Not surprisingly MODIS data display the lowest AOD values over oceans. ECHAM5-HAMs larger AOD for ocean regions in the tropics and during winter in the SH ocean regions suggests that sea salt AOD contributions are too large. Generally good AOD matches are found for off-source transport of dust and biomass over ocean regions, except for the North Pacific, where long-range transport from Asia is underestimated. Over land comparisons needs to take into account the larger uncertainty of the regional data, either related to accuracy issues of the satellite retrievals or related to a lack of regional representation for AERONET. For the land regions of the Americas and for Europe, AERONET is the preferred reference as there are sufficient stations in those regions. For all other regions the preferred reference is MISR. The at times large difference to the other land retrieval of TOMS, however, reduces confidence in the land retrievals. At large, there is a good agreement of simulated and retrieved regional AODs. For many regions, the simulated AODs lie within the range of the different retrievals. Focusing on the most pronounced differences, the ECHAM5-HAM model underestimates dust AOD in the North Africa-Middle East region. For the urban-industrial regions of the northern hemisphere the AOD contributions during fall and summer are often larger than the data. The biomass burning seasonal cycles in the (sub-) tropics are reproduced, although the strength of the biomass peak is underestimated, particularly in Southern Africa.
Satellite retrievals of the mid-visible Ångström parameter (ANG), defined as

$$\mathrm{ANG} = \frac{\ln \mathrm{AOD}_1 - \ln \mathrm{AOD}_2}{\ln \lambda_2 - \ln \lambda_1} \tag{2.21}$$

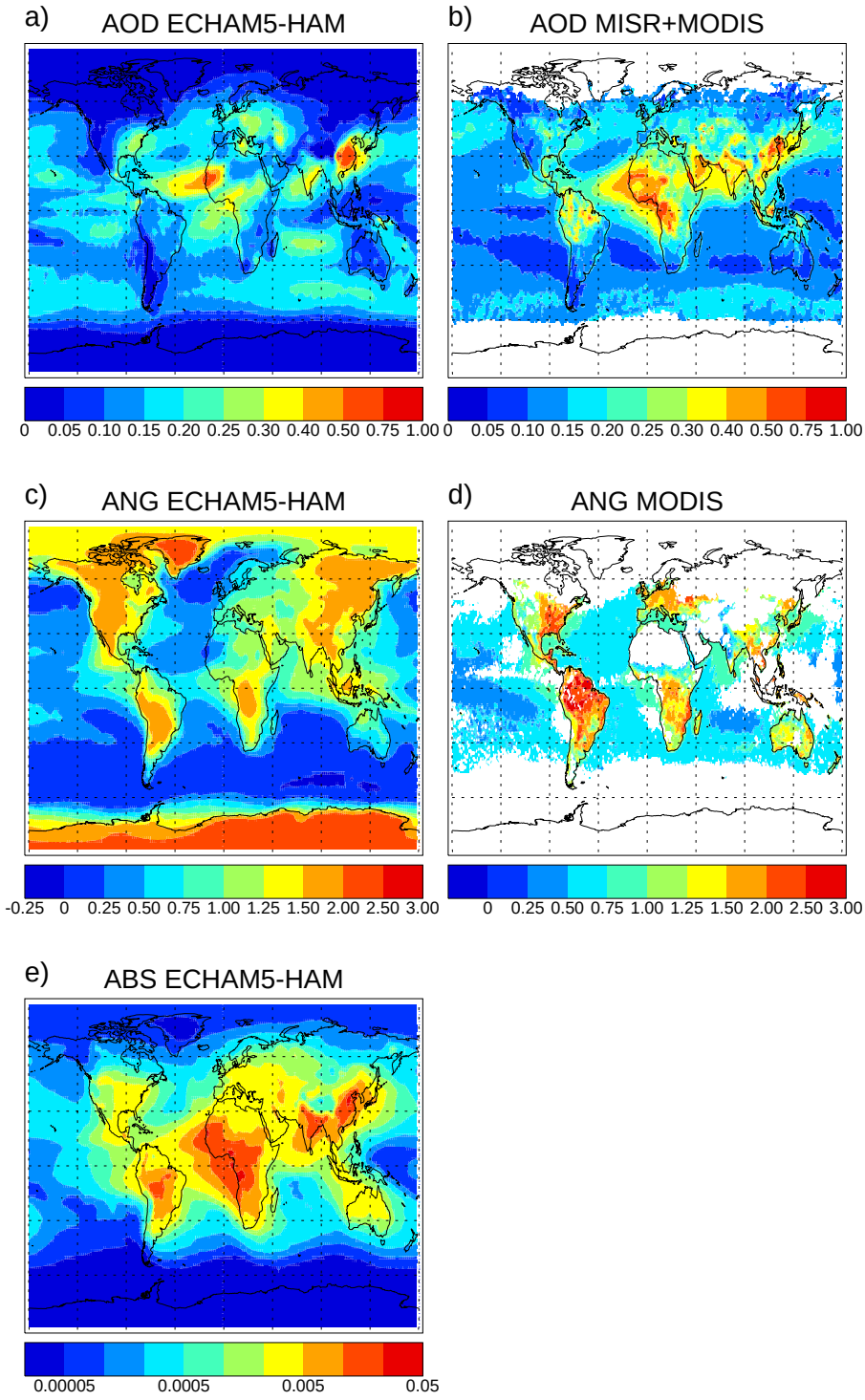

Figure 2.7: Annual mean aerosol optical depth AOD simulated with ECHAM5-HAM, satellite retrieved annual (3/2000-2/2001) mean aerosol optical depth based on a composite of monthly averages of the MODIS and MISR sensors (MODIS over oceans and MISR over land), simulated 550nm/825nm Ångström parameter ANG of ECHAM5-HAM, satellite retrieved ANG of MODIS (ocean: 550nm/865nm, land: 470nm/660nm), simulated absorption optical depth ABS of ECHAM5-HAM. ABS and AOD refer to a mid-visible wavelength $\lambda = 550$ nm.

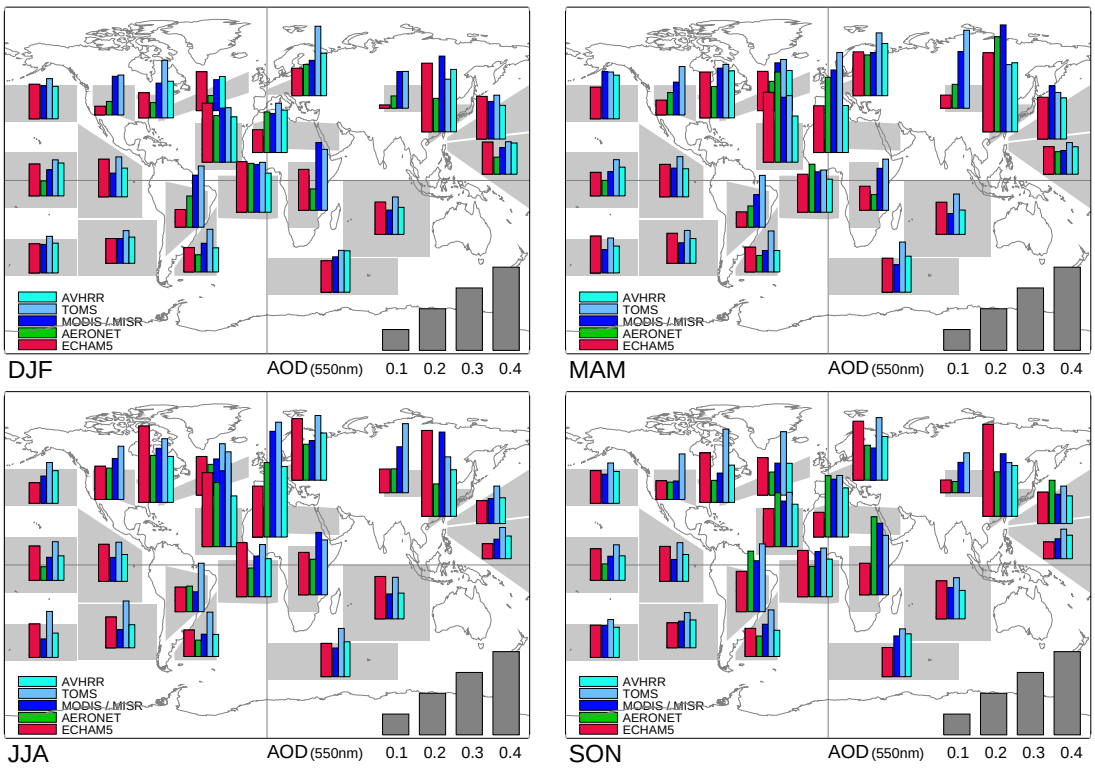

Figure 2.8: Seasonal-mean aerosol optical depths ($\lambda = 550$ nm) for December-January-February (DJF), March-April-May (MAM), June-July-August (JJA), and September-October-November (SON) for selected regions (gray) for the year 2000. ECHAM5-HAM (red), AERONET (green), composite of MODIS over water and MISR over land (dark blue), TOMS (light blue), and AVHRR (turquoise).

provide information on column integrated aerosol size. ANG values larger than 1.5 indicate that aerosol optical properties are dominated by the accumulation mode, whereas values smaller than 0.5 reflect a domination by coarse mode aerosol. Simulated ANG of ECHAM5-HAM are shown in Figure 2.7c and a composite of MODIS land retrievals (Kaufman et al., 1997) and MODIS ocean retrievals (Tanré et al., 1997) is shown in Figure 2.7d. Following the AOD accuracy assessment, MODIS ANG data over oceans are expected to be more accurate than over land. In addition, as MODIS AOD land retrievals largely ignore coarse size mode contributions, thus MODIS ANG values over land are often biased high. The ECHAM5-HAM simulation shows the expected land-sea contrast with higher ANG (smaller particles) over land and lower ANG (larger particles) over the oceans. While similar patterns and values for tropical oceans are matched by the model, there are also differences, particular over land regions at higher latitudes. Simulated higher ANG suggest smaller aerosol sizes over North America and Asia, although MODIS ANG could be biased low due to snow contamination. Over Europe smaller simulated ANG suggest larger aerosol sizes than indicated by data. Given the uncertainties in the MODIS ANG retrieval over land, however, it is not clear if these differences can be attributed to model deficiencies.

Aerosol absorption is an important parameter, as it determines the amount of solar heating by atmospheric aerosol, with potential implications to dynamics and the hydrological cycle. Aerosol absorption is commonly described by the aerosol absorption optical depth (ABS), which is defined by the product of the aerosol optical depth and the aerosol co-single-scattering albedo. Fig-

ure 2.7e displays the global distribution of the absorption optical depth simulated by ECHAM5-HAM. Highest values are found over the dust and biomass burning regions of Africa, the biomass burning regions of South America, and in the Asian regions with large anthropogenic activity, primarily regions in China and India. In the absence of global ABS measurements, we turned to aerosol absorption estimates from AERONET sky-radiation data inversion (Dubovik and King, 2000) for the year 2000. Monthly averages, which required a minimum of 10 inversions, were combined to seasonal averages. In Figure 2.9 these seasonal absorption averages are compared to ECHAM5-HAM simulations for two seasons (DJF and JJA) at selected AERONET sites (see Appendix C). It should be noted that the AERONET absorption (since derived from sky-radiance data) carries a significant uncertainty with likely overestimates at low aerosol optical depths. Thus, there should be a focus on cases of larger optical depths. Good agreement for absorption is found for the dust outflow off the west coast of Africa and for the strength and seasonality of North America and of the biomass burning regions in the southern hemisphere. Otherwise the simulated absorption tends to be smaller than AERONET. The deficits in the Mid-East can most likely be related to AOD underestimates in that region. The underestimation over Europe could be a consequence of potentially underestimated sources of black carbon, as discussed by Schaap et al. (2004), or due to the assumption of a smaller imaginary part of the refractive index for POM than suggested by recent estimates (Kirchstetter et al., 2004).

In summary, the ECHAM5-HAM simulation of aerosol optical depth, size-distribution in terms of the Ångström parameter, and absorption are in general agreement with remote sensing data from ground and space. While there is excellent AOD agreement for the global average, regional and seasonal analysis has shown that the ECHAM5-HAM overestimates sea salt contributions (particularly in the tropics and Southern oceans) and underestimates dust contributions (particularly in Northern Africa and the middle East). AODs in regions with strong anthropogenic contributions (particularly regions of Asia, Central to Eastern Europe, and the East Coast of North America) are generally well represented.

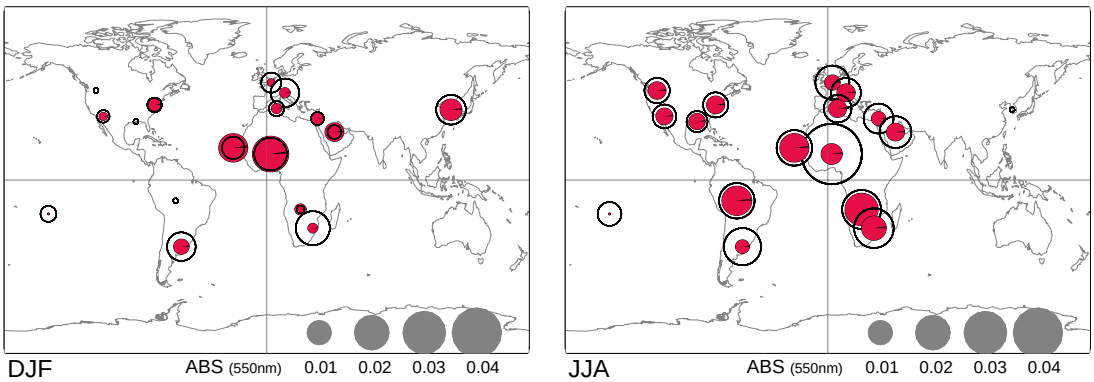

Figure 2.9: Seasonal-mean absorption aerosol optical depth ABS ($\lambda = 550$ nm) for December-January-February (DJF) and June-July-August (JJA) at selected AERONET sites. ECHAM5-HAM is displayed with filled red circles, AERONET with black circle lines. The absorption optical depth is proportional to the area of the circles.

2.4 Conclusions and Outlook

The aerosol-climate modelling system ECHAM5-HAM, as part of the emerging Max Planck Earth System Model, is introduced. Embedded in the ECHAM5 GCM, the aerosol model HAM predicts the evolution of an ensemble of microphysically interacting internally- and externally-mixed aerosol populations. In the current setup, the components sulfate, black carbon, particulate organic matter, sea salt, and mineral dust are included. Advancing from the bulk modelling approach of most previous global aerosol models, the aerosol size-distribution, mixing state, and composition are described by prognostic variables. This facilitates the explicit calculation of aerosol optical properties for the radiation calculation, an explicit treatment of the sink processes, and provides the necessary input for the aerosol-cloud coupling.

The aerosol model includes the processes gas- and liquid phase sulfur chemistry, the sink processes dry deposition, sedimentation, and wet deposition, a radiation module, and the microphysical core M7. M7 considers the processes coagulation, condensation on pre-existing aerosols, aerosol nucleation, thermodynamical equilibrium with water vapour, and the inter-modal transfer. The emissions of dust, sea salt and maritime DMS are calculated online. For all other compounds, emissions are based on an emission inventory for the year 2000, taking into account injection heights and emission size-distributions.

Despite the advanced complexity of ECHAM5-HAM, the computational efficiency allows the application in long-term climate studies.

Results of a one year nudged simulation for the year 2000 are presented. The global annual total emissions account to 95.2 Tg(S) yr^{-1} sulfuric compounds, 7.7 Tg yr^{-1} black carbon, 66.3 Tg yr^{-1} particulate organic matter, 5032 Tg yr^{-1} sea salt, as well as 662 Tg yr^{-1} and 787 Tg yr^{-1} dust for the Tegen et al. (2002) and Balkanski et al. (2004) emission schemes, respectively. Global annual-mean column burdens (lifetimes) of the compounds are: sulfate 0.80 Tg(S) (3.9 days), black carbon 0.11 Tg (5.4 days), particulate organic matter 0.99 Tg (5.4 days), sea salt 10.5 Tg (0.8 days), and dust 8.28 Tg (4.6 days). The compounds in the insoluble modes undergo microphysical aging, due to coagulation with soluble modes and sulfate coating, resulting in aging times of 0.7 days for BC, 1.1 days for POM, and 4.8 days for DU.

The global sulfate column burden shows a pronounced export from Europe to northern Africa and the Middle East. Substantial exports of pollutants from Europe towards the Mediterranean and northern Africa have also been observed in the MINOS measurement campaign (Lelieveld et al., 2002). The distinct long-range transport of sulfate can most likely be attributed to lower dry deposition velocities for SO_2 and sulfate over bare soils along the transport pathway. In contrast, most earlier studies assumed fixed dry deposition velocities over land surfaces. A large dust plume extending from North Africa into the Atlantic is the dominant feature of the dust distribution, secondary features are enhanced burdens over central Asia and Australia. Black carbon and particulate organic matter show large burdens in the vicinity of the biomass burning regions of Central Africa and South America, as well as in the regions with large anthropogenic activity, primarily near China and India. The dominant emissions of sea salt lie in the oceanic storm track regions. Compared to these emissions, the sea salt burden is high in the secondary source regions, centred around 15° N and S. Two factors account for this distribution as they result in high sinks coinciding with the source regions: First, the wet deposition is highest in the precipitation rich storm track regions. Second, the interactive calculation of the dry deposition velocities results in higher values in the oceanic storm tracks.

The evaluation of the simulated surface mass concentrations with measurements from the North American IMPROVE network, the European EMEP network, the Global Atmosphere Watch

program, and a climatological compilation for remote sites by the University of Miami shows generally a good agreement, except for dust. The simulated sulfate mass agrees well with a slight tendency to overestimate, in particular over Europe. As the sink processes are treated globally uniform, the good agreement in North America and the overestimation over Europe could potentially indicate a positive bias of the European emissions. For BC the agreement is good with no discernible bias. Also for POM there is a good agreement, however, with low concentrations the simulated concentrations are increasingly underestimated. SS surface mass concentrations agree well at marine measurement sites. Low concentrations at continental sites are overestimated in the model, most likely due to numerical diffusion associated with the strong sea-land gradients. For dust, the comparison with the climatological dataset of the University of Miami reveals a general underestimation of surface mass concentrations for both, the Tegen et al. (2002) and Balkanski et al. (2004) emission schemes. Focusing only on the peak aerosol masses at stations with significant dust concentrations, the agreement is somewhat better. An analysis of the seasonality of the dust surface concentrations (not shown) reveals generally a good agreement. It has to be stressed that the inhomogeneous distribution of the measurement stations (12 out of 21 used stations lie in the Pacific and only 3 in the outflow region of the dominant North African dust sources) bias the scatter plots towards sites where the radiative impacts of dust are low or negligible. As the underestimation is particularly pronounced at remote sites (see Table 2.9) the neglect of the super-coarse mode, with a short lifetime, appears not to be the main cause of the bias. This leaves a too low emission strength, in particular of the Asian dust sources, or an overestimation of the wet deposition as the most likely causes. The wet deposition is highly sensitive to two assumptions: First, the microphysical aging time depends on the required amount of sulfate to assume particles as coated. The current choice of a mono-layer of sulfate needs to be scrutinised in laboratory studies. Second, the scavenging parameters R are subject of large uncertainties. Even though measurements for individual cloud events are available, the translation to different aerosol types, to the grid-box scale and finally to the global scale, is highly uncertain. Further sensitivity studies will be carried out to investigate the sensitivity to the different assumptions.

Total simulated aerosol numbers are dominated by secondary particle formation. Highest number concentrations are found in the upper troposphere. Primary emissions dominate the accumulation and coarse mode sizes, largely confined to the low to mid troposphere. Simulated number concentrations are evaluated with campaign composite aircraft measurement data from three year 2000 measurement campaigns. For the maritime influenced southern hemispheric INCA-SH and northern hemispheric INCA-NH campaigns, the simulation nicely reproduces the vertical profiles of the median number concentration with maxima in the mid troposphere. For the continental UFA/EXPORT campaign, the number concentrations in the boundary layer are underestimated, however, the low values in the mid troposphere and the maximum between 7 and 12 km are in good agreement with the observations.

Simulated aerosol number size-distributions broadly reproduce the observed characteristics for a range of evaluated conditions from European surface measurement sites. Nonetheless, non-negligible deviations are found. Most of these differences are not attributable to specific processes as they could also be attributed to sub-grid scale variability and uncertainties in the local-scale emissions. However, a persistent feature at all sites is the underestimation of simulated nucleation mode number concentrations in summer. This could be indicative of an overestimation of the condensational sink but could also be explained by the importance of other nucleation pathways than the simulated binary sulfate / water nucleation.

The predominant features of the simulated aerosol optical depth are the Saharan dust plume

extending into the Atlantic, outflow regions of Central African biomass burning, Asian regions with strong anthropogenic pollution, and oceanic regions attributable to the contribution of sea salt aerosol. The simulated global average of aerosol optical depth is with 0.14 in very good agreement with estimates from remote sensing products (AERONET derived global average: 0.14, MODIS-MISR composite: 0.16) and falls within the range of estimates of other modelling studies (0.116 - 0.155) participating in the AEROCOM inter-comparison. The comparison of the AOD with remote sensing products on the regional scale reveals that the contribution by dust is underestimated, particularly in North-Eastern Africa, the Middle East, and East Asia extending into the Pacific outflow region. This is also the cause of an underestimation of absorption during the dust season, compared to Middle East AERONET measurements. Further it is consistent with the negative bias of the surface mass concentrations. The remote oceanic AODs are generally higher than the remote sensing data, suggesting an overestimation of the sea salt aerosol optical depth. This could either be a consequence of overestimated sea salt burdens, of an overestimated water uptake, or of a mismatch of the ambient size-distribution, resulting in a too high extinction cross section. However, the fact that the evaluation of the sea salt water uptake calculated by M7 with a more complex thermodynamical model revealed an overestimation at relative humidities between 45 % and 75 % (Vignati et al., 2004), suggests this bias as an important contribution to the overestimation. The underestimation of AODs at high latitudes of North America and Asia, together with the relatively good agreement of the surface mass concentrations of the in this regions predominant POM, could potentially indicate the effect of the neglect of water uptake by carbonaceous aerosols.

The presented results are part of an ongoing long-term research activity in which the ECHAM5-HAM aerosol climate model and the underlying parameterisations are further evaluated with increasing availability of suitable observational data.

The microphysical approach of ECHAM5-HAM, minimising the number of externally imposed parameters, is a major achievement. For example, most previous parameterisations used in indirect aerosol effect studies (see Penner et al. (2001)) rely on empirical relations that might not be applicable for different climatic regimes. The extension of the prognostic parameter space in ECHAM5-HAM to include size distribution, composition, mixing state provides the basis for a microphysical coupling of the aerosol and cloud schemes. ECHAM5-HAM has already been extended by an advanced cloud microphysical scheme with explicit treatment of cloud droplet number concentration and ice crystal number concentration (Lohmann et al., 1999a; Lohmann and Kärcher, 2002). This setup provides the fundament for future studies of the semi-direct and indirect aerosol radiative effects. The explicit treatment of the aerosol activation will also allow to reduce the uncertainty associated with the scavenging parameters and render the investigation of aerosol-cloud interaction in a GCM possible. However, the explicit treatment of aerosol-cloud interactions, in particular considering the ice phase, is a long-term effort that requires the development and improvement of suitable parameterisations. A sound experimental basis is required to be established in future laboratory and in-situ measurement studies.

Optionally, instead of the reduced sulfur chemistry scheme implemented in HAM, the full MOZART chemistry scheme (Horowitz et al., 2003) is available in ECHAM5, allowing for studies of heterogeneous chemistry and aerosol-chemistry interactions. In the framework of the EU project PHOENICS (http://phoenics.chemistry.uoc.gr), an extended thermodynamical module (Metzger et al., 2002) is being coupled with M7 in ECHAM5 and will be merged into the ECHAM5-HAM model. This development will, together with the MOZART chemistry scheme, establish the basis for the inclusion of the currently neglected nitrate/ammonium system and considerably improve the accuracy of the water uptake calculations. Also within PHOENICS, a

condensed version of a comprehensive secondary organic aerosol model (Tsigaridis and Kanakidou, 2003), computationally efficient for long-term simulations, is in development.

Acknowledgements

We wish to thank Joe Prospero and Dennis Savoie (University of Miami) for providing the compilation of multi-annual surface observations and to Brent Holben (NASA Goddard) for the use of the AERONET data. Many thanks also to Rita van Dingenen (JRC, Ispra) for helping us with the size-distribution measurements and to Sarah Guilbert (LSCE, Gif-sur-Yvette) for her help with the handling of the IMPROVE, EMEP, and GAW datasets. We are also grateful to Martin Schultz (MPI for Meteorology, Hamburg) for providing the MOZART chemistry fields. Frank Dentener (JRC, Ispra) is to be thanked for his support with the emission data and many helpful discussions. Our thanks extend to our colleagues (MPI for Meteorology, Hamburg) Luis Kornblueh, Sebastian Rast, Andreas Rhodin, Erich Roeckner, and Uwe Schulzweida for their constant support with the ECHAM5-HAM model development, and to Rene Hommel and Claudia Timmreck for fruitful discussions about the aerosol module and the help with the nucleation parameterisation. Ulrich Koerner (DKRZ, Hamburg) is to be thanked for the support with the code optimisation. We would also like to acknowledge the support of the German DEKLIM project, of the International Max Planck Research School for Earth System Modelling, and of the EU project PHOENICS (EVK2-CT-2001-00098).

2.5 Appendix A: List of Surface Measurement Stations Used in Figure 2.3

Sulfate

Location	Longitude	Latitude	Model Annual Mean [μg m^{-3}]	Measurement Annual Mean [μg m^{-3}]	Model Standard Deviation	Measurement Standard Deviation	Total Number Measurements
EMEP Network							
Aliartos	23.1	38.4	6.1	2.8	3.09	1.19	100
Anholt	11.5	56.7	3.7	2.5	3.36	1.49	355
Aspvretren	17.4	58.8	1.2	0.7	1.18	0.96	91
Birkenes	8.2	58.4	1.9	1.3	2.35	1.31	364
Danki	37.8	54.9	6.8	1.7	5.44	1.33	326
DiablaGora	22.1	54.2	5.4	2.4	4.51	2.05	354
Eskdalemuir	-3.2	55.3	2.1	1.3	2.04	1.08	344
HighMuffles	-0.8	54.3	3.1	1.8	2.58	1.32	358
Jarczew	22.0	51.3	7.6	4.7	5.24	2.31	360
Keldsnor	10.7	54.7	3.9	3.0	3.04	1.69	360
Kolummerwaard	6.3	53.3	3.9	1.9	3.19	1.28	316
Kpuszta	19.5	50.0	8.3	5.0	5.59	3.13	349
Leba	17.5	54.8	5.3	3.7	4.25	2.18	366
Montelibretti	12.6	42.1	5.3	3.2	4.27	1.71	345
Neuglobsow	13.0	53.2	4.8	3.2	4.61	2.45	338
Oulanka	29.4	66.3	1.3	1.2	1.72	0.97	364
Preila	21.2	55.3	4.7	2.8	4.30	1.82	360
Roervik	11.9	57.4	3.2	2.2	2.98	2.19	361
Rucava	21.2	56.2	4.2	0.8	3.60	0.83	366
Shepeljovo	29.1	60.0	4.2	0.4	2.92	0.34	345
Skrealaden	6.7	58.8	1.5	1.1	2.32	1.20	343
Tange	9.6	56.3	3.2	2.4	2.92	1.43	327
Uto	21.4	59.8	3.4	1.8	2.78	1.30	366
Vavihill	13.1	56.0	3.8	2.3	3.63	1.84	361
Vreedepeel	5.8	51.5	4.1	2.3	2.91	1.66	334
IMPROVE Network							
Acadia	-68.3	44.4	2.4	1.6	2.12	1.35	97
Badlands	-101.9	43.7	2.2	1.0	1.74	0.63	89
Bandelier	-106.3	35.8	2.4	0.8	1.60	0.39	103
Big Bend	-103.2	29.3	3.2	2.1	2.22	1.28	83
Boundary Waters	-91.5	48.0	1.1	1.0	1.46	0.66	61
Denali	-149.0	63.7	0.2	0.3	0.18	0.26	77
Everglades	-80.7	25.4	1.7	2.7	1.52	2.63	56
Gila Wilderness	-108.2	33.2	2.2	0.9	1.60	0.48	66
Mammoth Cave	-86.3	37.3	6.5	4.8	4.42	3.34	99
Mount Rainier	-122.1	46.8	1.8	0.8	1.44	0.69	103
Okefenokee	-82.1	30.7	4.2	3.9	2.81	2.34	95
Virgin Island	-64.8	18.3	0.6	1.1	0.44	0.41	38
University of Miami Network							
Chatham Island - New Zealand	-176.5	-43.9	0.4	0.3			
Cape Point - South Africa	18.5	-34.3	1.5	0.6			
Cape Grim - Tasmania	144.7	-40.7	0.6	0.3			
Invercargill - New Zealand	168.4	-46.4	0.3	0.4			
Marsh - King George Island	-58.3	-62.2	0.4	0.3			
Marion Island	37.8	-46.9	0.3	0.1			
Mawson - Antarctica	62.5	-67.6	0.1	0.1			
Palmer Station - Antarctica	-64.1	-64.8	0.3	0.1			
Reunion Island	55.8	-21.2	0.3	0.4			
Wellington - New Zealand	174.9	-41.3	0.5	0.4			
Yate - New Caledonia	167.0	-22.1	0.5	0.4			
Funafuti - Tuvalu	-179.2	-8.5	0.4	0.2			
Nauru	166.9	-0.5	0.6	0.2			
Norfolk Island	168.0	-29.1	0.3	0.3			
Rarotonga - Cook Islands	-159.8	-21.2	0.2	0.1			
American Samoa	-170.6	-14.2	0.2	0.3			
Midway Island	-177.4	28.2	0.3	0.5			
Oahu Hawaii	-157.7	21.3	0.4	0.5			
Cheju - Korea	126.5	33.5	7.8	7.2			
Hedo Okinawa - Japan	128.2	26.9	5.1	4.3			
Fanning Island	-159.3	3.9	0.4	0.6			
Enewetak Atoll	162.3	11.3	0.3	0.1			
Barbados	-59.4	13.2	0.4	0.7			
Izana Tenerife	-16.5	28.3	1.6	1.0			
Bermuda	-64.9	32.3	1.1	2.1			
Heimaey Iceland	-20.3	63.4	0.4	0.7			
Mace Head - Ireland	-9.9	53.3	1.4	1.3			
Miami	-80.2	25.8	2.0	2.2			
GAW Network							
Hohenpeissenberg	11.0	47.8	3.4	1.6	2.65	0.98	224

Table 2.6: List of sulfate measurement sites used in Figure 2.3 and corresponding statistics.

Black Carbon

Location	Longitude	Latitude	Model Annual Mean [μg m^{-3}]	Measurement Annual Mean [μg m^{-3}]	Model Standard Deviation	Measurement Standard Deviation	Total Number Measurements
IMPROVE Network							
Acadia	-68.3	44.4	0.2	0.2	0.18	0.16	99
Badlands	-101.9	43.7	0.2	0.2	0.10	0.15	90
Bandelier	-106.3	35.8	0.2	0.3	0.07	0.69	104
Big Bend	-103.2	29.3	0.1	0.2	0.06	0.11	83
Boundary Waters	-91.5	48.0	0.1	0.2	0.16	0.17	61
Denali	-149.0	63.7	0.0	0.1	0.02	0.17	104
Everglades	-80.7	25.4	0.1	0.3	0.06	0.21	56
Gila Wilderness	-108.2	33.2	0.2	0.3	0.05	0.55	66
Mammoth Cave	-86.3	37.3	0.5	0.5	0.22	0.28	99
Mount Rainier	-122.1	46.8	0.6	0.3	0.48	0.22	104
Okefenokee	-82.1	30.7	0.2	0.5	0.13	0.51	97
Virgin Island	-64.8	18.3	0.0	0.0	0.01	0.05	38

Table 2.7: List of black carbon measurement sites used in Figure 2.3 and corresponding statistics.

Organic Matter

Location	Longitude	Latitude	Model Annual Mean [μg m^{-3}]	Measurement Annual Mean [μg m^{-3}]	Model Standard Deviation	Measurement Standard Deviation	Total Number Measurements
IMPROVE Network							
Acadia	-68.3	44.4	0.9	0.9	1.04	0.50	99
Badlands	-101.9	43.7	0.8	1.1	1.04	1.15	90
Bandelier	-106.3	35.8	0.9	1.4	0.74	4.44	104
Big Bend	-103.2	29.3	0.9	1.0	0.65	0.72	83
Boundary Waters	-91.5	48.0	0.7	1.0	0.86	0.77	61
Denali	-149.0	63.7	0.2	0.7	0.23	2.46	104
Everglades	-80.7	25.4	0.5	1.0	0.40	0.57	56
Gila Wilderness	-108.2	33.2	0.8	2.0	0.53	3.10	66
Mammoth Cave	-86.3	37.3	2.1	2.3	1.57	1.77	99
Mount Rainier	-122.1	46.8	1.7	1.2	1.47	0.89	104
Okefenokee	-82.1	30.7	2.3	2.5	1.50	2.56	97
Virgin Island	-64.8	18.3	0.0	0.4	0.05	0.17	38

Table 2.8: List of organic matter measurement sites used in Figure 2.3 and corresponding statistics.

Dust

Location	Longitude	Latitude [μg m^{-3}]	Model Annual Mean [μg m^{-3}]	Measurement Annual Mean
University of Miami Network				
Cape Point - South Africa	18.5	-34.3	0.49	2.20
Marsh - King George Island	-58.3	-62.2	0.0006	0.52
Mawson - Antarctica	62.5	-67.6	0.0002	0.10
Palmer Station - Antarctica	-64.1	-64.8	0.0002	0.35
Yate - New Caledonia	167.0	-22.1	1.09	0.17
Funafuti - Tuvalu	-179.2	-8.5	0.01	0.19
Nauru	166.9	-0.5	0.01	0.10
Norfolk Island	168.0	-29.1	1.21	0.84
Rarotonga - Cook Islands	-159.8	-21.2	0.04	0.11
American Samoa	-170.6	-14.2	0.01	0.16
Midway Island	-177.4	28.2	0.04	0.72
Oahu Hawaii	-157.7	21.3	0.01	0.66
Cheju - Korea	126.5	33.5	3.16	14.14
Hedo Okinawa - Japan	128.2	26.9	1.46	8.37
Fanning Island	-159.3	3.9	0.01	0.10
Enewetak Atoll	162.3	11.3	0.01	0.24
Barbados	-59.4	13.2	6.89	14.48
Izana Tenerife	-16.5	28.3	22.12	30.18
Bermuda	-64.9	32.3	0.61	3.36
Mace Head - Ireland	-9.9	53.3	0.37	1.00
Miami	-80.2	25.8	1.25	4.59

Table 2.9: List of dust measurements sites used in Figure 2.3 and corresponding statistics.

Sea Salt

Location	Longitude	Latitude	Model Annual Mean [μg m^{-3}]	Measurement Annual Mean [μg m^{-3}]	Model Standard Deviation	Measurement Standard Deviation	Total Number Measurements
IMPROVE Network							
Acadia	-68.3	44.4	6.5	0.6	6.60	0.93	99
Badlands	-101.9	43.7	0.2	0.0	0.23	0.07	88
Bandelier	-106.3	35.8	0.3	0.0	0.34	0.05	97
Big Bend	-103.2	29.3	1.7	0.2	1.79	0.38	81
Boundary Waters	-91.5	48.0	1.0	0.1	1.03	0.16	61
Denali	-149.0	63.7	0.5	0.1	1.24	0.17	104
Everglades	-80.7	25.4	10.1	1.0	10.06	0.80	56
Gila Wilderness	-108.2	33.2	0.8	0.1	1.09	0.12	57
Mammoth Cave	-86.3	37.3	0.8	0.2	1.45	0.35	99
Mount Rainier	-122.1	46.8	2.7	0.2	3.89	0.26	105
Okefenokee	-82.1	30.7	4.8	0.7	4.55	0.75	100
Virgin Island	-64.8	18.3	13.9	1.7	7.43	1.23	38
University of Miami Network							
Chatham Island - New Zealand	-176.5	-43.9	27.3	13.8			
Cape Point - South Africa	18.5	-34.3	18.3	10.4			
Cape Grim - Tasmania	144.7	-40.7	22.6	19.8			
Invercargill - New Zealand	168.4	-46.4	20.9	7.1			
Marsh - King George Island	-58.3	-62.2	18.1	3.5			
Marion Island	37.8	-46.9	45.6	10.5			
Mawson - Antarctica	62.5	-67.6	0.8	0.3			
Palmer Station - Antarctica	-64.1	-64.8	9.1	3.2			
Reunion Island	55.8	-21.2	23.2	11.6			
Wellington - New Zealand	174.9	-41.3	15.7	10.4			
Yate - New Caledonia	167.0	-22.1	18.0	31.9			
Norfolk Island	168.0	-29.1	19.0	26.0			
American Samoa	-170.6	-14.2	9.5	5.5			
Midway Island	-177.4	28.2	17.7	14.3			
Oahu Hawaii	-157.7	21.3	21.1	14.9			
Cheju - Korea	126.5	33.5	11.5	16.4			
Hedo Okinawa - Japan	128.2	26.9	15.4	23.3			
Fanning Island	-159.3	3.9	17.7	14.8			
Barbados	-59.4	13.2	21.5	17.4			
Izana Tenerife	-16.5	28.3	20.1	0.0			
Bermuda	-64.9	32.3	16.0	13.4			
Heimaey Iceland	-20.3	63.4	14.3	25.7			
Mace Head - Ireland	-9.9	53.3	18.4	19.8			
Miami	-80.2	25.8	10.6	8.5			
GAW Network							
Hohenpeissenberg	11.0	47.8	1.5	0.4	3.53	0.56	224

Table 2.10: List of sea salt measurement sites used in Figure 2.3 and corresponding statistics.

2.6 Appendix B: List of Surface Measurement Sites Used in Figure 2.6

Location	Longitude	Latitude	Altitude [m a.s.l.]	Category
Milano-Bresso (I)	45.53	9.20	130	Urban
Ispra (I)	45.82	8.63	209	Near-City
Melpitz (D)	51.53	12.93	86	Near-City
Hohenpeissenberg (D)	47.80	11.02	988	Rural
Harwell (GB)	51.57	-1.32	125	Rural

Table 2.11: List of surface measurement sites used in Figure 2.6.

2.7 Appendix C: List of AERONET Measurement Sites Used in Figure 2.9

Location	Longitude	Latitude
AERONET Network		
Abracos Hill	-62.4	-10.8
Anmyon	126.3	36.5
Banizombou	2.7	13.5
Cap Verde	-22.9	16.7
Ceilap	-58.5	-34.6
El Arenosillo	6.7	37.1
Goddard	-106.1	53.9
Lille	3.1	50.6
Maricopa	-112.0	33.1
Mongu	-15.3	23.2
Nes Ziona	34.8	31.9
Rimrock	-117.0	46.5
Skukusa	31.6	-25.0
Solar Village	46.4	24.9
Stennis	-89.6	30.4
Tahiti	-149.6	-17.6
Venice	12.5	45.3

Table 2.12: List of AERONET measurement stations used in Figure 2.9.

Chapter 3

Emission-Induced Nonlinearities in the Global Aerosol System · Results From the ECHAM5-HAM Aerosol-Climate Model[1]

Abstract

In a series of simulations with the global ECHAM5-HAM aerosol-climate model, we analyze the response to changes in anthropogenic emissions. Traditionally, additivity is assumed in the assessment of the aerosol climate impact as the underlying bulk aerosol models are largely constrained to linearity. The microphysical aerosol module HAM establishes degrees of freedom for non-linear responses of the aerosol system. In our results, aerosol column mass burdens respond non-linearly to changes in anthropogenic emissions, manifested in alterations of the aerosol life-times. Specific emission changes induce modifications of aerosol cycles with unaltered emissions, indicating a microphysical coupling of the aerosol cycles. Anthropogenic carbonaceous emissions disproportionately contribute to the accumulation mode numbers close to the source regions. In contrast, anthropogenic sulfuric emissions less than proportionally contribute to the accumulation mode numbers close to the sources regions and disproportionately contribute in remote regions. We analyze the additivity of the aerosol system by comparing the changes from a simulation with emission changes for several compounds with the sum of changes of single simulations in each of which one the emission changes was introduced. Close to the anthropogenic source regions, deviations from additivity are found at up to 30 % and 15 % for the accumulation mode number burden and aerosol optical thickness, respectively. Our results challenge the traditional approach of assessing the climate impact of aerosols separately for each component and demand for integrated assessments and emission strategies.

3.1 Introduction

Atmospheric aerosol, defined as a suspension in air of liquid or solid particles, plays an important role in the global climate system. Aerosol particles modify the global radiation budget directly, by scattering and absorption (Ångström, 1962; McCormic and Ludwig, 1967), as well

[1]Submitted to *Journal of Climate*, with J., Feichter, S. Kloster, E. Vignati, J. Wilson as co-authors.

as indirectly, by the modification of cloud properties. An increase of aerosols acting as cloud condensation nuclei (CCN) yields in higher cloud droplet number concentrations (CDNC) with smaller radii, increasing the cloud albedo (Twomey, 1974, 1977), referred to as first indirect effect. Higher CDNC also can potentially decrease the precipitation efficiency resulting in a longer cloud lifetime and an subsequent increase of the planetary albedo (Albrecht, 1989), referred to as second indirect effect. In contrast, absorbing aerosols heat the atmosphere potentially evaporating cloud droplets (Graßl, 1975; Hansen et al., 1997), decreasing the planetary albedo, referred to as semi-direct effect. Suitable aerosols, when acting as ice-nuclei, can enhance the precipitation formation in mixed phase clouds (Lohmann, 2002), decreasing the cloud lifetime and therefore the planetary albedo. Modulation of solar radiation by aerosol scattering and absorption affects the surface heat radiation and therefore the hydrological cycle (Roderick and Farquhar, 2002; Liepert et al., 2004; Feichter et al., 2004). Furthermore, heterogeneous reactions on the aerosol surface and in liquid aerosol particles interact with the chemistry of the atmosphere (Crutzen, 1996; Ravishankara, 1997; Andreae and Crutzen, 1997; Emmons et al., 2003) affecting the radiative effects of chemical species. Additionally, the deposition of aerosols in the ocean plays an important role in the biogeochemical cycle of the oceans (Johnson et al., 1997; Vink and Measures, 2001) with potential feedbacks to the climate system via the emissions of aerosol precursors such as dimethyl sulfide (DMS) (Charlson et al., 1987).

Nevertheless, the quantitative evaluation of these aerosol effects is still insufficient (e.g. Penner et al. (2001); Ramanathan et al. (2001)). One reason for this is the inherent complexity of the global aerosol system. Aerosols and their precursors originate from all compartments of the earth system. A large number of aerosol compounds are observed, covering a wide range of compositions and mixing states as well as orders of magnitude in size (e.g. Murphy et al. (1998); Bates et al. (1998); Seinfeld et al. (2004)). The other main reason for the insufficient understanding of the global aerosol system is that the short life-time of aerosols causes large spatio-temporal inhomogeneities. Thus, in-situ observations provide the most detailed insight into the aerosol system, but are representative of limited spatial and temporal scales. Remote sensing data from ground-based lidar and sun-photometers provide valuable information but suffer from sampling limitations as well. Up to now, operational remote sensing data from space only provide integral aerosol properties and retrievals rely on a-priori information about the aerosol system and internal aerosol models.

Global aerosol models can help to increase the understanding about the complex aerosol system for past, present, and future conditions. Furthermore, they permit to identify the effects of specific aerosol components and aerosol sources on the climate system.

The first global aerosol models simulated the distribution of the mass of one of the major aerosol components: sulfate (SU), black (elemental) carbon (BC), particulate organic matter (POM), sea salt (SS), and mineral dust (DU). Langner and Rhode (1991), Feichter et al. (1996), and Rasch et al. (2000) simulated the global sulfur cycle. A range of studies (e.g. Cooke and Wilson (1996); Liousse et al. (1996); Cooke et al. (1999)) simulated the distribution of carbonaceous aerosols. The mineral dust cycle has been investigated e.g. in Tegen and Lacis (1997), Ginoux et al. (2001) and the sea salt distribution e.g. in Guelle et al. (2001). Consecutively, global aerosol models incorporated more aerosol components as external mixtures (Haywood et al., 1997b; Lohmann et al., 1999a; Chin et al., 2002). However, in order to derive the aerosol radiative effects and also for the parameterization of the sink processes, information on the aerosol composition, mixing-state, and size-distribution is essential. The size-distribution of single aerosol components has been investigated, e.g. in Tegen and Lacis (1997) predicting the evolution of externally mixed dust size-classes with size-dependent sources and sinks. The complexity of the processes and

computational constraints caused a bifurcation in the model development. On the one hand models with advanced chemistry and thermodynamics evolved, e.g. Nenes et al. (1998), with a focus on the chemical composition. On the other hand microphysical models developed with a focus on the prediction of the size distribution and with less detail on the aerosol composition. Higher-resolution sectional aerosol models provide a detailed description of the aerosol size-distribution. Adams and Seinfeld (2002) simulate the size-distribution of sulfate aerosol with a 30-bin sectional microphysical aerosol model. However, also the aerosol mixing-state affects the microphysical, chemical and radiative properties of aerosols and therefore their cycling and climatic effects. The computational burden of multicomponent sectional aerosol models with size-resolved description of the mixing state is with current computational resources too demanding for long-term transient climate simulations of the global aerosol system. Up to now, only few global aerosol models suitable for long-term integrations simulate the size-distribution and mixing state of interacting multicomponent aerosols. The application of computationally efficient modal aerosol microphysical schemes maintains the balance in complexity between the numerous processes in general circulation models and provides the basis for long-term simulations. Wilson et al. (2001) represent the size-distribution in a multicomponent aerosol model by a superposition of eight partly interacting log-normal modes. Ghan et al. (2001a,b) use an interactive modal size-segregated multicomponent module to estimate the direct and indirect radiative aerosol forcing. In Stier et al. (2004) we introduced the aerosol module HAM of the Max Planck Institute - Earth System Model (MPI-ESM). In HAM the aerosol distribution is represented by an ensemble of interacting internally and externally-mixed log-normal aerosol modes. The sink processes as well as the aerosol optical properties are calculated in dependence of size and composition.

As it is now widely accepted that aerosols exert a distinct impact on regional and global scale climate (Penner et al., 2001; Heintzenberg et al., 2003) and that enhanced aerosol concentrations pose a risk to human health (Dockery et al., 1993; Lippmann, 2000), emission reduction strategies for aerosols and their precursors become of fundamental importance. Earlier, acidification-related aerosol precursors were mitigated. Particulate mass has now become a criteria pollutant (e.g. EC (1999); WHO (2003)). It is widely assumed that the responses of the aerosol system are linear, so that the changes in the emissions are linearly reflected in the aerosol distribution. However, changes in emissions of aerosols or their precursors can potentially induce non-linear responses of the global aerosol system. Observations indicate that the mixing state of the global aerosol system shows a large internally mixed contribution with varying ratios among constituents (e.g. Murphy et al. (1998); Bates et al. (1998); Seinfeld et al. (2004)). Thus, one can hypothesize that changes in the emissions of individual aerosol compounds or their precursors can affect the chemical and microphysical aging capacity of the atmosphere, resulting in a non-linear response of aerosol populations with a coherence among the individual aerosol compounds. Chemical aging in this context refers to the modification of aerosol properties via heterogeneous reaction on the aerosol surface or chemical reactions within the aerosol particles. Microphysical aging refers to growth and modification of aerosols by coagulation with other aerosol particles, condensation of gaseous compounds on the aerosol surface, and by cloud processing, affecting their size-distribution, solubility, and radiative properties. For secondary aerosols, emission changes can also induce shifts in chemical equilibria and modify the oxidizing capacity of the atmosphere, non-linearly affecting the aerosol system (e.g. Chin et al. (2000)). Shifts in the relative emission strength of the aerosol compounds can affect the phase partitioning of semi-volatile aerosol species resulting in non-linear responses of the aerosol mass (West et al., 1999). Spatially inhomogeneous emissions changes can introduce non-linearities in the mass response

as the aerosol sink processes and resulting lifetime vary regionally and, in particular for the secondary particles, by source type and formation pathway (Graf et al., 1997). Additionally, as highlighted in Wilson et al. (2001), one can expect that the response of the aerosol numbers will be non-linear, even when the response of the aerosol mass is linear, as secondary particle formation, growth and sink processes are highly non-linear functions of the aerosol and aerosol-precursor mass.
The representation of these processes in global aerosol models is a challenging task. The majority of current global aerosol models, bulk mass models without prognostic treatment of size-distribution and mixing state, can only capture non-linearities due to spatially inhomogeneous emissions and due to shifts in chemical equilibria. Some bulk models parameterize aging time-dependently, neglecting spatial and temporal variations in the aging capacity, e.g. due to anthropogenic pollution. Thermodynamical models can additionally account for the non-linear partitioning effects. Global microphysical aerosol models are required to scrutinize the effect of variations of emissions on the aerosol aging and cycling, the aerosol size-distribution and numbers, as well as on the coherence among the aerosol cycles. The microphysical approach of HAM, including the processes coagulation, condensation, nucleation, sulfur-chemistry, water uptake, as well as size and composition dependent sink processes for the ensemble of log-normal modes allows to investigate the listed non-linearities, except for the phase partitioning effect.
In this study we analyze the response of the global aerosol system to changes in anthropogenic emissions of aerosols and their precursors with a particular focus on non-linearities and the coherence among the aerosol cycles.
Section 3.2 describes the ECHAM5-HAM aerosol-climate model as part of the MPI-ESM and the investigated emission scenarios. The analysis of the response of the aerosol system to anthropogenic emission changes is presented in Section 3.3. Section 3.4 concludes the main findings.

3.2 Model Description

3.2.1 The aerosol-climate model ECHAM5-HAM

In the current setup, the MPI-ESM consists of the following interactively coupled sub-models: the atmospheric general circulation model ECHAM5 (Roeckner et al., 2003, 2005), the ocean general circulation model MPI-OM (Marsland et al., 2003), the surface and vegetation model JSBACH (Schnitzler et al., 2005), the atmospheric aerosol model HAM (Stier et al., 2004), the atmospheric chemistry model MOZECH (Schultz et al., in preparation), and the ocean biogeochemistry model HAMOCC (Maier-Reimer et al., 2005). In this study we use a sub-model of the MPI-ESM, the combined ECHAM5-HAM aerosol-climate model, described in detail in Stier et al. (2004).

The ECHAM5 General Circulation Model The atmospheric general circulation model ECHAM5 is the fifth-generation climate model developed at the Max Planck Institute for Meteorology, evolving from the model of the European Centre for Medium-Range Weather Forecasts (ECMWF). ECHAM5 solves prognostic equations for vorticity, divergence, surface pressure and temperature expressed in terms of spherical harmonics with a triangular truncation. Non-linear processes and the physical parameterizations are solved on a corresponding Gaussian grid. Water vapor, cloud liquid water, cloud ice and trace components are transported in grid-point space with a flux form semi-Lagrangian transport scheme (Lin and Rood, 1996). ECHAM5 contains a new microphysical cloud scheme (Lohmann and Roeckner, 1996) with prognostic equations for

cloud liquid water and ice. Cloud cover is predicted with a prognostic-statistical scheme solving equations for the distribution moments of total water (Tompkins, 2002). Convective clouds and convective transport are based on the mass-flux scheme of Tiedtke (1989) with modifications by Nordeng (1994). The solar radiation scheme (Fouquart and Bonnel, 1980) has 4 spectral bands, 1 for the visible and ultra-violet, and 3 for the near-infrared. The long-wave radiation scheme (Mlawer et al., 1997; Morcrette et al., 1998) has 16 spectral bands. ECHAM5 has the capability to perform nudged simulations, i.e. to relaxate the prognostic variables towards an atmospheric reference state, such as forecast or re-analysis data from operational weather forecast models.

The Aerosol Module HAM The microphysical aerosol module HAM (Stier et al., 2004) predicts the evolution of an ensemble of seven interacting internally- and externally-mixed log-normal aerosol modes. In the current setup, the components sulfate, black carbon, particulate organic matter, sea salt, and mineral dust are included. The aerosol mixing state is prognosed within the possible mixing-state configurations illustrated in Table 3.1. The modes are composed either of compounds with no or low solubility, henceforth denoted as insoluble mode, or by an internal mixture of insoluble and soluble compounds, henceforth denoted as soluble mode. The main components of HAM are the microphysical core M7 (Vignati et al., 2004), an emission module, a sulfur chemistry scheme (Feichter et al., 1996), a deposition module, and a module to calculate the aerosol radiative properties.

Modes	**Soluble / Mixed**	**Insoluble**
Nucleation	N_1, M_1^{SU}	
Aitken	N_2, M_2^{SU}, M_2^{BC}, M_2^{POM}	N_5, M_5^{BC}, M_5^{POM}
Accumulation	N_3, M_3^{SU}, M_3^{BC}, M_3^{POM}, M_3^{SS}, M_3^{DU}	N_6, M_6^{DU}
Coarse	N_4, M_4^{SU}, M_4^{BC}, M_4^{POM}, M_4^{SS}, M_4^{DU}	N_7, M_7^{DU}

Table 3.1: Modal structure and possible mixing state configurations of HAM. N_i denotes the aerosol number of the mode i and M_i^j denotes the mass of compound $j \in \{SU, BC, POM, SS, DU\}$ in mode i.

The microphysical core M7 calculates the coagulation among the modes, the condensation of gas-phase sulfuric acid on the aerosol surface, the binary nucleation of sulfate, and the water uptake. Emissions of dimethyl sulfide (DMS) are calculated interactively from prescribed DMS seawater concentrations (Kettle and Andreae, 2000). Dust emissions are calculated following Tegen et al. (2002) and sea-salt emissions after Schulz et al. (*in preparation*). The emissions of anthropogenic and volcanic SO_2, of terrestrial DMS, of BC and of POM are based on the AEROCOM aerosol model inter-comparison experiment (http://nansen.ipsl.jussieu.fr/AEROCOM/) emission inventories (Dentener et al., *in preparation*) for the years 1750 and 2000. Initially, dust and black carbon emissions are assumed insoluble and 65 % of the POM emissions are assumed soluble. The soluble fraction of POM is assumed to condense on the soluble modes, the insoluble fraction is emitted in particulate form in the insoluble Aitken mode. For the conversion of the carbon mass of POM into the total mass of POM, a factor of 1.4 is applied. The sink processes dry deposition, sedimentation, and wet deposition as well as the aerosol optical properties are parameterized in dependence of size and composition. For the wet deposition, the differentiation of the soluble and insoluble modes is introduced in form of mode-specific semi-empirical scavenging parameters with reduced scavenging efficiencies for the insoluble modes (c.f. Stier

et al. (2004)).
This setup allows the prediction of the aerosol composition, size-distribution and mixing state. As these properties in turn affect the interactively calculated sink processes and optical properties, it renders the investigation of microphysical interaction effects on the global aerosol system possible.

3.2.2 Scenarios

To investigate the microphysical coupling among the aerosol cycles and the role of specific aerosol contributors we perform a series of simulations in which we switch off the emission of the respective aerosol contributor and compare the results to a reference run with the complete emission scenario. In the simulations the large-scale meteorology is constrained to the year 2000 by nudging ECHAM5 to the ECMWF ERA40 reanalysis data (Simmons and Gibson, 2000). The nudging method permits local-scale meteorological processes, such as clouds, to respond to perturbations (Jeuken et al., 1996). We use a resolution of horizontally T63 in spectral space with a corresponding resolution of $1.8° \times 1.8°$ on a Gaussian grid. The vertical resolution is set to 31 levels, extending from the surface up to 10 hPa.
To isolate the effects of the different aerosol sources we perform simulations with the full year 2000 emissions (REF) as evaluated in Stier et al. (2004), with solely natural emissions (NAT), and with pre-industrial emissions for the year 1750 (PI). Additionally, we perform year 2000 simulations without SO_2 emissions from fossil-fuel use, industry and bio-fuels (NAS), without BC and POM emissions from fossil-fuel use and industry (NAC), and a combined simulation without SO_2 emissions from fossil-fuel use, industry and bio-fuels and without BC and POM emissions from fossil-fuel use and industry (NA). For the NAT scenario the assumption is made that emissions from vegetation fires, fossil-fuel use, industry and bio-fuels have solely anthropogenic origin. Thus these emissions are not included in NAT. As a non-negligible fraction of vegetation fires are of natural origin, ignited by lightning (Saarnak, 2001), this scenario is a lower estimate of the natural emissions. An overview of the scenarios is given in Table 3.2, the respective emission strengths are listed in Table 3.3, and the zonal emission distribution is depicted in Fig. 3.1. It should be noted that the interactively calculated sources of DMS, sea salt, and dust are unaltered in the scenarios but show marginal variability due to variations in the local meteorological parameters, as only the large scale meteorology is constrained by the nudging technique. While in the REF scenario, following the recommendations of AEROCOM, 2.5 % of the total SO_2 emissions are assumed to be in form of primary sulfate, we emit in the NPS scenario 100 % of the SO_2 emissions as SO_2. To isolate the impact of the changes in aerosol emissions, for all runs the offline oxidant fields for the sulfate chemistry are used as in the REF scenario.

3.3 Results

3.3.1 Response of Aerosol Mass

If the response of the aerosol system were linear and decoupled, a decrease of the emission strength of a certain species should result in a reduction of the total aerosol burden of that species by the same percentage. Therefore, the lifetime of a species, defined as the ratio of the mass burden [Tg] to sources [Tg $days^{-1}$], should be unaffected. Distribution, burden and lifetime of other species should not be altered. Table 3.4 lists the annual-mean total sources, the

REF	Reference with year 2000 emissions
NAS	Reference without: anthropogenic sulfuric emissions from fossil-fuel use, industry and bio-fuels
NAC	Reference without: anthropogenic carbonaceous emissions from fossil-fuel use and industry
NA	Combination of NAS and NAC Reference without: anthropogenic sulfuric emissions from fossil-fuel use, industry and bio-fuels anthropogenic carbonaceous emissions from fossil-fuel use and industry
NAT	Solely natural emissions
PI	Pre-Industrial emissions for year 1750
NPS	Reference without: SO_2 emissions assumed in form of primary sulfate

Table 3.2: Emission scenarios used for the simulations.

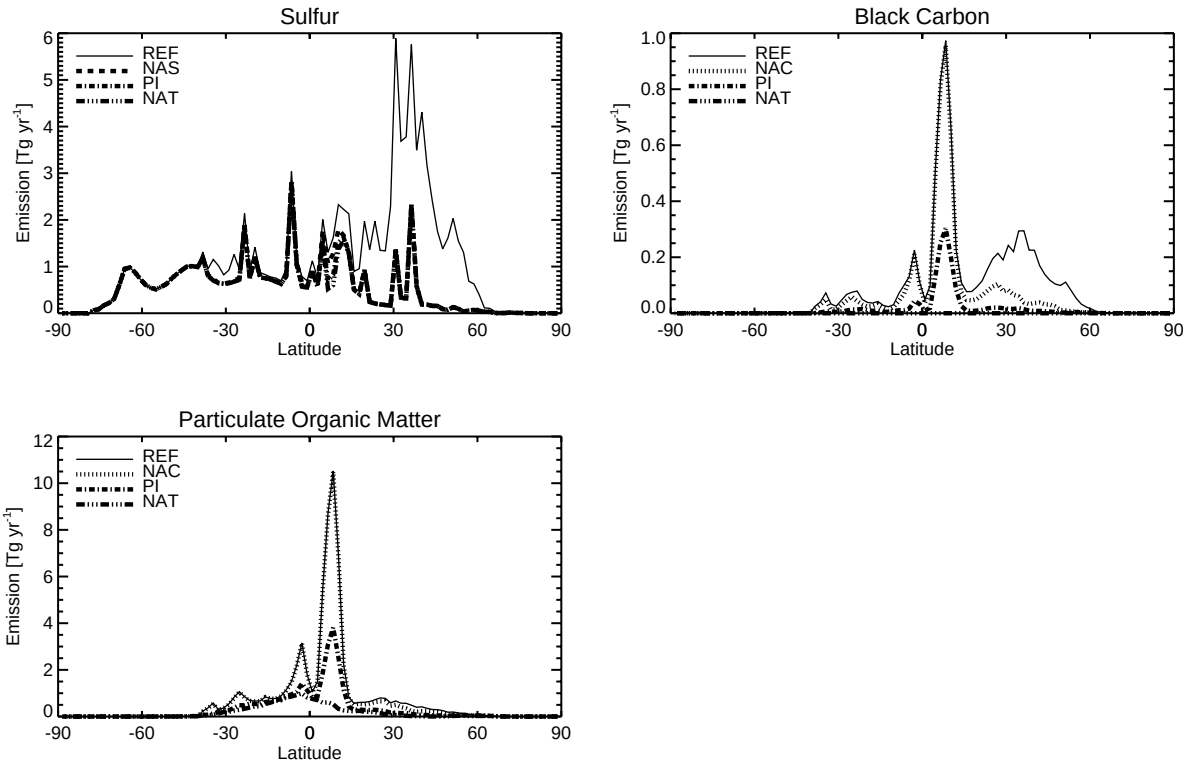

Figure 3.1: Annual zonal-mean aerosol and aerosol precursor emissions [Tg yr^{-1}] for the reference scenario (REF), the natural (NAT), the pre-industrial (PI), the scenario without SO_2 emissions (NAS) and without BC and POM emissions (NAC) from fossil-fuel and industry.

Species	Source	REF	NAT	PI	NAS	NAC	NA
DMS	Marine Biosphere	23.1	23.2	23.2	23.1	23.2	23.1
	Terrestrial Biosphere	0.3	0.3	0.3	0.3	0.3	0.3
SO_2	Volcanoes	14.3	14.3	14.3	14.3	14.3	14.3
	Vegetation Fires	2.1	-	0.7	2.1	2.1	2.1
	Fossil-Fuel, Industry and Bio-Fuels	54.2	-	0.1	-	54.2	-
Total sulfur		94.0	37.8	38.6	39.8	94.1	39.8
BC	Vegetation Fires	3.0	-	1.0	3.0	3.0	3.0
	Fossil-Fuel and Industry	3.0	-	-	3.0	-	-
	Bio-Fuels	1.7	-	0.4	1.7	1.7	1.7
Total BC		7.7	-	1.4	7.7	4.7	4.7
POM	Biogenic	19.1	19.1	19.1	19.1	19.1	19.1
	Vegetation Fires	34.7	-	12.7	34.7	34.7	34.7
	Fossil-Fuel and Industry	3.4	-	-	3.4	-	-
	Bio-Fuels	9.1	-	2.2	9.1	9.1	9.1
Total POM		66.3	19.1	34.0	66.3	62.9	62.9
DU [$\times 10^{-1}$]	Wind driven						
Accumulation		0.8	0.8	0.8	0.8	0.8	0.8
Coarse		65.4	66.4	66.1	65.4	65.7	65.7
Total DU		66.2	67.2	66.9	66.2	66.5	66.5
SS [$\times 10^{-2}$]	Wind driven						
Accumulation		0.5	0.5	0.5	0.5	0.5	0.5
Coarse		49.6	49.7	49.7	49.5	49.6	49.6
Total SS		50.1	50.2	50.2	50.0	50.1	50.1

Table 3.3: Global annual aerosol and aerosol-precursor emissions in [Tg yr^{-1}] for sulfuric species for the reference (REF), the natural (NAT), the pre-industrial (PI), the scenario without SO_2 emissions (NAS) and without BC and POM emissions (NAC) from fossil-fuel and industry, respectively. Units of sulfate refer to [Tg(S)], emissions of dust and sea salt are scaled with 10^{-1} and 10^{-2}, respectively.

column burden, and the lifetime for the different scenarios and aerosol species. For sulfate the sources are the sum of SO_2 in-cloud oxidation, condensation of gas-phase sulfuric acid, primary emissions, and nucleation. For the initially insoluble DU and BC and for the initially insoluble fraction of POM the microphysical aging time is given, defined as ratio of the column burden [Tg] of the insoluble compound divided by the transfer to the soluble modes [Tg $days^{-1}$]. The zonal distribution of the column burdens and the percent changes with respect to the REF scenario are depicted in Fig. 3.2.

From Table 3.4 it is evident that the sea salt cycle is unaffected by the changes in anthropogenic emissions as anthropogenic components that become attached by microphysical processes are negligible in terms of aerosol mass and sea salt is a priori soluble. Therefore, the sea salt cycle is not further investigated.

For the other compounds, alterations in the aerosol lifetime are evident, indicating a non-linear response of the aerosol mass to changes in the emissions. In all scenarios except NAC, the sulfate sources were approximately halved. The sulfate life-time increases from 3.8 days in REF to 4.2 and 4.3 days for the NAT and the PI, NAS, NA scenarios, respectively. It is not possible to attribute the non-linearity solely to microphysical aging as the increase of life-time is also

consistent with the relative shift of the emissions to low-latitude source regions (Fig. 3.1) and to natural sources, facilitating a longer life-time (Graf et al., 1997).
However, the increase of the burden and life-time of BC in the scenario without anthropogenic sulfur emissions (NAS) is a clear evidence for the impact of microphysical aging and the coherence of the aerosol cycles. The reduction of the sulfate source from 76.1 Tg(S) yr^{-1} in REF to 34.6 Tg(S) yr^{-1} in NAS increases the global life-time of BC from 5.4 days to 5.8 days as the reduced microphysical aging slows down the transfers of BC to the soluble modes making it less prone to wet deposition. For POM the increase from 5.5 days to 5.6 days is less pronounced as 65% of the POM sources are already assumed soluble. The effect of aging is also reflected in the increase of the aging times of BC, POM, and DU by 164 %, 84 %, and 66 %, respectively. The zonal distribution of the column burden shows a general increase in BC, with the most pronounced absolute increase between 15°N and 40°N where the reduction in sulfuric emissions is strongest. For POM the change in the annual zonal-mean column burden is similar though less pronounced. For BC, POM, and DU the zonal distribution shows the strongest relative increase in the high northern latitudes reaching 70 %, 20 %, and 20 % respectively. These increases are accompanied by total deposition rates increases of up to 140 %, 60 %, and 20 %, respectively (*not shown*).
In the scenario without carbon emissions from fossil fuels and industry (NAC), the reduction of the total aerosol mass source is with 6.4 Tg yr^{-1} relatively small and does not significantly affect the mass burden of other aerosol cycles. However, the BC life-time increases from 5.4 days to 6.4 days. This is most likely attributable to the shift of the dominant emission source to biomass burning with maxima of the vegetation fire emissions in the dry season and injection of the emissions above the surface sinks. The aging-time of BC and POM is slightly decreased as the insoluble BC and POM in the NAC scenario are predominantly co-emitted with the soluble POM in the biomass burning regions.
Conversely, the POM lifetime in the NAT and PI scenarios is decreased from 5.5 days to 4.0 and to 4.9 days, respectively, as the relative contribution of emissions from non biomass-burning sources increases. The minimum zonal-mean relative reduction of BC and POM is found around 60°N. For POM in the PI scenario the increase due to reduced microphysical aging out-weights the decrease due to the reduced emissions, resulting in an absolute increase of POM of up to 40 %.
Life-time and burden of the natural dust cycle are less sensitive to changes in anthropogenic emissions. Global annual-mean dust burdens increase by 3.4 %, 2.9 %, and 1.5 % for the NAT, PI, and NAS scenario, respectively. However, the zonal distribution of the burden changes for the NAS, NAT, and PI scenarios indicates that the zonal mean dust burden in remote areas is enhanced by up to 20 % and also the life-time is slightly enhanced. Regionally, the increase in dust burden exceeds 40 % for the NAT scenario (*not shown*). The increased aging time is consistent with a decrease in microphysical aging.
In summary, the response of aerosol mass to anthropogenic emission changes shows significant non-linearities manifested as changes in the aerosol life-time. The induced changes in the annual zonal-mean mass burdens are type and source specific. A clear coherence among the aerosol cycles, caused by microphysical coupling, is evident.

3.3.2 Response of Aerosol Numbers

In the preceding paragraph we showed that the mass response of the global aerosol system to changes in emissions shows significant non-linearities and that there is a microphysical coupling of the aerosol cycles. As aerosol mass and numbers are interdependent, a non-linear response

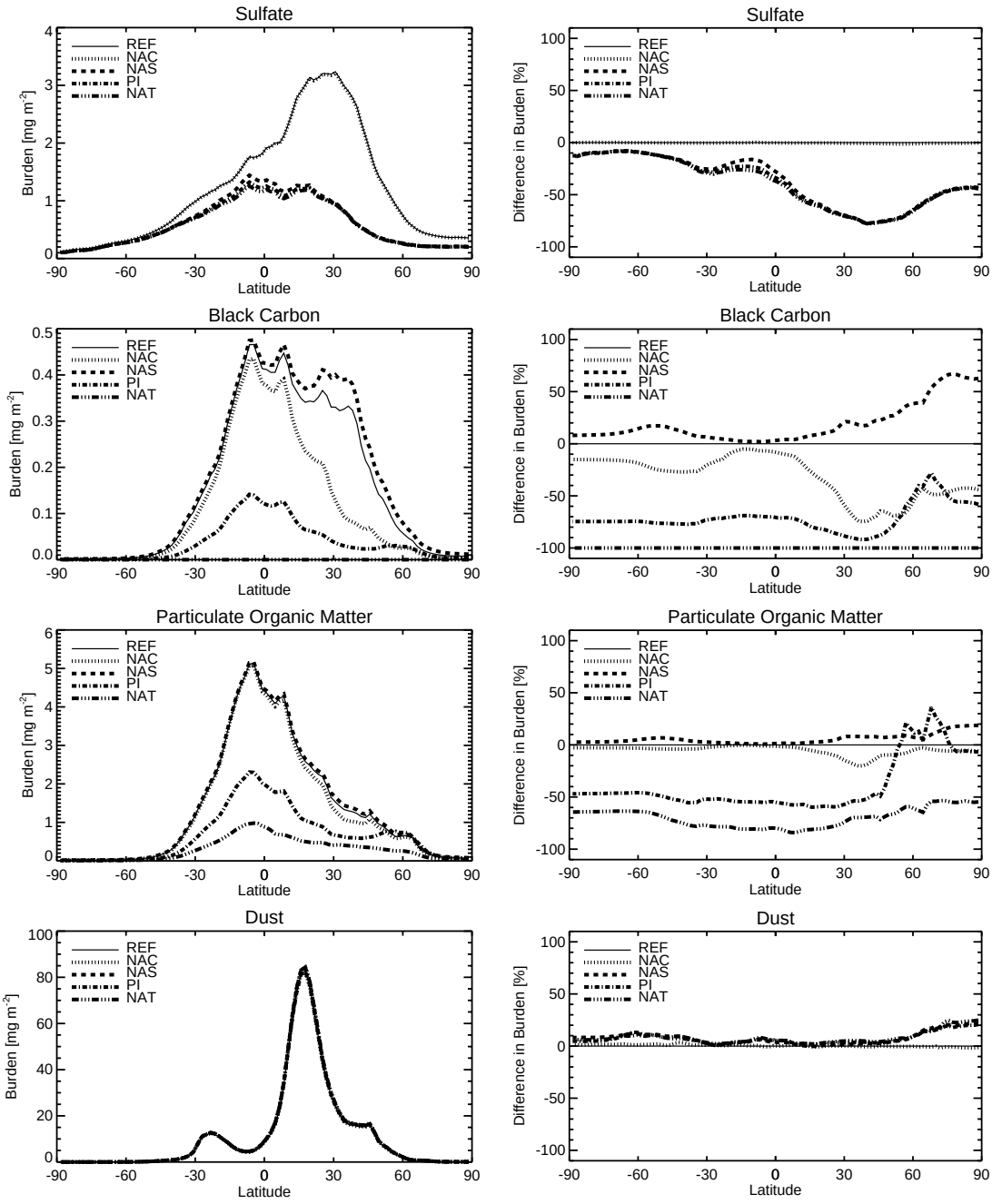

Figure 3.2: Annual zonal-mean aerosol column burdens in [Tg] and [Tg(S)] and the percent changes with respect to the reference scenario (REF) for the natural (NAT), the pre-industrial (PI), the scenario without SO_2 emissions (NAS) and without BC and POM emissions (NAC) from fossil-fuel and industry.

Species		REF	NAT	PI	NAS	NAC	NA
Sulfate	Sources	76.1	32.9	33.6	34.6	76.1	34.6
	Burden	0.80	0.38	0.39	0.41	0.79	0.41
	Life-time	3.8	4.2	4.3	4.3	3.8	4.3
Black	Emissions	7.7	-	1.4	7.7	4.7	4.7
Carbon	Burden	0.11	-	0.03	0.12	0.08	0.09
	Life-time	5.4	-	6.9	5.8	6.4	6.7
	Aging-time	0.7	-	0.3	1.9	0.5	0.9
Particulate	Emissions	66.3	19.1	34.0	66.3	62.9	62.9
Organic	Burden	0.99	0.21	0.46	1.01	0.95	0.97
Matter	Life-time	5.5	4.0	4.9	5.6	5.5	5.6
	Aging-time	1.1	0.5	0.9	2.0	1.0	1.5
Dust	Emissions [$\times 10^{-1}$]	66.2	67.2	66.9	66.2	66.5	66.5
	Burden	8.29	8.57	8.53	8.41	8.30	8.46
	Life-time	4.6	4.7	4.7	4.6	4.6	4.6
	Aging-time	4.9	7.7	7.8	8.0	4.8	7.9
Sea	Emissions [$\times 10^{-2}$]	50.1	50.2	50.2	50.0	50.1	50.1
Salt	Burden	10.45	10.45	10.44	10.43	10.44	10.44
	Life-time	0.8	0.8	0.8	0.8	0.8	0.8

Table 3.4: Global annual aerosol sources [Tg yr^{-1}] and annual-mean column burdens [Tg], life-time [days], and aging time for the insoluble fraction, for the reference (REF), the natural (NAT), the pre-industrial (PI), the scenario without SO_2 emissions from fossil-fuel, industry and bio-fuels (NAS), without BC and POM emissions (NAC) from fossil-fuel and industry, and without SO_2 emissions from fossil-fuel, industry and bio-fuels and without BC and POM emissions from fossil-fuel and industry (NA). Units of sulfate refer to [Tg(S)], emissions of dust and sea salt are scaled with 10^{-1} and 10^{-2}, respectively.

of aerosol numbers to changes in emissions is to be expected. In this paragraph we analyze the linearity of the changes of the aerosol numbers with respect to the (demonstrable non-linear) changes in the mass distribution.

The annual zonal-mean distribution of the aerosol number column burdens of each mode and their percent changes for the different scenarios are depicted in Fig. 3.3. Nucleation mode and Aitken mode soluble number burdens are dominated by nucleation of gas-phase sulfuric acid. Therefore, their decrease in the NAS, PI, and NAT scenarios is most pronounced in the Northern Hemisphere where most of the emission reductions occur compared to REF. It is interesting to note, that although the total source of gas-phase sulfuric acid decreases from the REF scenario to the NAS scenario by -13.8 Tg(S) yr^{-1} (-49.5 %), the global mean number burden of the soluble nucleation, Aitken, and accumulation modes decrease by -7.4 %, -16.9 % and by -21.1 %, respectively. This is an indication that the secondary production processes are saturated so that the nucleation mode number burdens are less than proportionally affected by changes in the sulfuric emissions. The global mean accumulation mode soluble number burden decreases from the REF scenario by -4.6 % for the NAC, by -42.3 % for the PI, and -56.7 % for the NAT scenario. As discernible in Fig. 3.3, the strongest decrease occurs in the Northern Hemisphere, where the anthropogenic contribution is large and the decrease of the emissions is most pronounced. Only the reduction of tropical biomass burning in the PI and NAT scenarios causes a distinct decrease of Southern Hemispheric accumulation mode number burdens. The effect of microphysical aging is most prominently cognizable in the changes of the insoluble Aitken mode number concentrations. With the decrease of the sulfate emissions in

the NAS scenario, the insoluble Aitken mode number burdens increase by up to 400 % with a maximum centered around 35°N. The analogue of this is that the number burdens of the insoluble accumulation and coarse modes increase with decreasing anthropogenic emissions in the NAS, PI, and NAT scenarios. Correspondingly, the peak of the soluble coarse mode number burden around 15°N, attributable to aged dust particles, is decreased. The reduction in primary particle emission in the NAC scenario decrease the insoluble Aitken mode number burden between 15°N and 70°N by up to -80 %.

For our analysis of the linearity, we focus on the soluble accumulation mode as it dominates the anthropogenic contribution to optical depth and cloud condensation nuclei and is therefore of fundamental importance for estimates of direct and indirect aerosol effects. Let λ be the ratio of the normalized change in vertically integrated aerosol numbers $\Delta\mathcal{N}$ to the normalized change in vertically integrated aerosol mass $\Delta\mathcal{M}$:

$$\lambda = \frac{\Delta\mathcal{N}}{\Delta\mathcal{M}} \equiv \frac{\left(N^{REF} - N\right)/N^{REF}}{\left(M^{REF} - M\right)/M^{REF}} \tag{3.1}$$

Hereby, are N, M the number and mass burden of the respective scenario and N^{REF}, M^{REF} the number and mass burdens of the reference scenario. We limit our analysis to cases of $\Delta\mathcal{M} > 1\%$ as λ can become ill-defined for $\Delta\mathcal{M} \to 0$. Values of $\lambda \approx 1$ indicate a linear change of aerosol mass and numbers. Values of $0 < \lambda < 1$ indicate that the relative change in aerosol numbers is less than the change in the aerosol mass compared to the reference scenario. For $\lambda > 1$ the relative change in aerosol numbers is larger than the change in aerosol mass compared to the reference scenario. Values of $\lambda < 0$ indicate anticorrelated changes of mass and numbers and are not of concern here.

The annual mean distributions of λ for the soluble accumulation mode for the NAC, NAS, NA, and NAT scenarios are displayed in Fig. 3.4a-d).

For the NAC scenario, λ is larger than one in the most regions with significant changes in the mass burden. This indicates that the changes in the number burden exceed the changes in the mass burden. That is, the anthropogenic carbonaceous emissions, with a large primary contribution, contribute disproportionately to the number of accumulation mode particles. In the continental plumes over the Northern Hemispheric oceans λ decreases with increasing distance from the sources, reaching values $\lambda \approx 1$. In high northern latitudes λ shows values $0 < \lambda < 1$. A possible explanation is that the increased microphysical sink in the source regions, introduced by the primary emissions, subsequently reduces the availability of sulfate for secondary particle formation in remote regions.

In contrast, for the NAS scenario λ is smaller than one close to the source regions and larger than one in the remote ocean regions. This indicates that the relative changes in the number burden is less than the changes in the mass burden close to the source and vice versa in remote regions and can be explained as follows. In the presence of sufficient aerosols, as in the anthropogenic source regions, an increase of the sulfate source from 34.6 Tg(S) yr^{-1} in NAS to 76.1 Tg(S) yr^{-1} in REF does not linearly increase the number of accumulation mode particles. A fraction of sulfate condenses on pre-existing particles and smaller particles preferentially coagulate with the available large particles, less than proportionally increasing the number of accumulation mode particles. (In the reference run, globally 36.4 % of the total sulfate source condensate on pre-existing aerosol particles.) In the remote regions, characterized by a lower available aerosol surface area and low primary sources, secondary particle formation accounts to a large fraction of the total accumulation mode number burden (*not shown*). Therefore, in these regions the

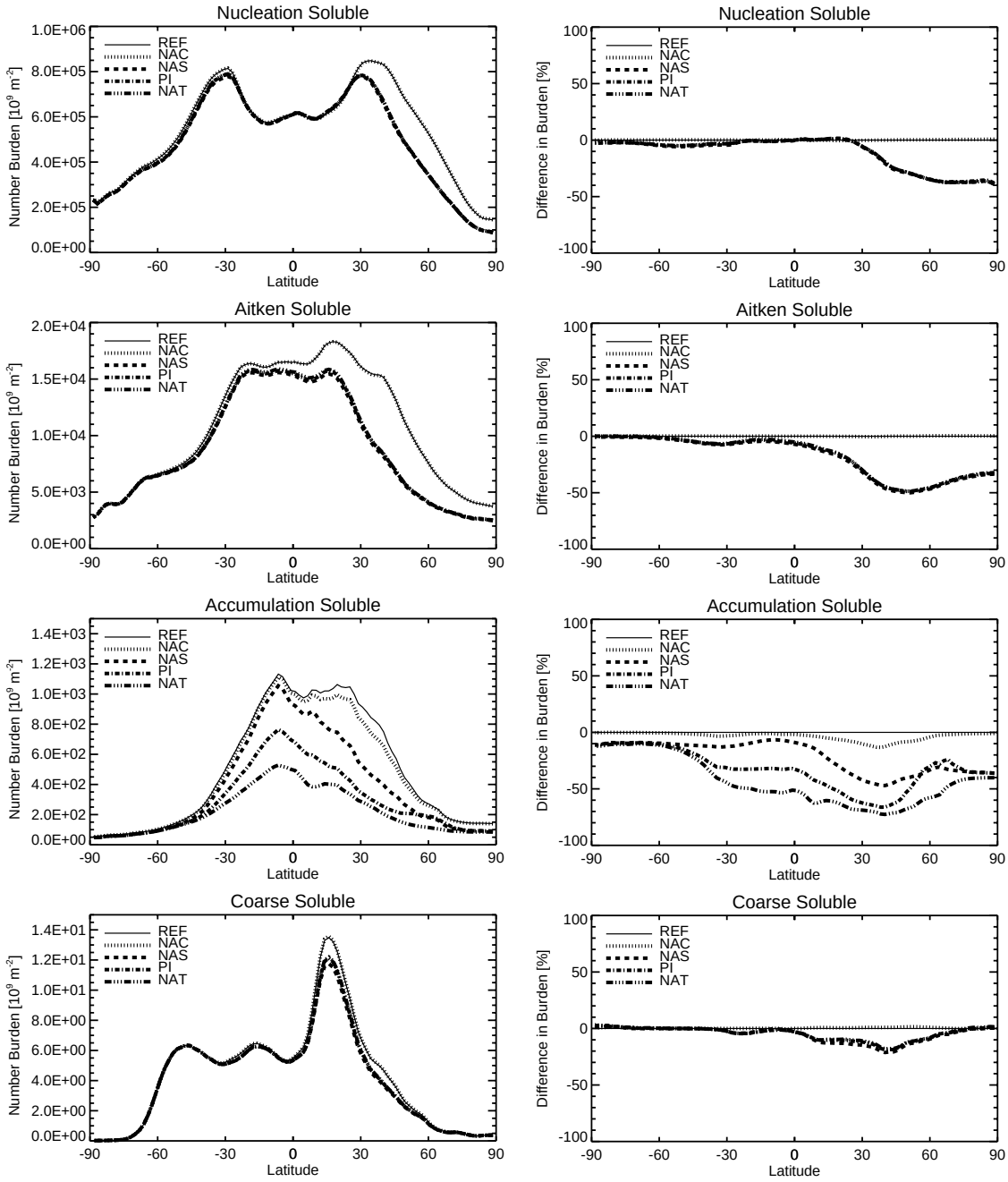

Figure 3.3: Annual zonal-mean aerosol number column burdens in [10^9 m^{-2}] for each mode and the percent changes with respect to the reference scenario (REF) for the natural (NAT), the pre-industrial (PI), the scenario without SO_2 emissions (NAS) and without BC and POM emissions (NAC) from fossil-fuel and industry.

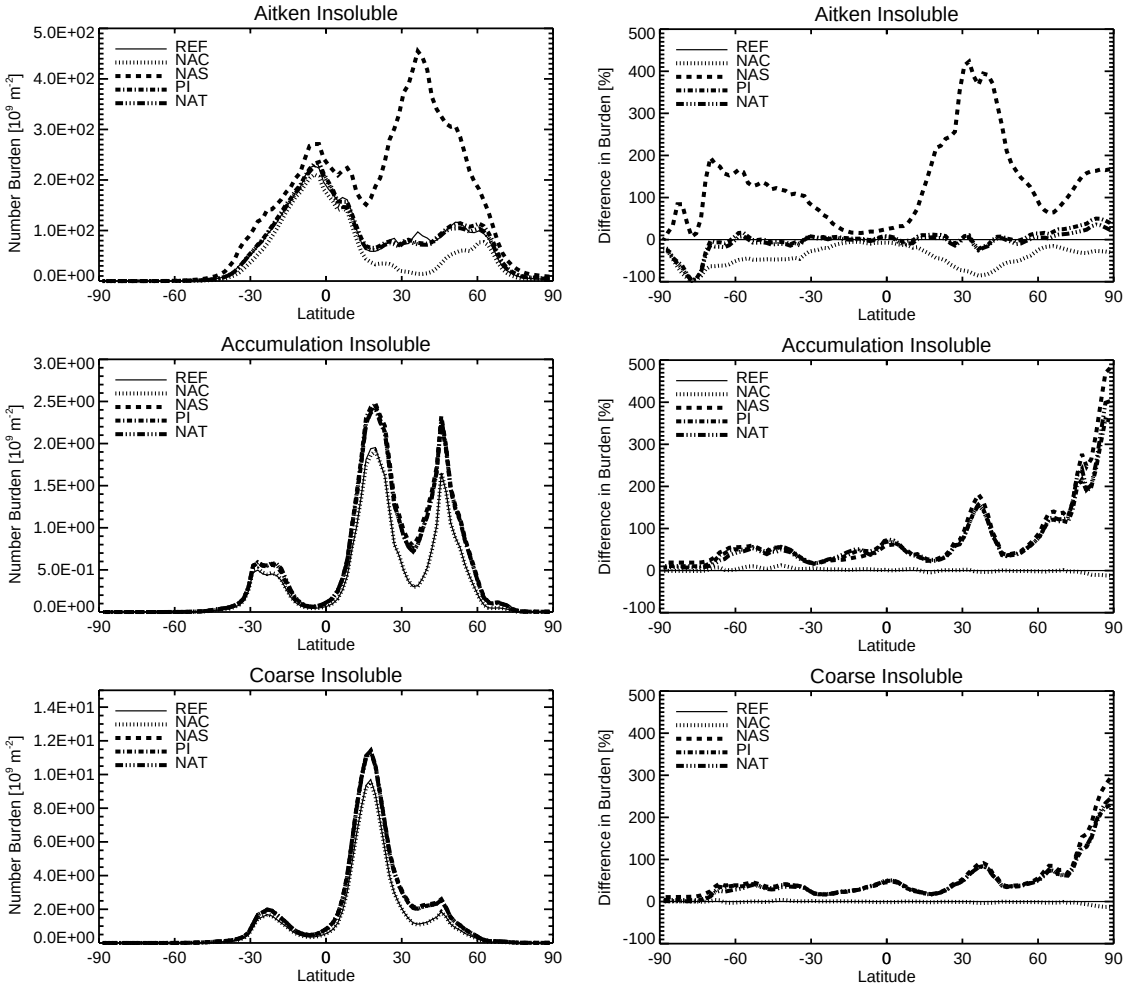

Figure 3.3: (continued)

increase of the sulfate source from NAS to REF disproportionately enhances the formation of accumulation mode particles via enhanced nucleation and growth processes.

The combined NA scenario shows a similar distribution of λ as the NAS scenario, as the aerosol mass source reductions in NAS are by more than one order in magnitude larger than in NAC (c.f. Table 3.4). However, in the source regions the small values of $\lambda < 1$ are partly compensated by the contribution of the primary emissions with $\lambda > 1$ as in the NAC scenario.

It is interesting to note that in the natural NAT scenario the main patterns of non-linearity still resemble the effect of the sulfuric emissions in the NAS scenario. However, the accumulation mode soluble particle numbers increase closer to linearity with the mass over large parts of the continents, indicated by values of $\lambda \approx 1$. One possible explanation is that the emissions of primary particles and of secondary particle precursors balance each other from natural to present day conditions resulting in the quasi-linear behavior over large parts of the continents. Over most part of the remote oceanic regions, values of $\lambda > 1$ indicate a disproportionate increase of the aerosol numbers compared to aerosol mass.

The disproportionate impact of primary emissions on accumulation mode particles, as surrogate for CCN, as indicated by the linearity analysis of the NAC scenario, has also been investigated

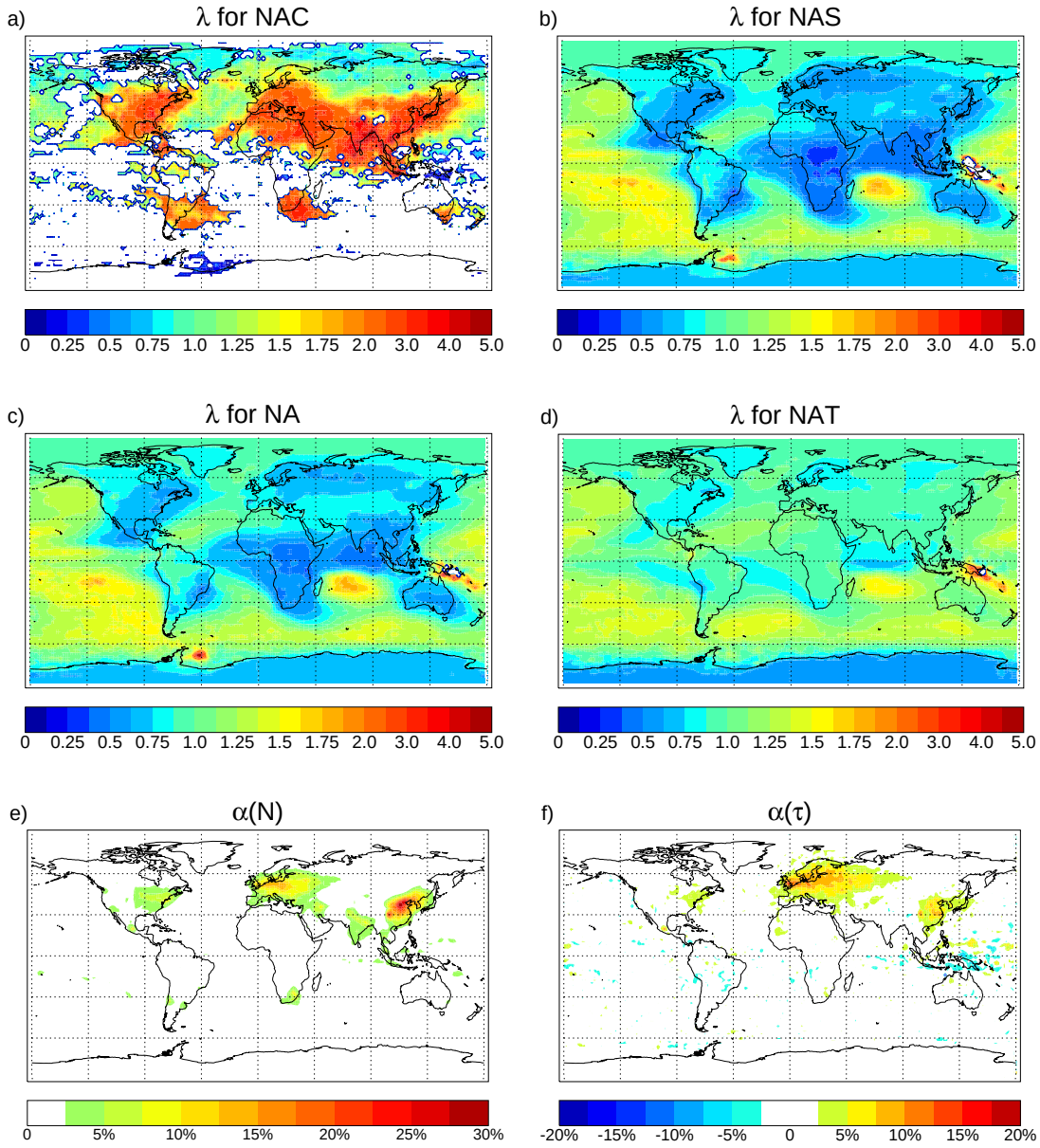

Figure 3.4: Annual mean non-linearity factor λ for the soluble accumulation mode as defined in Eq. (3.1) for a) the NAC, b) the NAS, c) the NA, and d) the NAT scenario. Annual mean additivity factor α as defined in Eq. (3.2) for e) the accumulation mode soluble number burden N and f) the aerosol optical depth τ at 550 nm, for the NAS and NAC scenarios compared to the NA scenario. Regions of λ with $\Delta\mathcal{M} < 1\%$ are masked out in a-d). Regions of α with $\tau^{REF} < 0.05$ are masked out in f).

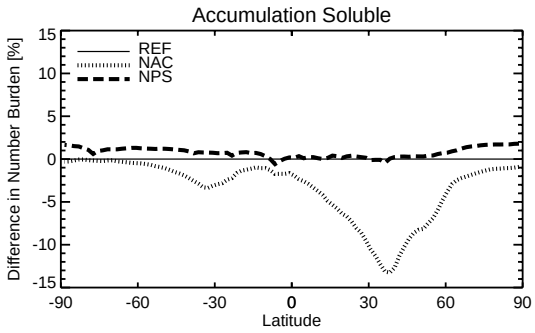

Figure 3.5: Annual zonal-mean change in accumulation mode soluble aerosol number column burdens for the scenario with no primary sulfate emissions (NPS) and the scenario without BC and POM emissions from fossil-fuel and industry (NAC), with respect to the reference scenario.

by Adams and Seinfeld (2002). As they did, we analyze the effect of assuming 2.5 % (Adams and Seinfeld (2002): 3 %) of total SO_2 emissions to be in form of primary sulfate in REF, following the recommendations of AEROCOM, by emitting 100 % of the SO_2 emissions as SO_2 in the NPS scenario. Aside from differences in the microphysics, the main difference of the model setup is that Adams and Seinfeld (2002) treat the idealized aerosol system consisting of sulfate and sea salt aerosols while in our set-up additionally black carbon, particulate organic matter, and mineral dust are considered. Fig. 3.5 shows the annual zonal-mean change in accumulation mode soluble number burdens for the NPS and for comparison for the scenario without carbonaceous emissions from fossil-fuel and industry (NAC). In our simulation, the neglect of primary sulfate emissions shows a negligible (< 1 %) effect on the zonal mean accumulation mode soluble number concentration in the regions with a significant number burden (c.f. Fig. 3.3). A small increase up to 2 % occurs in the remote regions compared to a reduction by up to -13 % for the neglect of carbonaceous emissions from fossil-fuel use and industry. This difference to the strong positive effect of primary sulfate emission on CCN numbers, as found by Adams and Seinfeld (2002), can most likely be attributed to the inclusion of more relevant aerosol components in HAM.
In summary, the analysis of the response of aerosol number burdens to emission changes reveals distinct non-linearities. Strongest non-linearities occur in the vicinity of the aerosol source regions. Primary aerosols contribute preferentially to the formation of accumulation mode particles. Increasing emissions of secondary aerosol precursors less than proportionally increase the accumulation mode aerosol numbers close to the sources and disproportionately increase the accumulation mode aerosol numbers in the remote regions.

3.3.3 Response of Aerosol Optical Depth

We demonstrated that aerosol mass and aerosol number respond non-linearly to changes in aerosol emissions. The optical depth in turn is non-linearly coupled to the aerosol numbers and mass via the size-distribution, composition, and mixing state. Therefore, a non-linear response of the aerosol optical thickness to emission changes is to be expected and not further investigated. The annual zonal-mean distribution of the aerosol optical depth (τ) and the percent changes for the different scenarios are depicted in Fig. 3.6. The strongest effect of anthropogenic emissions on τ can be attributed to the sulfuric emission from fossil-fuels, industry, and bio-fuels. In the NAS scenario, zonal-mean optical depths between 20°N and 70°N decrease by up to -50 %. Regionally, close to the North American and Asian anthropogenic sulfuric source regions, the

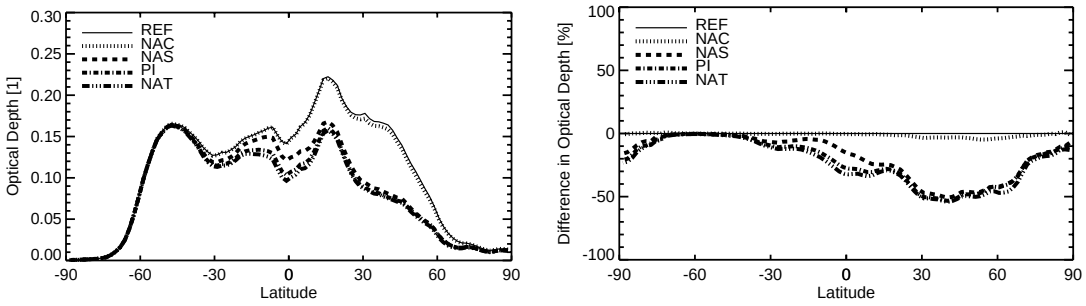

Figure 3.6: Annual zonal-mean aerosol optical depth at a wavelength of 550 nm and the percent changes with respect to the reference scenario (REF) for the natural (NAT), the pre-industrial (PI), the scenario without SO_2 emissions (NAS) and without BC and POM emissions (NAC) from fossil-fuel and industry.

reduction reaches more than -80 % (*not shown*).
The effect of the reduction of carbonaceous emissions in the NAC scenario on the annual zonal-mean of τ is less than -5 %. Regionally, close to the European and Asian source regions of carbonaceous aerosols from fossil-fuels and industry the reductions reach around -15 % (*not shown*). The maximal zonal-mean difference between the NAS and PI and between the NAS and NAT scenarios, attributable to the reduction in biomass burning, is discernible in the tropics, reaching -15 % and -20 % at the equator, respectively. The influence of anthropogenic emission on the zonal-mean aerosol optical thickness in the extra-tropical Southern Hemisphere is small.

3.3.4 Analysis of the Additivity

In the development of emission strategies for aerosol and their precursors, it is of fundamental importance to forecast the total effect of a number of concurrent emission changes. In bulk aerosol models, traditionally used for the assessment of aerosol effects, the change in the aerosol system from a simulation with emission changes for several compounds is the sum of changes of single simulations in each of which one the emission changes was introduced. That is, the response of the aerosol system is constrained to the concept of additivity. This is the underlying principle of the forcing concept applied for the analysis of the radiative effects of aerosols in the IPCC (2001) assessment report.
Here, we analyze the additivity of the microphysically coupled aerosol system, taking into account the coherence of aerosol cycles demonstrated in Sections 3.3.1, 3.3.2. We compare the results from the NAC and NAS scenarios to the NA scenario in which the emission reductions from both scenarios are combined. Let α be a measure of the additivity for the quantity X defined as:

$$\alpha(X) = \frac{\Delta X^{NA} - \Delta X^{NAS} - \Delta X^{NAC}}{X^{REF}} \tag{3.2}$$

Hereby are $\Delta X^i = X^i - X^{REF}$ for the scenarios $i \in$ (NA, NAS, NAC). If the aerosol system follows additivity α is zero as $\Delta X^{NA} = \Delta X^{NAS} + \Delta X^{NAC}$.
The global distribution of α for the accumulation mode soluble number burden (N) is shown in Fig. 3.4e). Close to the anthropogenic source regions, $\alpha(N)$ shows a positive deviation from additivity, reaching up to 30 %. That is the sum of (negative) changes in the NAS and NAC scenarios is lower than the combined (negative) change in the NA scenario. Conceptually starting from the NA scenario, the increase of N due to separately increasing the sulfate sources

(NAC) and the carbonaceous sources (NAS) is more efficient than the increase of N due to the combined increase of sulfate and carbonaceous sources. The reason is that the microphysical interactions increase with increasing aerosol concentrations so that growth processes become more important. Therefore, the co-emission of several compounds can reduce the efficiency with which accumulation mode particles are formed from the emissions. The corresponding deviations from additivity, reaching up to 15 %, are also evident in the distribution of $\alpha(\tau)$ for the aerosol optical depth, displayed in Fig. 3.4f). This can be attributed to the fact that the aerosol optical depth over the the anthropogenic source regions is dominated by the contribution of aerosols from the accumulation mode soluble. Therefore, a weaker decrease of N in the NA scenario compared to the combination of the NAC and NAS scenarios, results in a corresponding behavior of the aerosol optical depth. For both, accumulation mode number burdens and optical depths, the largest deviations from additivity occur in the main anthropogenic aerosol source regions. The regional distribution of the relative emission changes (*not shown*) is more evenly distributed over the northern hemispheric continents. This suggests that the deviations from additivity increase with increasing aerosol and precursor concentrations, as the microphysical interactions increase.

3.4 Summary and Conclusions

In a series of simulations with the ECHAM5-HAM aerosol-climate model, we analyzed the response of the global aerosol system to changes in anthropogenic emissions. In the microphysical aerosol module HAM, sink processes and radiative properties are parameterized in terms of prognosed size-distribution, mixing-state, and composition, establishing degrees of freedom for non-linear responses of the aerosol system. The large-scale meteorology in each simulation was constrained to year 2000 ECMWF ERA40 reanalysis data. From a reference simulation with year 2000 emissions, we progressively reduced the emission of specific anthropogenic aerosols and aerosol precursors. We consider a scenario without SO_2 emissions from fossil-fuel use and industry and bio-fuels (NAS), a scenario without BC and POM emissions from fossil-fuel use and industry (NAC), and a combined scenario without SO_2 emissions from fossil-fuel use, industry and bio-fuels and without BC and POM emissions from fossil-fuel use and industry (NA). Additionally, we consider a pre-industrial scenario with emissions for the year 1750 (PI) and a scenario with solely natural emissions (NAT).

The analysis of the response of the global aerosol system to the emission changes reveals significant non-linearities. Global annual-mean mass-burdens respond non-linearly to the induced emission changes, manifested in alterations of the aerosol life-times. From pre-industrial to present day aerosol emissions, the life-time of sulfate decreased by -10.2 %, of black carbon decreased by -22.6 %, for particulate organic matter increased by 10.6 %, and for mineral dust decreased by -1.9 %. The natural sea salt cycle is unaffected by the anthropogenic emissions and shows only negligible variations.

The impact of specific anthropogenic emission reductions on aerosol cycles with unaltered emissions, manifested in increased life-times, column burdens, and microphysical aging-times, is a clear indicator for the coherence of the aerosol cycles. In the scenario without anthropogenic sulfate emissions, annual global-mean life-times of black carbon, particulate organic matter, and dust increase by 8.9 %, 2.5 %, and 1.5 %, microphysical aging-times increase by 164 %, 84 %, and 66 %, and annual zonal-mean column burdens in high northern latitudes increase by up to 70 %, 20 %, and 20 %, respectively.

A linearity analysis of the changes of accumulation mode soluble number burdens with respect

to the corresponding changes in mass burden indicated substantial non-linearities. Comparing the NAC scenario with the reference scenario, anthropogenic carbonaceous emissions disproportionately contribute to the accumulation mode number burden, particularly close to the source regions. In contrast, anthropogenic sulfuric emissions less than proportionally contribute to the accumulation mode number burden close to the source regions and disproportionately contribute in remote regions. From natural to present day conditions, the increase of both carbonaceous and sulfuric emissions partly off-set these non-linearities. However, the main patterns of non-linearity still resemble the effect of the sulfuric emissions, though with reduced amplitude. In contrast to the effect of the neglect of the carbonaceous emissions in the NAC scenario, a neglect of the assumption to emit 2.5 % of total sulfuric emission in the reference scenario as primary sulfate, is negligible.

We analyzed the additivity of the aerosol system by comparing the sum of the changes from the NAS and NAC scenarios with respect to the reference scenario, with the change from the NA scenario in which the emission changes of NAS and NAC are combined. For the accumulation mode soluble number burden and the aerosol optical depth, considerable deviations from additivity occur close to the main anthropogenic source regions where the aerosol concentrations are highest. There, the enhanced microphysical interactions in the combined NA scenario result in a up to 30 % reduced change of the number burden when compared with the sum of the changes from the separate NAS and NAC scenarios. That is, the co-emission of the carbonaceous and sulfuric aerosol components reduces the efficiency with which accumulation mode particles are formed from the emissions. The resulting aerosol optical depth shows an analogue behavior with local deviations from additivity up to 15 %.

The demonstrated non-linearities, the coherence among the different aerosol cycles, and the deviations from additivity, challenge the bulk approach established in global aerosol models. Bulk models do not provide the degrees of freedom for these effects to be included. In addition, our results suggest that the separate perception of the different aerosol components and their precursors can lead to non-negligible errors in estimates of the aerosol radiative effects. Traditionally, the radiative effects of specific aerosol components have been derived separately. Our results, in contrast, suggest that estimates of the contribution of specific aerosol components to the radiative effects require simulations with the fully coupled aerosol system but the component of interest omitted.

There are manifold potential impacts of our results on the global climate system. We showed that changes in anthropogenic emissions affect the microphysical aging capacity of the atmosphere which in turn affects the aerosol life-times, global distributions and radiative effects. The demonstrated increase in the transfer of insoluble to soluble particles due to anthropogenic emissions potentially increases the number of CCN affecting the indirect aerosol effects. The exposed deviations from additivity challenge the concept of radiative forcing applied in IPCC (2001) for the assessment of the aerosol radiative effects. The anthropogenic modulation of the high latitude aerosol concentrations and deposition rates - also of natural components - has consequences for the interpretation of ice core data. It suggests that the aerosol concentration in ice cores might not be such a direct measure of the atmospheric aerosol load as previously assumed (e.g. Kohfeld and Harrison (2001)). For example, the omission of anthropogenic sulfur emissions increases the high latitudes dust deposition by up to 20 %, while the global dust mass burden is only increased by 1.5 %. The strong increase of black carbon at high northern latitudes due to the omission of anthropogenic sulfuric emissions should be emphasized. This region is prone to changes in the surface albedo and ice feedbacks and it has been proposed that black carbon deposition on snow and ice exerts a significant positive climate forcing (Hansen and Nazarenko,

2004). Enhanced deposition of black carbon due to mitigation of sulfuric aerosol precursors could amplify this effect. This example emphasizes the need for integrated emission strategies for aerosols and their precursors comprising the cross-connections of the global aerosol cycles.
Although the used ECHAM5-HAM aerosol-climate model is advanced in terms of the aerosol representation and microphysical detail compared to most previous global models suitable for long-term simulations, large uncertainties remain. Important aerosol components such as nitrate as well as important processes such as the treatment of semi-volatile species are neglected. In particular the fact that secondary organic aerosols are substituted by a primary approach constitutes an underestimation of the amount of condensable material and therefore of the coupling of the aerosol cycles. Large uncertainties are also associated with the scavenging ratios of the insoluble and soluble modes, with the nucleation of gas-phase aerosol precursors, and with the accommodation coefficients for the condensation of gases on pre-existing aerosols. However, these uncertainties do not affect the conclusion that the global aerosol system is characterized by inherent non-linearities that cannot be accounted for in the traditional bulk modeling approach. Further studies with advanced global aerosol models are required to reduce the associated uncertainties and to constrain the impacts on the aerosol radiative effects.

Acknowledgments This work was supported by the German climate research program DEKLIM. Review comments by Stefan Kinne, Erich Roeckner, and Martin Schultz greatly improved this manuscript.

Chapter 4

Towards the Assessment of the Aerosol Radiative Effects

The ECHAM5-HAM aerosol-climate model provides the basis for a mechanistic calculation of the aerosol radiative effects. The aerosol radiative properties are calculated online from the prognosed aerosol size-distribution, composition, and mixing state and are provided to the ECHAM5 radiation scheme. In this chapter, methods and first applications of the ECHAM5-HAM aerosol model towards the assessment of the aerosol radiative effects are presented. A measure suitable for the assessment of all aerosol radiative effects is introduced and applied to estimate direct and semi-direct aerosol effects. An extension of the ECHAM5 stratiform cloud scheme with prognostic treatment of cloud droplet numbers and ice crystal numbers is described. Two alternative methods for the coupling of the HAM aerosol distribution and the extended cloud scheme are introduced. First results from the aerosol-cloud coupling are presented and evaluated with satellite data. A detailed investigation of the aerosol radiative effects is beyond the scope of this study. Transient long-term climate simulations with HAM as part of the Max Planck Institute Earth System Model are ongoing and will be subject of forthcoming publications.

4.1 A Measure for Aerosol Radiative Effects

Following IPCC (2001), direct aerosol radiative effects are generally measured in terms of radiative forcing (c.f. Section 1.4). However, the stringent concept of radiative forcing is not applicable to all aerosol radiative effects as it is limited to externally imposed disturbances. Aerosol effects such as the semi-direct and the cloud-lifetime effect involve internal feedbacks to changes in cloud liquid water and cloud amount and are therefore not included in the forcing definition. However, as demonstrated in Chapter 3, also the microphysically coupled aerosol system is characterised by inherent coherences and non-linearities, causing non-negligible deviations from additivity. Therefore, in a strict sense, emission changes of specific aerosols or aerosol precursors do not satisfy the definition as external perturbation because of the internal aerosol microphysical interactions and feedbacks. Additionally, due to the demonstrated microphysical interactions and deviations from additivity, the resulting radiative disturbance will differ if the perturbation is introduced to the undisturbed system (natural atmosphere) or to an already disturbed system (polluted atmosphere). Therefore, as a measure of the current radiative disturbance of a specific aerosol species it seems more appropriate to define the perturbation by the omission of the respective species from the current disturbed (polluted) state than by the

introduction of the species to the undisturbed (natural) state, as it is done in the forcing concept applied in IPCC (2001). It has to be pointed out again that the demonstrated deviations from additivity indicate that the sum of individual radiative disturbances is not representative for the total radiative disturbance. Nonetheless, a first order measure of the individual radiative effects is desirable.

Based on this considerations a measure applicable for all aerosol radiative effects, the large-scale constrained radiative perturbation (P_L), is introduced:
"The large-scale constrained radiative perturbation of the surface-troposphere system due to the omission of a perturbation or agent is the change in net irradiance at the top of the atmosphere in two simulations in one of which the perturbation or agent is omitted, with the sea surface temperature and large-scale dynamical state held fixed at the unperturbed values."
This could be seen as large-scale constrained extension of the "forcing" expression that has been used in Lohmann and Feichter (1997) and termed "quasi forcing" by Rotstayn and Penner (2001). Practically, this form of radiative perturbation can be derived in global circulation models with nudging capabilities as the difference in top of the atmosphere irradiance from two simulations in one of which the respective perturbation or agent is omitted. Nudging refers to the relaxation of the prognostic dynamic variables towards an atmospheric reference state with prescribed SST and sea-ice distribution (Jeuken et al., 1996). Depending on the strength of the relaxation towards the reference meteorology, the atmosphere has the degrees of freedom to locally adjust to feedback processes while maintaining an undisturbed state on the large scale.
A range of redefined forcing expressions are discussed in Hansen et al. (1997, 2002) and defined here by the illustrations in Figure 4.1.

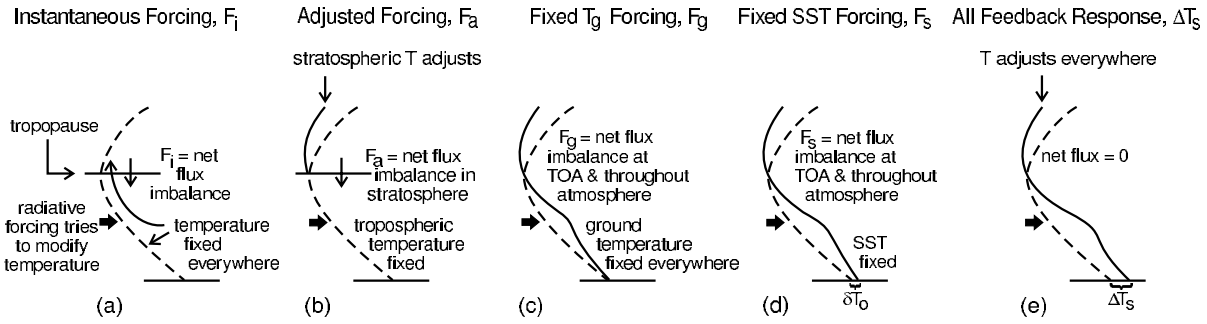

Figure 4.1: Illustration defining a) instantaneous forcing F_i, b) adjusted forcing F_a, c) fixed ground temperature forcing F_g, d) fixed SST forcing F_S, and e) all feedback response. From Hansen et al. (2002).

According to these definitions, the large-scale constrained radiative perturbation could be classified as top of the atmosphere instantaneous forcing on the large-scale, with all feedback response on the local-scale.
As test case for this practicable definition, a CO_2-doubling experiment in the nudging mode of the ECHAM5 GCM was performed. In the simulations the large-scale meteorology is relaxed towards ECMWF ERA40 reanalysis data (Simmons and Gibson, 2000) for the year 2000. A resolution of horizontally T63 in spectral space is used with a corresponding resolution of $1.8° \times 1.8°$ on a Gaussian grid. The vertical resolution is set to 31 levels, extending from the surface up to 10 hPa. In one of the simulations the CO_2 concentration is doubled from the standard value of 348 ppm to 696 ppm. The large-scale constrained radiative perturbation due to CO_2-doubling is then

calculated as the annual-mean difference of the net irradiance at the top of the atmosphere. The resulting P_L should have a similar value as the "traditional" instantaneous top of the atmosphere radiative forcing. Local scale processes, most importantly clouds, have the degrees of freedom to respond.
The annual-mean large-scale constrained radiative perturbation for CO_2-doubling is displayed in Figure 4.2.

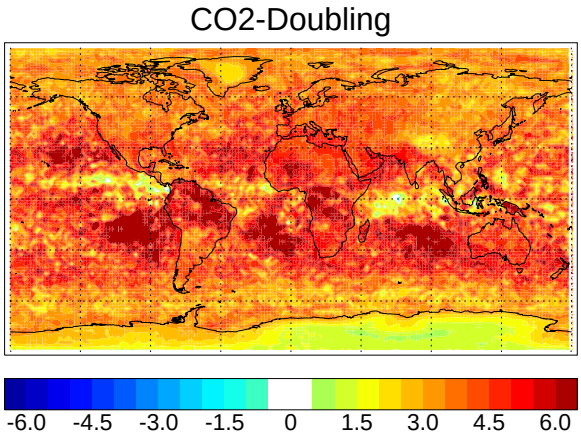

Figure 4.2: Annual-mean large-scale constrained radiative perturbation [$W\,m^{-2}$] for CO_2-doubling from 348 ppm to 696 ppm. The annual global-mean value is +4.3 $W\,m^{-2}$.

The local-scale cloud variations are clearly discernible due to the relatively short one year integration period. However, the annual global-mean value of +4.3 $W\,m^{-2}$ is in good agreement with the annual global-mean instantaneous forcing of +4.2 $W\,m^{-2}$ (4.0 $W\,m^{-2}$ with stratospheric adjustment) from a CO_2-doubling experiment performed with the ECHAM5 GCM (Erich Roeckner, *pers. comm.*). For aerosols, the difference between instantaneous and adjusted forcing is believed to be smaller (Houghton et al., 1994).
In conclusion, subject to a more detailed investigation, P_L serves as good first order estimate of the aerosol radiative disturbance even for short integration periods, applicable for a consistent assessment of all aerosol effects.

4.2 Direct and Semi-Direct Aerosol Effects

The explicit online calculation of the aerosol radiative properties for the ECHAM5 radiation scheme (c.f. Section 2.2.8) provides the basis for the calculation of the direct and semi-direct aerosol radiative effects. A series of simulations with ECHAM5-HAM nudged to year 2000 ECMWF ERA40 reanalysis data is performed at a resolution of horizontally T63 in spectral space with a corresponding resolution of $1.8° \times 1.8°$ on a Gaussian grid. The vertical resolution is set to 31 levels, extending from the surface up to 10 hPa. Although an extension of the aerosol radiation module, including the terrestrial part of the spectrum, has now been implemented into HAM, in these calculation only the solar part of the spectrum is considered for the aerosol radiative properties. However, except for mineral dust, the radiative perturbations in the terrestrial part of the spectrum are believed to be small and do therefore not significantly affect the anthropogenic aerosol radiative perturbations (Haywood et al., 1997b; Penner et al., 2001).

Based on the methods introduced in the preceeding section, the combined direct and semi-direct large-scale constrained radiative perturbation is analysed for three different anthropogenic emission scenarios: First, for carbonaceous emissions from fossil-fuels and industry. Second, for sulfuric emissions from fossil-fuels, industry, and bio-fuels. Third, for all anthropogenic aerosol and aerosol precursor emissions. These scenarios correspond to the NAC, NAS, and NAT scenarios introduced in Chapter 3, respectively. Annual-mean clear-sky and total-sky values of P_L for the three scenarios are depicted in Figure 4.3 and the annual global-mean values of P_L are given in Table 4.1. As the simulations were performed with interactively coupled radiation, the calculated radiative perturbations constitute the combination of direct and semi-direct aerosol effects.

Scenario	**Clear-Sky**	**Total-Sky**
Carbonaceous emissions from fossil-fuel use and industry	+0.08	+0.11
Sulfuric emissions from fossil-fuel use, industry and bio-fuels	-0.69	-0.46
Total anthropogenic emissions	-0.49	-0.12

Table 4.1: Annual global-mean large-scale constrained radiative perturbations [$\mathrm{W\,m^{-2}}$] for three emission scenarios.

In the total-sky distributions of P_L in Figure 4.3 the local-scale cloud variations cause a noisy structure due to the short one-year integration period. Nonetheless, good agreement with the instantaneous forcing in the CO_2-doubling experiment support the assumption that these variations are random. The relevant coherent features of the respective perturbations are clearly discernible.

Beside the semi-direct aerosol effect, the impact of clouds on the total-sky aerosol radiative perturbations depends on the relative height of the aerosol and cloud layers. On the one hand, clouds overlying the respective aerosol layer will dominate the total optical depth and render the underlying aerosol negligible. Analogue, a layer of scattering aerosols over a cloud layer will have a negligible impact. On the other hand, a layer of absorbing aerosols over a cloud layer can significantly reduce the high planetary albedo caused by the brightness of the underlying clouds. The radiative effects of aerosol embedded in clouds, particularly of absorbing aerosols, are more complex and not taken into account in these simulations.

The radiative perturbation P_L of the carbonaceous aerosols from fossil-fuels and industry is generally positive, indicating the predominance of absorption. Highest values are found over the main source regions (c.f. Figure 2.1). However, P_L is also high over areas with a high surface albedo such as the desert regions in Africa and the Middle East. The positive radiative perturbation over north-central Europe and China is higher for the total-sky case than for the clear-sky case. A clear separation of direct and semi-direct aerosol effects is not possible in this configuration. However, an analysis of the cloud cover differences (*not shown*) revealed only small changes, suggesting the predominance of the effect of absorbing aerosol above clouds over the semi-direct effect. The annual global-mean clear-sky and total-sky values of P_L are positive with +0.08 and +0.11 $\mathrm{W\,m^{-2}}$, respectively.
For aerosols originating from sulfuric emissions from fossil-fuels, industry, and bio-fuels, the

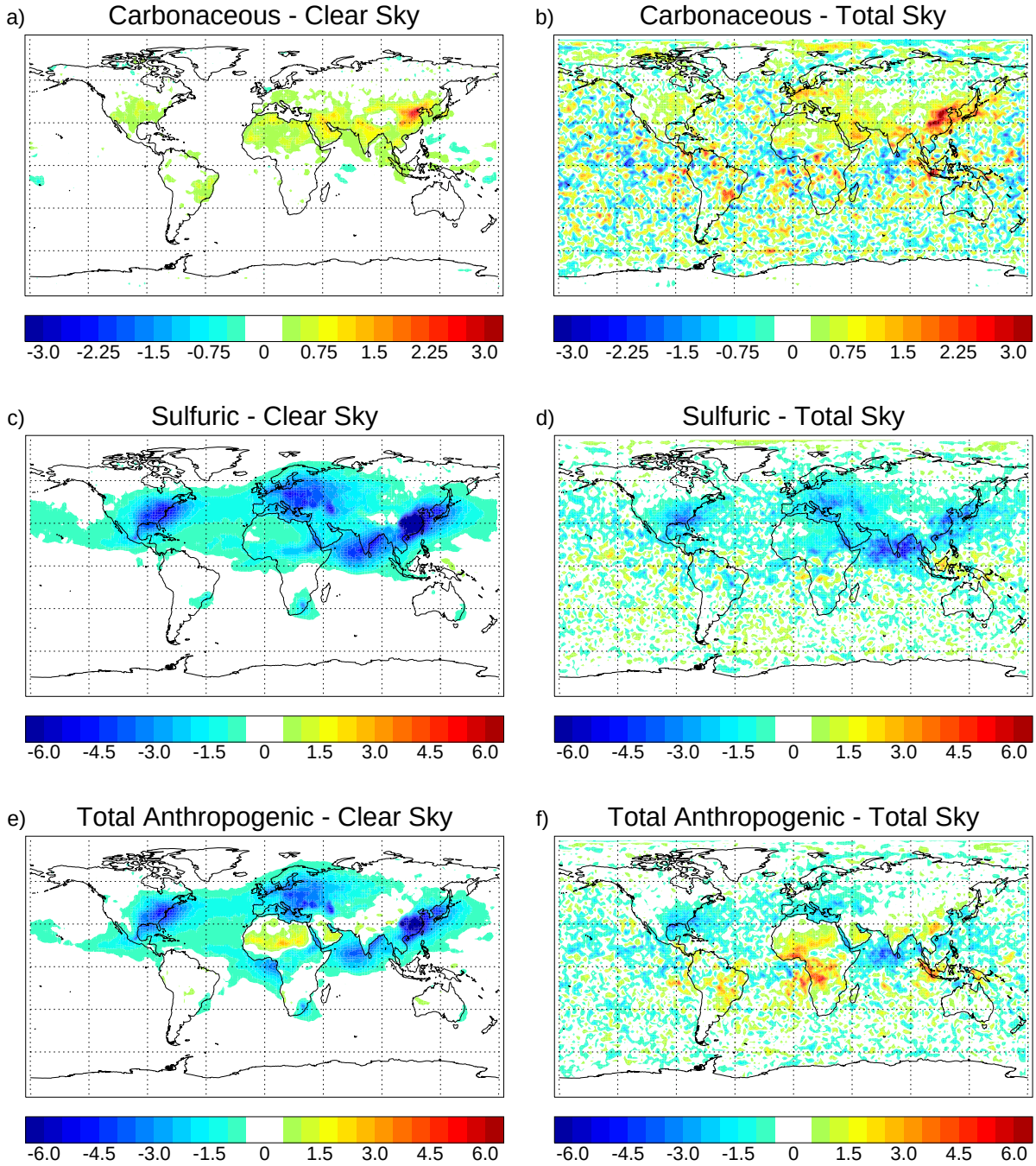

Figure 4.3: Clear-sky and total-sky annual-mean large-scale constrained radiative perturbation [$\mathrm{W\,m^{-2}}$] a),b) for carbonaceous emissions from fossil-fuels and industry, c),d) for sulfuric emissions from fossil-fuels, industry, and bio-fuels, e),f) all anthropogenic aerosol and aerosol precursor emissions, respectively. Note the different scale in a)-b) and in c)-f).

clear-sky P_L shows negative values of up to -6 $W\,m^{-2}$ around China, India, Central and East Europe and the East Coast of North America, indicative for the predominance of scattering and a cooling effect. The effect of long-range transport is clearly discernible in the radiative disturbances of the plumes of North America and Asia over the North Atlantic and North Pacific, respectively. The total-sky effect, in particular at higher latitudes, is reduced, as underlying or overlying clouds render the scattering by aerosols negligible. This causes a reduction of the annual global-mean values of P_L from -0.69 $W\,m^{-2}$ clear-sky to -0.46 $W\,m^{-2}$ total-sky.
To determine the total direct and semi-direct anthropogenic P_L, all anthropogenic emissions, originating from fossil-fuel, bio-fuel use, industry, and vegetation fires, are deactivated so that only the natural emissions remain. The clear-sky radiative perturbation P_L shows a pattern of negative values resembling the perturbation caused by the sulfuric emissions with the strongest cooling around China, India, Central and East Europe and the East Coast of North America. These perturbations are less pronounced than for the sulfuric emissions. Over highly reflective surfaces as over northern Africa and the Middle East, P_L is positive, attributable to the influence of absorbing aerosols from biomass burning and fossil-fuel use. The effect of absorbing aerosols is distinctively enhanced in the total-sky values of P_L, with strongly positive perturbations of up to $+5$ $W\,m^{-2}$ in the biomass burning regions in Central Africa, South America, and the Maritime Continent, attributable to the influence of underlying clouds and the semi-direct aerosol effect. In South-Asia and South-East Asia, the cooling aerosol effect of the clear-sky perturbations are regionally compensated or overcompensated by absorption effects in the total-sky radiative perturbations. The annual global-mean anthropogenic direct and semi-direct aerosol radiative perturbation P_L is reduced from -0.49 $W\,m^{-2}$ clear-sky to -0.12 $W\,m^{-2}$ total-sky.
The distinct effect of absorbing aerosols in these simulations is enhanced by the fact that the predominant anthropogenic absorbing aerosol component, black carbon, is partly internally mixed with otherwise predominantly scattering aerosol components, such as sulfates and particulate organic matter. The volume-weighted calculation of the refractive indices for the internally-mixed modes results in higher absorption cross-sections than for the simplified externally mixed approach. However, it gives also higher absorption cross-sections than the more realistic core-shell approach and constitutes therefore an upper estimate of the effect of the aerosol absorption cross section (Jacobson, 2000). On the other hand, the underlying emission inventory for carbonaceous aerosols from fossil-fuel use and industry (Bond et al., 2004) yields significantly lower carbonaceous emission than previous estimates (Liousse et al., 1996; Cooke et al., 1999). It has been suggested that these emissions could constitute an underestimate for Europe (Schaap et al., 2004). This is consistent with the underestimation of the ECHAM5-HAM simulated absorption optical-depth over Europe, evident in Figure 2.9. Therefore, the pronounced positive radiative perturbance due to aerosol absorption does not necessarily constitute an overestimation.

4.3 Indirect Aerosol Effects

Most previous modelling studies of the indirect aerosol effects were based on bulk mass models. As the size-distribution is no prognostic parameter in bulk models, an explicit derivation of the number of activated aerosol particles is not possible. Therefore, the number of activated particles has traditionally been implicitly derived from empirical relationships between aerosol mass and the cloud droplet number concentration (Boucher and Lohmann, 1995; Roelofs et al., 1998). Alternatively, the number of aerosols has been derived from the simulated aerosol mass, assuming pre-scribed size-distributions, and then empirically related to CDNC (Lohmann et al., 1999a). In ECHAM5-HAM, the parameterisation of the aerosol-cloud interactions is based on

the prognostic treatment of size-distribution, composition, and mixing state.

4.3.1 Extended Cloud Parameterisation

An extended microphysical parameterisation for stratiform clouds has been implemented into ECHAM5, in co-operation with Ulrike Lohmann[1], Junhua Zhang[2], and Erich Roeckner[3]. This cloud-microphysical parameterisation extends the standard stratiform cloud scheme of ECHAM5 (Lohmann and Roeckner, 1996) with a prognostic treatment of the cloud droplet number concentration, following Lohmann et al. (1999a) and ice crystal number concentration, following Lohmann (2002) and Lohmann and Kärcher (2002). A detailed description of the schemes is given in the original references. Here, only a brief outline of the parameterisations and references to enhancements from the original schemes are given.

The prognostic equation for the cloud droplet number concentration (N_l) is given by:

$$\frac{\partial N_l}{\partial t} = R(N_l) + Q_{nucl} - Q_{autn} - Q_{self} - \frac{N_l}{q_l}\left(Q_{racl} + Q_{sacl} + Q_{frz} + Q_{eva}\right) + Q_{mlt} \qquad (4.1)$$

where $R(N_l)$ represents the rate of change due to large-scale, turbulent, and convective transport processes. q_l is the liquid water content. Q_{nucl} represents the nucleation of cloud droplets and is discussed in Section 4.3.2. The other terms represent the microphysical processes autoconversion Q_{autn}, self collection of cloud droplets Q_{self}, accretion of cloud droplets by rain Q_{racl} and snow Q_{sacl}, freezing of cloud droplets Q_{frz}, evaporation of cloud droplets Q_{eva}, and melting of ice crystals Q_{mlt}. As introduced in Lohmann et al. (2003), the autoconversion term Q_{autn} is now based on the well evaluated parameterisation of Khairoutdinov and Kogan (2000).

Analogue, the prognostic equation for the ice crystal number concentration (N_i) is given by:

$$\frac{\partial N_i}{\partial t} = R(N_i) + Q_{nuci} - Q_{mlt} + \frac{N_i}{q_i}\left(Q_{frz} + Q_{secp} - Q_{agg} - Q_{saci} - Q_{self} - Q_{sub}\right) \qquad (4.2)$$

where $R(N_i)$ represents the rate of change due to large-scale, turbulent, and convective transport processes. q_i is the ice water content. The microphysical processes are the nucleation of ice crystals Q_{nuci}, melting of ice crystals Q_{mlt}, freezing of cloud droplets Q_{frz}, secondary ice crystal production Q_{secp} , aggregation of ice crystals Q_{agg}, accretion of ice crystals by snow Q_{saci}, self-collection of ice crystals Q_{self}, and sublimation of ice crystals Q_{sub}.

Aerosols affect the cloud microphysics by modulating the nucleation rates of cloud droplets and ice crystals.

4.3.2 Aerosol Cloud Coupling

In the current implementation, only the nucleation of cloud droplets is parameterised in dependency of the aerosol distribution. The ice-crystal formation is derived from the standard ECHAM5 cloud-ice formation rate with a temperature dependent parameterisation of the effective ice-crystal radii (Lohmann, 2002). The implementation of advanced ice-nucleation parameterisations is subject of ongoing research activities.

[1]ETH, Swiss Federal Institute of Technology Zürich, Switzerland
[2]Dalhousie University, Halifax, Canada
[3]Max Planck Institute for Meteorology, Hamburg, Germany

Two alternative parameterisations of the nucleation of liquid cloud droplets from the aerosol distribution have been implemented in ECHAM5-HAM. First, a parameterisation of intermediate complexity that semi-empirically relates the number of available aerosols with the cloud droplet number concentration. Second, an explicit parameterisation of the activation process for an ensemble of log-normal modes.
A key parameter to calculate the aerosol activation is the maximum supersaturation which in turn depends on the updraft velocity. However, the vertical velocity is largely determined by sub-grid scale processes so that it cannot be directly derived from the prognostic variables of global circulation models. Following Lohmann and Kärcher (2002), the total vertical velocity w is parameterised as the sum of the large-scale vertical velocity $\bar{w}$ and a sub-grid scale contribution expressed in terms of the turbulent kinetic energy (TKE):

$$w = \bar{w} + 1.33\sqrt{TKE} \tag{4.3}$$

Semi-Empirical Activation Scheme

The implemented activation scheme of intermediate complexity is based on Lin and Leaitch (1997). Based on measurements obtained during the North Atlantic Regional Experiment (NARE) they empirically determine the constant

$$c = 2.3 \times 10^{-10}\ \mathrm{m^4\,s^{-1}} \tag{4.4}$$

representing aerosol size and composition in the activation parameterisation of Ghan et al. (1993, 1995). The maximum number of activated particles N_{max} is calculated from the number of aerosols N_a by:

$$N_{max} = \frac{N_a w}{w + cN_a} \tag{4.5}$$

N_{max} is further empirically related to the observed average number of activated particles N_{avg} by:

$$N_{avg} = 0.1\ N_{max}^{1.27} \tag{4.6}$$

The measurements of the aerosol number concentration N_a were performed with a Passive Cavity Aerosol Spectrometer Probe (PCASP) with a lower cut-off radius of $r_{cut} = 0.07\ \mu$m (Richard Leaitch, *pers. comm.*). For the implementation in ECHAM5-HAM, the prognosed log-normal aerosol number distribution is integrated over $[r_{cut}, \infty]$ to derive N_a and provide it to the activation scheme to obtain N_{avg} that determines Q_{nuc} in Equation 4.1.

Explicit Activation Scheme

The implemented explicit activation scheme is based on (Abdul-Razzak and Ghan, 2000) and has been applied in a global aerosol model by Ghan et al. (2001a). For a given vertical velocity and an ensemble of log-normal modes i with varying internally-mixed composition, the maximum supersaturation S_{max} is calculated from:

$$S_{max} = \left\{ \sum_i \frac{1}{(\bar{S}^i)^2} \left[f^i \left(\frac{\zeta}{\eta^i} \right)^{\frac{2}{3}} + g^i \left(\frac{(\bar{S}^i)^2}{(\eta^i)^2 + 3\zeta} \right)^{\frac{3}{4}} \right] \right\}^{-\frac{1}{2}} \tag{4.7}$$

where $\bar{S}^i$ is the critical supersaturation for particles with number median radius $\bar{r}^i$. The functions f^i and g^i depend on the mode standard deviation and account for kinetic effects during the

activation. ζ and η^i are functions of the ambient properties, ζ is also a function of the vertical velocity and η^i also a function of the chemical composition of the modes. From the maximum supersaturation, for each mode i the critical radius of activation r^i_{crit} is derived:

$$r^i_{crit} = \bar{r}^i \left(\frac{\bar{S}^i}{S_{max}} \right)^{\frac{2}{3}} \tag{4.8}$$

The total number of activated particles is then calculated by summing the integrals of the log-normal aerosol number distribution for each mode over $[r^i_{crit}, \infty]$ and provided as source term Q_{nuc} in Equation 4.1.

The major limitation of explicit activation schemes is that they require detailed information about the aerosol composition. While the composition is relatively well defined for some aerosol components, such as sea salt, the detailed composition of other components, such as particulate organic matter is insufficiently understood and subject of ongoing research (Kanakidou et al., 2004). In many measurements of aerosol chemical composition, a non-negligible fraction of the aerosol mass cannot be identified (Kanakidou et al., 2004; Putaud et al., 2004). Therefore, although semi-empirical activation schemes are inevitably less accurate for a well defined aerosol system, they are most likely more robust for under-determined aerosol distributions. On this account, the subsequent analysis is based on the semi-empirical Lin and Leaitch (1997) activation approach. A rigorous testing of the explicit Abdul-Razzak and Ghan (2000) approach in ECHAM5-HAM, including improvements of the representation of aerosol chemical composition, is subject of ongoing and future research activities.

4.3.3 Preliminary Results

In the following, preliminary results from a one year integration of ECHAM5-HAM with prognostic cloud-droplet number concentration and the semi-empirical Lin and Leaitch (1997) activation scheme are presented. The simulations are performed in the climate mode of ECHAM5 at a resolution of horizontally T63 in spectral space with a corresponding resolution of $1.8° \times 1.8°$ on a Gaussian grid. The vertical resolution is set to 31 levels, extending from the surface up to 10 hPa. Sea surface temperature and sea ice are prescribed for the year 1980 based on the AMIP II dataset (Taylor et al., 2000). The prescribed emissions of aerosols and precursors are representative for the year 2000 (c.f. 2.2.3), except for the vegetation fires, for which a 1997 to 2000 climatological average of the van der Werf et al. (2003) emission dataset is applied.
The evaluation of the results has a particular focus on the cloud droplet number concentrations and on the cloud droplet effective radii, as they are the key parameters affected by indirect aerosol effects. The annual mean in-cloud cloud-droplet number burden as simulated with ECHAM5-HAM and from the International Satellite Cloud Climatology Project (ISCCP) retrieval of year 1987 AVHRR data (Han et al., 1998) are displayed in Figure 4.4. The high ISCCP cloud droplet burdens over North Africa and the Middle East are most likely an artefact due to the misinterpretation of mineral dust as cloud droplets and the high surface albedo (Han et al., 1998).
The simulated CDNC burdens are generally in good agreement with the ISCCP data. The observed land-sea contrast with higher values over land is well reproduced. Enhanced CDNC levels are found over the polluted continental areas (c.f. illustration of the aerosol optical depth in Figure 2.7). Highest values are simulated over South-East Asia in good agreement with the observations. Plumes with enhanced CDNC levels are clearly discernible in the lee of the

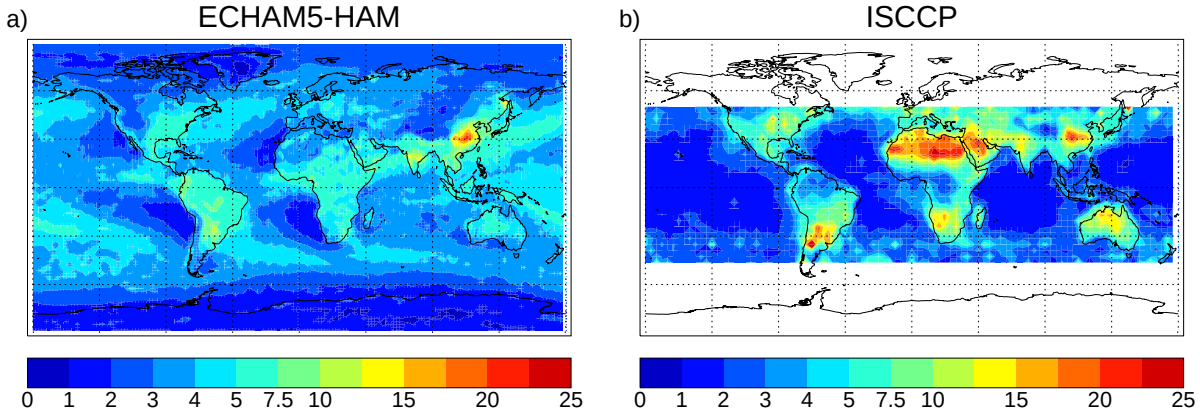

Figure 4.4: Annual-mean in-cloud cloud-droplet number burden [10^6 cm^{-2}] from a) ECHAM4-HAM and b) ISCCP retrieval of year 1987 AVHRR data (Han et al., 1998).

continents. Remote oceanic and clean continental regions show significantly lower values but are regionally higher than in the ISCCP data. This could partly be an effect of shielding of low-level clouds by higher level ice clouds in the ISCCP data. It has to be stressed that the comparison of the climatological simulation with the year 1987 ISCCP data can only give a qualitative picture. Additionally, the ISCCP cloud droplet number burden retrieval is associated with high uncertainties. Nudged simulations for the satellite observation period with concurrent emission data as well as a satellite conform sampling of the model output are necessary requirements for more quantitative conclusions.

The simulated annual mean cloud-droplet effective radius at the cloud top from ECHAM5-HAM and from a POLDER derived satellite composite (Bréon and Colzy, 2000) are displayed in Figure 4.5. Hereby, the ECHAM5-HAM model values are sampled consistently with the POLDER satellite view using the maximum random cloud overlap assumption (based on Quaas et al. (2004)). Only clouds with a liquid fraction of more than 50 % and an optical thickness larger than 0.1 that are not covered by overlying clouds are considered in the ECHAM5-HAM sample. The POLDER data is a composite of the periods 11/1996 - 03/1997 and 04/2003 - 10/2003. The retrieval is limited to cloud-droplets smaller than 16 μm, potentially introducing a low bias. It further requires 150×150 km horizontally homogeneous liquid-clouds so that large areas in the tropics are not covered. It has to be pointed out that the comparison of ECHAM5-HAM simulations in free climate mode with POLDER data representative for specific dates is not fully consistent.

Simulated effective radii agree generally well with the POLDER retrieval but are slightly larger, with the strongest deviation in the regions with low CDNC burdens west of the Americas and of southern Africa. The simulation well reproduces the observed land-sea contrast with lower effective radii over land.

4.4 Conclusions and Outlook

Methods and first applications of the ECHAM5-HAM aerosol model towards the assessment of the aerosol radiative effects were presented.

A measure of aerosol radiative effects was introduced that is applicable consistently for all aerosol radiative effects, including the effects involving feedback processes. This large-scale constrained

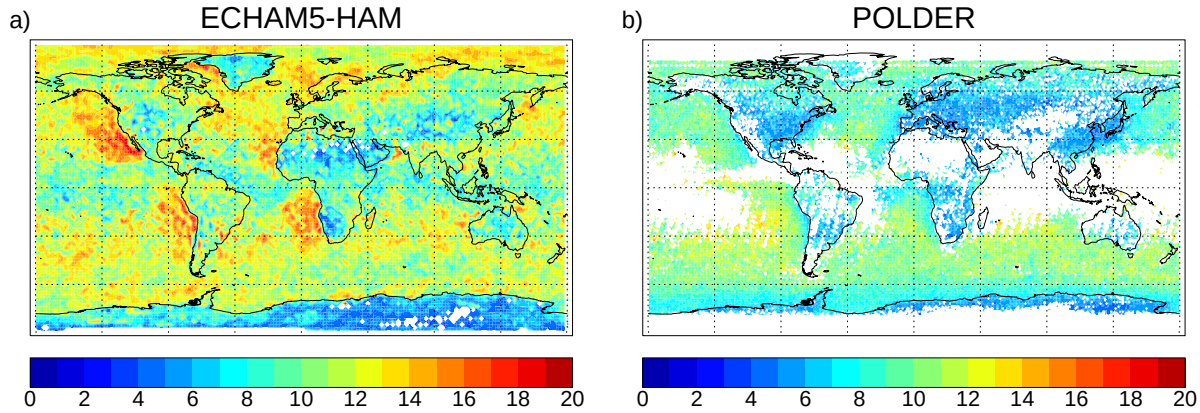

Figure 4.5: Annual-mean cloud droplet effective radius [μ m] at cloud top from a) ECHAM5-HAM sampled with POLDER "view" and b) POLDER composite (Bréon and Colzy, 2000) derived over the periods 11/1996 - 03/1997 and 04/2003 - 10/2003.

aerosol radiative perturbation P_L is similar to the instantaneous forcing on the large-scale but allows for local scale feedbacks. The concept of the large-scale constrained radiative perturbation could easily be extended to include stratospheric adjustment by weakening the relaxation towards the reference meteorology for the stratosphere. The suitability of P_L as first order predictor for the global-mean surface temperature as well as potential scale dependencies require further investigation. However, the demonstrated deviations from additivity (c.f. Chapter 3) generally question the concept of separate first order predictors for individual aerosol components. Further they suggest that advanced integrated global modelling studies are necessary for regional and global estimates of the surface temperature response to changes in the aerosol system.

An analysis of the large-scale aerosol radiative perturbation due to direct and semi-direct aerosol effects was performed exemplary for three anthropogenic perturbations. The global distribution of the radiative perturbations with maxima in the vicinity of the sources illustrates the largely regional extent of the aerosol radiative effects.

The radiative perturbation of carbonaceous emissions from fossil-fuels use and industry is generally positive, indicating the predominance of absorption. The annual global-mean clear-sky radiative perturbation of +0.08 W m^{-2} is enhanced to +0.11 W m^{-2} for the total-sky case, attributable to the enhanced reduction of the planetary albedo of absorbing aerosols due to underlying clouds and the semi-direct aerosol effect. The radiative perturbation of sulfuric emissions from fossil-fuels, industry, and bio-fuels is generally negative, indicating the predominance of scattering. The annual global-mean clear-sky radiative perturbation of -0.69 W m^{-2} is reduced to -0.46 W m^{-2} for the total-sky case, as over and underlying clouds regionally render the increase of the planetary albedo due to aerosol scattering negligible. The total anthropogenic aerosol radiative perturbation, including fossil-fuel and bio-fuel use, industry, and vegetation fires, is negative indicating the predominance of scattering. However, the annual global-mean clear-sky perturbation of -0.49 W m^{-2} is reduced to -0.12 W m^{-2} for the total-sky case. This can be attributed to the dampening of the cooling effect by overlying and underlying clouds and the positive perturbation of absorbing aerosols, clearly discernible in the positive total-sky perturbations of the low-latitude biomass burning regions.

An extended microphysical parameterisation for stratiform clouds, with prognostic treatment of cloud-droplet and ice-crystal number concentrations, was introduced into ECHAM5. Two optional aerosol activation schemes were introduced, coupling the cloud microphysics with the HAM aerosol module. First, a semi-empirical scheme, parameterising the number of activated aerosols in terms of the aerosol number-distribution and the total vertical velocity. The total vertical velocity is derived from the prognostic large-scale and the subgrid-scale vertical velocity parameterised in terms of turbulent kinetic energy. Second, an explicit activation scheme for an ensemble of log-normal modes, parameterising the number of activated aerosols in terms of the aerosol number-distribution, mixing-state, composition, and total vertical velocity.

Results from a preliminary one-year climatological simulation with the semi-empirical activation scheme are presented and evaluated with satellite data. The simulated in-cloud cloud droplet number burdens are in the range of 1 $\times 10^6$ to 20 $\times 10^6$ cm^{-2}, in good agreement with the ISCCP retrieval based on AVHRR data. The distinct observed land sea-contrast with higher CDNC burdens over land is well reproduced. Plumes with enhanced CDNC levels are clearly discernible in the lee of the continents. Simulated cloud-top effective radii, sampled consistently with the POLDER satellite view, reveal a general good agreement with the POLDER retrieved effective radii but are slightly biased high. The observed land-sea contrast with smaller radii over land is captured in the simulations, though less pronounced. In summary, the preliminary evaluation of ECHAM5-HAM with an extended microphysical stratiform cloud scheme and explicit aerosol-cloud coupling shows generally a good agreement with satellite-retrieved remote sensing data. This good agreement of the cloud parameters, despite the large degree of freedom of the fully coupled aerosol-cloud system, provides confidence in the capabilities of the ECHAM5-HAM aerosol-cloud coupling. However, further sensitivity studies and an extensive evaluation are required before quantitative conclusions on the indirect aerosol radiative effects can be drawn.

Current global modelling studies treat only a subset of the relevant aerosol-cloud interactions (Lohmann and Feichter, 2004), so that the total uncertainty of their effects is much higher than the already high uncertainty of the currently accounted effects. While the introduced treatment of aerosol-cloud coupling in ECHAM5-HAM is advanced compared to previous global aerosol-cloud modelling studies suitable for long-term integrations, there is scope for improvements. The development and implementation of advanced parameterisations for ice-nucleation is ongoing. In particular the current limitation of the aerosol-cloud interactions to stratiform clouds is restrictive. However, in standard ECHAM5, as in most global circulation models, the convective cloud parameterisation is based on a mass-flux scheme without explicit treatment of cloud microphysics. Therefore, as basis for a mechanistic calculation of the interaction of aerosols and convective clouds, the convective mass flux scheme of ECHAM5 (Tiedtke, 1989; Nordeng, 1994) has been extended with the microphysical cloud scheme of Lohmann and Roeckner (1996), that is also applied for the stratiform cloud scheme (Zhang et al., 2004). An extension of this implementation to include the prognostic treatment of cloud droplet and ice crystal number concentrations is subject of ongoing research activities and will provide the basis for a consistent treatment of aerosol-cloud interactions for stratiform and convective clouds on the global scale.

Chapter 5

Conclusions and Outlook

5.1 Conclusions

Aerosols play an important role in the global climate system. However, their effects on the radiation budget and even their global distribution and composition are not understood satisfactorily. The primary objective of this study is to advance the understanding about the global tropospheric aerosol system as basis for higher accuracy estimates of the anthropogenic aerosol effects. The inherent complexity and the large spatio-temporal inhomogeneity of the global aerosol system render the assessment of the aerosol effects, and in particular their anthropogenic contribution, challenging. Observations, in-situ and remote sensing, provide fundamental information on the aerosol system. However, remote sensing as the only measurement with a global coverage, is limited by the fact that the anthropogenic signal is per se not distinguishable from the natural signal. This was the main rationale for the choice of a global aerosol modelling approach to address the objective of this study.

The traditional global aerosol models suitable for climate studies are based on a bulk mass approach without prognostic treatment of the aerosol size-distribution and mixing-state. However, these parameters are fundamental for the calculation of all climate relevant processes and are therefore fixedly prescribed in these models. In reality, measurements reveal their large spatio-temporal variability. Measurements additionally provide cogent indications for an anthropogenic influence on the aerosol mixing-state and size-distribution. Therefore, the general assumption that these fixed parameters are applicable in different climate regimes under different emission levels is not justified.

To overcome this deficiencies, the global aerosol-climate model ECHAM5-HAM (Stier et al., 2004) has been developed. In the aerosol module HAM, the aerosol distribution is represented by an ensemble of interacting internally and externally-mixed log-normal aerosol modes. Aerosol size-distribution, mixing-state, and composition are described by prognostic variables. This quasi-realistic aerosol representation provides the basis of a mechanistic coupling with the other components of the earth system. The sink processes as well as the aerosol radiative properties for each mode are calculated consistently in dependence of size and composition. In the current configuration, the components sulfate, black carbon, particulate organic matter, sea salt, and mineral dust are included. The aerosol module HAM includes the processes gas- and liquid phase sulfur chemistry, the sink processes dry deposition, sedimentation, and wet deposition, a module for the calculation of the aerosol radiative properties, and the microphysical core M7. M7 considers the processes coagulation, condensation on pre-existing aerosols, aerosol nucleation, thermodynamical equilibrium with water vapour, and the inter-modal transfer. The emissions of

mineral dust, sea salt and maritime DMS are calculated online. Despite the advanced complexity of ECHAM5-HAM, the computational efficiency allows the application in long-term climate studies.
The ECHAM5-HAM simulated global aerosol system is generally in good agreement with available observations. Simulated global annual-mean column burdens (lifetimes) for the year 2000 are for sulfate 0.80 Tg(S) (3.9 days), black carbon 0.11 Tg (5.4 days), particulate organic matter 0.99 Tg (5.4 days), sea salt 10.5 Tg (0.8 days), and mineral dust 8.28 Tg (4.6 days), lying in the range of previous estimates. The evaluation of the simulated surface mass concentrations with in-situ surface measurements shows generally a good agreement, with larger deviations for mineral dust. An evaluation of the simulated number concentrations with campaign-composite aircraft measurements from three measurement campaigns, confirms at large the capability to reproduce observed vertical profiles of the number concentrations for a range of conditions. The simulated global average of aerosol optical depth is with 0.14 in very good agreement with current estimates from remote sensing products, such as 0.14 from an AERONET sun-photometer network derived global average, and 0.16 from a MODIS-MISR satellite composite. The global distribution of the aerosol optical depth agrees well with satellite observations, with non-negligible regional differences.

It has been demonstrated, that the introduced ECHAM5-HAM aerosol model is, albeit the increased degrees of freedom, capable to simulate the fundamental characteristics of the global aerosol system. This provides the basis for the analysis of the limitations of the inherent assumptions in the traditional approach for the assessment of the aerosol radiative effects. The internal dynamics of the aerosol system as a response to anthropogenic disturbances, imposed in form of emission changes, has been investigated with the following key findings:

- Changes in anthropogenic emissions affect the microphysical aging capacity of the atmosphere. Changes in the aging capacity, in turn, non-linearly affect the aerosol life-times, global distributions, and radiative effects.

- The changes in aerosol numbers and radiative effects, as response to emission changes, deviate from additivity. These exposed deviations from additivity challenge the radiative forcing concept applied in IPCC (2001) for the assessment of the aerosol radiative effects.

- Aerosol numbers respond non-linearly to changes in anthropogenic emissions. Carbonaceous emissions disproportionately contribute to the radiatively important accumulation mode number burden, particularly close to the source regions. In contrast, anthropogenic sulfuric emissions less than proportionally contribute to the accumulation mode number burden close to the source regions and disproportionately contribute in remote regions.

- The anthropogenic impact on the microphysical aging capacity modulates the long-distance transport of aerosols. Reductions of anthropogenic sulfur emissions increase the high-latitude concentrations and associated deposition rates of black carbon, particulate organic matter, and mineral dust. This has important implications:

  - For the interpretation of ice core data, the aerosol concentration in ice-cores is generally assumed a linear proxy for the atmospheric aerosol load. However, it has been shown that the omission of anthropogenic sulfur emissions increased the zonal-mean northern high-latitude deposition rate of mineral dust by 20 % while the global aerosol

load was only increased by 1.5 %. Thus, a linear derivation of the atmospheric aerosol load from ice-core aerosol concentrations seems inappropriate.

– Due to the omission of anthropogenic sulfuric emissions, the zonal-mean black-carbon deposition at northern high-latitudes increased even by of up to 140 %. This region is prone to changes in the surface albedo and ice feedbacks. It has been proposed that black carbon deposition on snow and ice exerts a significant positive climate forcing (Hansen and Nazarenko, 2004). This effect could be amplified by enhanced deposition of black carbon due to mitigation of sulfuric aerosol precursors.

In summary, the analysis of the response of the aerosol system to changes in anthropogenic emissions revealed significant non-linearities and deviations from additivity, accompanied by a microphysical coupling of the aerosol cycles. The potential climate implications are manifold. The majority of the underlying processes can not be accounted for in the traditional bulk aerosol modelling approach. Further studies with advanced global aerosol models are required to reduce the uncertainties associated with these non-linearities and to constrain the impacts on the aerosol radiative effects.

The demonstrated deviations from additivity indicate that the sum of individual radiative disturbances is not representative for the total radiative disturbance. Integrated advanced modelling studies are required to assess the individual anthropogenic effects on the total radiative disturbance. Nonetheless, a first order measure of the individual radiative effects is desirable. The established measure for radiative disturbances in the climate system, radiative forcing, is strictly limited to external perturbations. However, beside the semi-direct and the indirect cloud-lifetime effect, it has been demonstrated in Chapter 3 that also the aerosol system itself is characterised by internal microphysical interactions and feedbacks, violating the definition as external perturbation. The large-scale constrained radiative perturbation has been introduced as first order measure of the aerosol radiative perturbation, applicable consistently to all aerosol radiative effects:

- The large-scale constrained radiative perturbation of the surface-troposphere system due to the omission of a perturbation or agent is the change in net irradiance at the top of the atmosphere in two simulations in one of which the perturbation or agent is omitted, with the sea surface temperature and large-scale dynamical state held fixed at the unperturbed values.

First applications of ECHAM5-HAM towards the assessment of the direct and semi-direct aerosol radiative effects have been presented. The global distribution of the large-scale constrained aerosol radiative perturbations with maxima in the vicinity of the sources illustrates the largely regional extent of the aerosol radiative effects. The total anthropogenic radiative perturbation, including fossil-fuel and bio-fuel use, industry, and vegetation fires, is negative, indicating the predominance of scattering. However, the annual global-mean clear-sky perturbation of -0.49 $\mathrm{W\,m^{-2}}$ is reduced to -0.12 $\mathrm{W\,m^{-2}}$ for the total sky case. This can be attributed to the following effects. First, overlying and underlying clouds regionally render the negative contribution of the increase of the planetary albedo due to aerosol scattering negligible. Second, absorbing aerosols over clouds reducing their high albedo as well as the semi-direct aerosol effect introduce positive radiative perturbations.

The coupling of the aerosol cycle and the hydrological cycle is an essential step towards a comprehensive assessment of the aerosol radiative effects. As basis, an extended microphysical parameterisation for stratiform clouds, with prognostic treatment of cloud-droplet and ice-crystal number concentrations, has been introduced into ECHAM5. The cloud microphysics has been coupled to the aerosol system via two optional aerosol activation schemes, a semi-empirical scheme and an explicit activation scheme.
The simulated cloud parameters from a preliminary one-year climatological simulation with the semi-empirical activation scheme were evaluated with satellite retrieved datasets. In-cloud cloud droplet number burdens are in good agreement with the International Satellite Cloud Climatology Project retrieval based on AVHRR satellite data. The observed distinct land sea-contrast with higher cloud droplet burdens over land is well reproduced. Simulated cloud-top effective radii, sampled consistently with the POLDER satellite view, reveal a general good agreement with the POLDER retrieved effective radii but are slightly biased high. The observed land-sea contrast with smaller radii over land is captured in the simulations, though less pronounced. It has to be pointed out that these satellite-retrievals, in particular of the cloud droplet number burden, are associated with high uncertainties.
Nonetheless, this general good performance of ECHAM5-HAM, despite the large degree of freedom of the fully coupled aerosol-cloud system, provides confidence in the capabilities of the aerosol-cloud coupling. However, further sensitivity studies and an extensive evaluation are required before quantitative conclusions on the indirect aerosol radiative effects can be drawn.

5.2 Outlook

It has been demonstrated that the ECHAM5-HAM aerosol-climate model has the capability to simulate the fundamental properties of the global aerosol system while providing extensive degrees of freedom. This allows the application in a wide range of climate regimes. Further investigations of the climate impact of aerosols and the internal dynamics of the aerosol system will be performed with a particular focus on the additivity of the aerosol radiative effects.

The advanced aerosol representation of HAM establishes the basis for a mechanistic coupling with the other components of the earth system. In the framework of the emerging Max Planck Institute Earth System Model, the aerosol module HAM has been interactively coupled to the following sub-models: the atmospheric general circulation model ECHAM5, the ocean general circulation model MPI-OM, the surface and vegetation model JSBACH, the atmospheric chemistry model MOZECH, and the ocean biogeochemistry model HAMOCC. Initially, the effect of aerosols on the hydrological cycle and the radiative fluxes are interacting with the atmosphere-ocean-land system. Emissions of dimethyl sulfide from the ocean biogeochemistry are integrated in the sulfur cycle and the deposition of mineral dust acts as micro-nutrient for the marine biosphere. The aerosol system is coupled to the atmospheric chemistry with an explicit consideration in the calculation of the photolysis rates. Numerous enhanced linkages between the compartments of the earth system model, such as heterogeneous chemistry or the interaction of the terrestrial biosphere and the land-surface emissions, are subject of ongoing research.
Long-term transient climate simulations with the fully coupled earth system model are ongoing and will allow to gain deep insights in the anthropogenic contribution to climate change and the internal dynamics of the complex earth system. The coupling with the marine biosphere allows to investigate the proposed CLAW (Charlson et al., 1987) feedback cycle between the marine

biosphere, sulfate aerosols, and the hydrological cycle.
Based on the established coupling of aerosols and the hydrological cycle, the indirect aerosol effects will be scrutinised. The implemented aerosol activation schemes will be compared and further evaluated. Advanced parameterisations for ice nucleation are being integrated into ECHAM5-HAM. The convective cloud scheme has been extended by a cloud microphysical scheme that is being extended with the prognostic treatment of cloud droplet and ice crystal number concentrations. These developments provide the basis for a consistent analysis of aerosol-cloud interactions for stratiform and convective clouds on the global scale.
In the framework of the EU project PHOENICS, an extended thermodynamical module is being coupled with the aerosol microphysical core M7 and will be merged into the HAM aerosol module. This development will, together with the MOZECH chemistry module, establish the basis for the inclusion of the currently neglected nitrate/ammonium system and considerably improve the accuracy of the aerosol water uptake calculations. Also within PHOENICS, a condensed version of a comprehensive secondary organic aerosol model, suitable for the inclusion into HAM, is in development.

The inherent complexity of the aerosol system gives rise to uncertainties that can only be partly diminished with individual global modelling studies.
A multi-scale approach, synthesising the individual strengths of a hierarchy of models from the molecular scale to the global scale, appears promising for the aerosol model improvement. Small-scale models allow the application of more explicit process representation and a better evaluation with laboratory and in-situ measurements. They can be utilised to derive and enhance parameterisations applicable to the larger scales. In turn, large-scale models can provide realistic boundary conditions for small-scale process studies.
On the global scale, an integrated approach, constraining and evaluating multiple global model results with the available observational data is the way forward to reduce the remaining uncertainties. Therefore, the ECHAM5-HAM aerosol climate model is participating in the international global aerosol model intercomparison AEROCOM in which results from the majority of the state of the art global aerosol models and the latest observational data are integrated to advance the understanding about the global aerosol system.

Bibliography

Abdul-Razzak, H. and Ghan, S. J.: A parameterization of aerosol activation 2. Multiple aerosol types, J. Geophys. Res., 105, 6837–6844, 2000.

Adams, P. J. and Seinfeld, J. H.: Predicting global aerosol size distributions in general circulation models, J. Geophys. Res., 107, 4370, doi:10.1029/2001JD001 010, 2002.

Adams, P. J., Seinfeld, J. H., and Koch, D. M.: Global concentrations of tropospheric sulfate, nitrate, and ammonium aerosol simulated in a general circulation model, J. Geophys. Res., 104, 13 791–13 824, 1999.

Albrecht, B. A.: Aerosols, cloud microphysics, and fractional cloudiness, Science, 245, 1227–1230, 1989.

Andreae, M. and Crutzen, P.: Atmospheric aerosols: biogeochemical sources and role in atmospheric chemistry, Science, 276, 1052–1058, 1997.

Andreae, M. O., Rosenfeld, D., Artaxo, P., Costa, A. A., Frank, G. P., Longo, K. M., and Silva-Diass, M. A. F.: Smoking rain clouds over the Amazon, Science, 303, 1337–1342, 2004.

Andres, R. J. and Kasgnoc, A. D.: A time-averaged inventory of subaerial volcanic sulfur emissions, J. Geophys. Res., 103, 25 251–25 261, 1998.

Ångström, A.: Atmospheric turbidity, global illumination and planetary albedo of the earth, Tellus, 14, 435–450, 1962.

Arnold, F.: Ion nucleation - a potential source for stratospheric aerosols, Nature, 299, 134–137, 1982.

Bagnold, R. A.: The physics of blown sand and desert dunes, Methuen, New York, 265 pp., 1941.

Balkanski, Y., Schulz, M., Claquin, T., Moulin, C., and Ginoux, P.: Emission of Atmospheric Trace Compounds, chap. Global emissions of mineral aerosol: formulation and validation using satellite imagery, pp. 239–267, Ed. Kluwer, 2004.

Bates, T. S., Huebert, B. J., Gras, J. L., Griffiths, F. B., and Durkee, P. A.: International Global Atmospheric Chemistry (IGAC) project's first Aerosol Characterisation Experiment (ACE 1): overview., J. Geophys. Res., 103, 16 297–16 318, 1998.

Blanchard, C. and Syzdek, L.: Mechanism for water-to-air transfer and concentration of bacteria, Science, 170, 626–628, 1970.

Bond, T. C., Streets, D. G., Yarber, K. F., Nelson, S. M., Woo, J.-H., and Klimont, Z.: A technology-based global inventory of black and organic carbon emissions from combustion, J. Geophys. Res., 109, D14 203, doi:10.1029/2003JD003 697, 2004.

Boucher, O. and Haywood, J.: On summing the components of radiative forcing of climate change, Clim. Dyn., 18, 297–302, 2001.

Boucher, O. and Lohmann, U.: The sulfate-CCN-cloud albedo effect, a sensitivity study with two general circulation models, Tellus, Ser. B, 47, 281–300, 1995.

Boucher, O., Venkataraman, C., Sciare, J., Reddy, M. S., Pham, M., Lawrence, M. G., vonKuhlmann, R., Cosme, E., Bopp, L., Aumont, O., Belviso, S., and Moulin, C.: DMS atmospheric concentrations and sulphate aerosol indirect radiative forcing: a sensitivity study to the DMS source representation and oxidation, Atm. Chem. Phys., 3, 49–65, 2003.

Bower, K. and Choularton, T.: Cloud processing of the cloud condensation nucleus spectrum and its climatological consequences, Q. J. R. Meteorol. Soc., 119, 655–679, 1993.

Brasseur, G. P., Prinn, R. G., and Pszenny, A. A., eds.: Atmospheric Chemistry in a Changing World, Global Change - The IGBP Series, Springer, Berlin, 300 pp., 2003.

Bréon, F.-M. and Colzy, S.: Global distribution of cloud droplet effective radius from POLDER polarization measurements, GRL, 27, 4065–4068, 2000.

Carney, J., Schnell, R., and Carty, C.: Active ice nuclei associated with viable bacteria in nova-scotia marine fogs, Transactions-American Geophysical Union, 56, 994–994, 1975.

Charlson, R., Lovelock, J., Andreae, M., and Warren, S.: Oceanic phytoplankton, atmospheric sulphur, cloud albedo and climate, Nature, 326, 655–661, 1987.

Chin, M., Jacob, D. J., Gardner, G. M., Foreman-Fowler, M. S., Spiro, P. A., and Savoie, D. L.: A global three-dimensional model of tropospheric sulfate, J. Geophys. Res., 101, 18 667–18 690, 1996.

Chin, M., Rood, R. B., Lin, S., Mller, J., and Thompson, A. M.: Atmospheric sulfur cycle simulated in the global model GOCART: Model description and global properties, J. Geophys. Res., 105, 24 671–24 688, 2000.

Chin, M., Ginoux, P., Kinne, S., Torres, O., Holben, B. N., Duncan, B. N., Martin, R. V., Logan, J. A., Higurashi, A., and Nakajima, T.: Tropospheric aerosol optical thickness from the GOCART model and comparisons with satellite and Sun photometer measurements, J. Atmos. Sci., 59, 461–483, 2002.

Christopher, S. A. and Zhang, J.: Cloud-free shortwave aerosol radiative effect over oceans: Strategies for identifying anthropogenic forcing from Terra satellite measurements, Geophys. Res. Lett., 31, L18 101, doi:10.1029/2004GL020 510, 2004.

Chu, D. A., Kaufman, Y. J., Ichoku, C., Remer, L. A., Tanré, D., and Holben, B. N.: Validation of MODIS aerosol optical depth retrieval over land, Geophys. Res. Lett., 29, 8007, doi:10.1029/2001GL013 205, 2002.

Chung, S. H. and Seinfeld, J. H.: Global distribution and climate forcing of carbonaceous aerosols, J. Geophys. Res., 107, 4407, doi:10.1029/2001JD001 397, 2002.

Claquin, T.: Modeling of the mineralogy and the radiative forcing of desert dust, Ph.D. thesis, Paris University, Paris, France, 1999.

Cofala, J., Amann, M., and Mechler, R.: Scenarios of world anthropogenic emissions of air pollutants and methane up to 2030, Tech. rep., International Institute for Applied Systems Analysis (IIASA), Laxenburg, Austria, available from: http://www.iiasa.ac.at/rains/global_emiss/global_emiss.html, 2005.

Cooke, W. F. and Wilson, J. J. N.: A global black carbon aerosol model, J. Geophys. Res., 101, 19 395–19 410, doi:10.1029/96JD00671, 1996.

Cooke, W. F., Koffi, B., and Gregoire, J.-M.: Seasonality of vegetation fires in Africa from remote sensing data and application to a global chemistry model, J. Geophys. Res., 101, 21 051–21 065, 1996.

Cooke, W. F., Liousse, C., Cachier, H., and Feichter, J.: Construction of a 1° x 1° fossil fuel emission data set for carbonaceous aerosol and implimentation and radiative impact in the ECHAM4 model, J. Geophys. Res., 104, 22 137–22 162, 1999.

Crutzen, P.: Nucleation of atmospheric aerosols, chap. The role of particulate matter in ozone photochemistry, pp. 268–270, Elsevier, 1996.

Dentener, F. and Crutzen, P.: Reaction of N_2O_5 on tropospheric aerosols - impact on the global distributions of NO_X, O_3, and OH, J. Geophys. Res., 98, 7149 – 7163, 1993.

Dickinson, R. E.: Carbon Dioxide Review, pp. 101–133, Clarendon, New York, NY, USA, 1982.

Dockery, D. W., Pope, A. C., Xu, X., Spengler, J. D., Ware, J. H., Fay, M. E., Ferris, B. G., and Speizer, F. E.: An association between air pollution and mortality in six U.S. cities, The New England Journal of Medicine, 329, 1753–1759, 1993.

Downing, H. D. and Williams, D.: Optical-constants of water in infrared, J. Geophys. Res., 80, 1656–1661, 1975.

Dubovik, O. and King, M. D.: A flexible inversion algorithm for retrieval of aerosol optical properties from sun and sky radiance measurements, J. Geophys. Res., 105, 20 673–20 696, 2000.

EC: Directive 199/30EC relating to limit values for sulphur dioxide, oxides of nitrogen, particulate matter and lead in air, J. Europ. Commun., L 163, 41–60, 1999.

Emmons, L. K., Hess, P., Klonecki, A., Tie, X., Horowitz, L., Lamarque, J. F., Kinnison, D., Brasseur, G. P., Atlas, E., Browell, E., Cantrell, C., Eisele, F., Mauldin, R. L., Merrill, J., Ridley, B., and Shetter, R.: Budget of tropospheric ozone during TOPSE from two chemical transport models, J. Geophys. Res., 108, 8372, doi:10.1029/2002JD002 665, 2003.

Feichter, J., Kjellström, E., Rodhe, H., Dentener, F., Lelieveld, J., and Roelofs, G.-J.: Simulation of the tropospheric sulfur cycle in a global climate model, Atmos. Environ., 30, 1693–1707, 1996.

Feichter, J., Roeckner, E., Lohmann, U., and Liepert, B.: Nonlinear aspects of the climate response to greenhouse gas and aerosol forcing, J. Clim., 17, 2384–2398, 2004.

Flossmann, A., Hall, W., and Pruppacher, H.: A theoretical-study of the wet removal of atmospheric pollutants. 1. The redistribution of aerosol-particles captured through nucleation and impaction scavenging by growing cloud drops, Journal Of The Atmospheric Sciences, 42, 583–606, 1985.

Fouquart, Y. and Bonnel, B.: Computations of solar heating of the earth's atmosphere: A new parameterization, Beitr. Phys. Atmos., 53, 35–62, 1980.

Fuchs, N. A.: Evaporation and droplet growth in gaseous media, Pergamon, Tarrytown, New York, 72 pp., 1959.

Fuchs, N. A.: The mechanics of aerosols, Pergamon Press, Oxford, 1964.

Gallagher, M. W., Nemitz, E., Dorsey, J. R., Fowler, D., Sutton, M. A., and andand J. Duyzer, M. F.: Measurements and parameterizations of small aerosol deposition velocities to grassland, arable crops, and forest: Influence of surface roughness length on deposition, J. Geophys. Res., 107, 4154, doi:10.1029/2001JD000 817, 2002.

Ganzeveld, L. and Lelieveld, J.: Dry deposition parameterization in a chemistry general circulation model and its influence on the distribution of reactive trace gases, J. Geophys. Res., 100, 20 999–21 012, 1995.

Ganzeveld, L., Lelieveld, J., and Roelofs, G.-J.: Dry deposition parameterization of sulfur oxides in a chemistry and general circulation model, J. Geophys. Res., 103, 5679–5694, 1998.

Ghan, S., Chuang, C., and Penner, J.: A parameterization of cloud droplet nucleation. Part I: single aerosol type, Atmos. Res., 30, 198–221, 1993.

Ghan, S., Chuang, C., Easter, R., and Penner, J.: A parameterization of cloud droplet nucleation. Part II: multiple aerosol types, Atmos. Res., 36, 39–54, 1995.

Ghan, S., Laulainen, N., Easter, R., Wagener, R., Nemesure, S., Chapman, E., and Leung, Y. Z. R.: Evaluation of aerosol direct radiative forcing in MIRAGE, J. Geophys. Res., 106, 5295–5316, 2001a.

Ghan, S. J., Easter, R. C., Hudson, J., and Brèon, F.-M.: Evaluation of aerosol indirect radiative forcing in MIRAGE, J. Geophys. Res., 106, 5317–5334, 2001b.

Gilgen, H., Wild, M., and Ohmura, A.: Means and trends of shortwave irradiance at the surface estimated from global energy balance archive data, J. Clim., 11, 2042–2061, 1998.

Ginoux, P., Chin, M., Tegen, I., Prospero, J. M., Holben, B., Dubovik, O., and Lin, S.-J.: Sources and distributions of dust aerosols simulated with the GOCART model, J. Geophys. Res., 106, 20 255–20 274, 2001.

Gong, S. L., Barrie, L. A., and Lazare, M.: Canadian Aerosol Module (CAM): A size-segregated simulation of atmospheric aerosol processes for climate and air quality models 2. Global sea-salt aerosol and its budgets, J. Geophys. Res., 107, 4779, doi:10.1029/2001JD002 004, 2002.

Gong, S. L., Barrie, L. A., Blanchet, J. P., K. von Salzen, U. L., Lesins, G., Spacek, L., Zhang, L. M., Girard, E., Lin, H., Leaitch, R., Leighton, H., Chylek, P., and Huang, P.: Canadian Aerosol Module: A size-segregated simulation of atmospheric aerosol processes for climate and air quality models - 1. Module development, J. Geophys. Res., 108, 4007, doi:10.1029/2002JD002 633, 2003.

Graf, H.-F., Feichter, J., and Langmann, B.: Volcanic sulfur emissions: Estimates of source strength and its contribution to the global sulfate distribution, J. Geophys. Res., 102, 10 727–10 738, 1997.

Graßl, H.: Albedo reduction and radiative heating of clouds by absorbing aerosol particles, Contributions Atmospheric Physics, 48, 199–210, 1975.

Guelle, W., Schulz, M., Balkanski, Y., and Dentener, F.: Influence of the source formulation on modeling the atmospheric global distribution of sea salt aerosol, J. Geophys. Res., 106, 27 509–27 524, 2001.

Guenther, A., Hewitt, C. N., Erickson, D., Fall, R., Geron, C., Graedel, T., Harley, P., Klinger, L., Lerdau, M., McKay, W. A., Pierce, T., Scholes, B., Steinbrecher, R., Tallamraju, R., Taylor, J., , and Zimmerman, P.: A global model of natural volatile organic compound emissions, J. Geophys. Res., 100, 8873–8892, 1995.

Gutman, G., Tarpley, D., Ignatov, A., and Olson, S.: The enhanced NOAA global land dataset from Advanced Very High Resolution Radiometer, Bull. Am. Meteorol. Soc., 76, 1141–1156, 1995.

Halmer, M. M., Schmincke, H.-U., and Graf, H.-F.: The annual volcanic gas input into the atmosphere, in particular into the stratosphere: a global data set for the past 100 years, Journal of Volcanology and Geothermal Research, 115, 511–528, 2002.

Han, Q., Rossow, W. B., Chou, J., and Welch, R. M.: Global variation of column droplet concentration in low-level clouds, Geophys. Res. Lett., 25, 1419–1422, 1998.

Hansen, J., Sato, M., and Ruedy, R.: Radiative forcing and climate response, J. Geophys. Res., 102, 6831–6864, 1997.

Hansen, J., Sato, M., Nazarenko, L., Ruedy, R., Lacis, A., Koch, D., Tegen, I., Hall, T., Shindell, D., Santer, B., Stone, P., Novakov, T., Thomason, L., Wang, R., Wang, Y., Jacob, D., Hollandsworth, S., Bishop, L., Logan, J., Thompson, A., Stolarski, R., Lean, J., Willson, R., Levitus, S., Antonov, J., Rayner, N., Parker, D., and Christy, J.: Climate forcings in Goddard Institute for Space Studies SI2000 simulations, J. Geophys. Res., 107, 4347, doi:10.1029/2001JD001 143, 2002.

Hansen, J. E. and Nazarenko, L.: Soot climate forcing via snow and ice albedos, Proc. Natl. Acad. Sci., 101, 423–428, doi:10.1073/pnas.2237157100, 2004.

Haywood, J. M., Ramaswamy, V., and Donner, L. J.: A limited-area-model case study of the effects of sub-grid scale variations in relative humidity and cloud upon the direct radiative forcing of sulfate aerosol, Geophys. Res. Lett., 24, 143–146, 1997a.

Haywood, J. M., Roberts, D. L., Slingo, A., Edwards, J. M., and Shine, K. P.: General circulation model calculations of the direct radiative forcing by anthropogenic sulfate and fossil-fuel soot aerosol, J. Clim., 10, 1562–1577, 1997b.

Heintzenberg, J., Raes, F., Schwartz, S., Ackermann, I., Artaxo, P., Bates, T., Benkovitz, C., Bigg, K., Bond, T., Brenguier, J., Eisele, F., Feichter, J., Flossmann, A., Fuzzi, S., Graf, H., Hales, J., Herrmann, H., Hoffmann, T., Huebert, B., Husar, R., Jaenicke, R., Kärcher, B., Kaufman, Y., Kent, G., Kulmala, M., Leck, C., Liousse, C., Lohmann, U., Marticorena, B., Mcmurry, P., Noone, K., Dowd, C., Penner, J., Pszenny, A., Putaud, J., Quinn, P., Schurath, U., Seinfeld, J., Sievering, H., Snider, J., Sokolik, I., Stratmann, F., Dingenen, R. V., Westphal, D., Wexler, A., Wiedensohler, A., Winkler, D., and Wilson, J.: Atmospheric Chemistry in a Changing World. An Integration and Synthesis of a Decade of Tropospheric Chemistry Research, chap. Tropospheric Aerosols, pp. 125–156, Global Change - The IGBP Series, Springer, Berlin Heidelberg New York, 2003.

Henning, S., Bojinski, S., Diehl, K., Ghan, S., Nyeki, S., Weingartner, E., Wurzler, S., , and Baltensperger, U.: Aerosol partitioning in natural mixed-phase clouds, Geophys. Res. Lett., 31, L06 101, doi:10.1029/2003GL019 025, 2004.

Hess, M., Koepke, P., and Schult, I.: Optical properties of aerosols and clouds: The software package OPAC, Bull. Am. Meteorol. Soc., 79, 831–844, 1998.

Hicks, B. B., Boldocchini, D. D., Meyers, T. P., Hosker, R. P., and Matt, D. R.: A preliminary multiple resistance routine for deriving dry deposition velocities from measured quantities, Water, Air, Soil Pollut., 36, 311–330, 1987.

Holben, B. N., Tanré, D., Smirnov, A., Eck, T. F., Slutsker, I., Abuhassan, N., Newcomb, W. W., Schafer, J. S., Chatenet, B., Lavenu, F., Kaufman, Y. J., Castle, J. V., Setzer, A., Markham, B., Frouin, D. C. R., Halthore, R., Karneli, A., O'Neill, N. T., Pietras, C., Pinker, R. T., Voss, K., and Zibordi, G.: An emerging ground-based aerosol climatology: Aerosol optical depth from AERONET, J. Geophys. Res., 106, 12 067–12 098, 2001.

Hoppel, W., Frick, G., Fitzgerald, J., and Larson, R.: Marine boundary-layer measurements of new particle formation and the effects nonprecipitating clouds have on aerosol-size distribution, J. Geophys. Res., 99, 14 443–14 459, 1994.

Horowitz, L. W., Walters, S., Mauzerall, D. L., Emmons, L. K., Rasch, P. J., Granier, C., Tie, X., Lamarque, J.-F., Schultz, M. G., Tyndall, G. S., Orlando, J. J., and Brasseur, G. P.: A global simulation of tropospheric ozone and related tracers: Description and evaluation of MOZART, version 22, J. Geophys. Res., 108, 4784, doi:10.1029/2002JD002 853, 2003.

Houghton, J. T., Filho, L. G. M., Bruce, J., Lee, H., Callender, B. A., Haites, E., Harris, N., and Maskell, K., eds.: Climate change 1994, chap. Radiative Forcing of Climate Change and an Evalutation of the IPCC IS92 Emission Scenarios, Cambridge University Press, 339 pp., 1994.

Hsu, N. C., Herman, J. R., Torres, O., Holben, B. N., Tanre, D., Eck, T. F., Smirnov, A., Chatenet, B., and Lavenu, F.: Comparisons of the TOMS aerosol index with Sun-photometer aerosol optical thickness: Results and applications, J. Geophys. Res., 104, 6269–6280, 1999.

Hummelshøj, P., Jensen, N. O., and Larsen, S. E.: Particle dry deposition to a sea surface, pp. 829–840, Precipitation scavenging and atmosphere-surface exchange, Hemisphere Publishing Corporation, Washington, 1992.

IPCC: Climate change 2001: The scientific basis, Cambridge University Press, 881 pp., 2001.

Jacobson, M. Z.: A physically-based treatment of elemental carbon optics: Implications for global direct forcing of aerosols, Geophys. Res. Lett., 27, 217–220, 2000.

Jacobson, M. Z.: GATOR-GCMM: A global- through urban-scale air pollution and weather forecast model, 1. Model design and treatment of subgrid soil, vegetation, roads, rooftops, water, sea ice, and snow, J. Geophys. Res., 106, 5385–5402, 2001a.

Jacobson, M. Z.: Global direct radiative forcing due to multicomponent anthropogenic and natural aerosols, J. Geophys. Res., 106, 1551–1568, doi:10.1029/2000JD900514, 2001b.

Jacobson, M. Z., Tabazadeh, A., and Turco, R. P.: Simulating equilibrium within aerosols and nonequilibrium between gases and aerosols, J. Geophys. Res., 101, 9079–9091, 1996.

Jaenicke, R. and Matthias-Maser, S.: The direct contribution of the biosphere to the atmospheric aerosol, J. Aerosol Sci., 24, S537–S538, 1993.

Jeuken, A. B. M., Siegmund, P. C., Heijboer, L. C., Feichter, J., and Bengtsson, L.: On the potential of assimilating meteorological analyses in a global climate model for the purpose of model validation, J. Geophys. Res., 101, 16 939–16 950, doi:10.1029/96JD01218, 1996.

Johnson, K., Gordon, R., and Coale, K.: What controls dissolved iron concentrations in the world ocean?, Marine Chemistry, 57, 137–161, 1997.

Kanakidou, M., Seinfeld, J. H., Pandis, S. N., Barnes, I., Dentener, F. J., Facchini, M. C., van Dingenen, R., Ervens, B., Nenes, A., Nielsen, C. J., Swietlicki, E., Putaud, J. P., Balkanski, Y., Fuzzi, S., Horth, J., Moortgat, G. K., Winterhalter, R., Myhre, C. E. L., Tsigaridis, K., Vignati, E., Stephanou, E. G., and Wilson, J.: Organic aerosol and global climate modelling: a review, Atm. Chem. Phys. Discuss., 4, 5855–6024, 2004.

Kaufman, Y. J., Tanré, D., Remer, L. A., Vermote, E. F., Chu, A., and Holben, B. N.: Operational remote sensing of tropospheric aerosol over land from EOS moderate resolution imaging spectroradiometer, J. Geophys. Res., 102, 17 051–17 068, 1997.

Kettle, A. and Andreae, M.: Flux of the dimethylsulfide from the oceans: A comparison of updated data sets and flux models, J. Geophys. Res., 105, 26 793–26 808, 2000.

Khain, A., Rosenfeld, D., and Pokrovsky, A.: Simulating convective clouds with sustained supercooled liquid water down to -37.5 degrees C using a spectral microphysics model, Geophys. Res. Lett., 28, 3887–3890, 2001.

Khairoutdinov, M. and Kogan, Y.: A New Cloud Physics Parameterization in a Large-Eddy Simulation Model of Marine Stratocumulus, Mon. Wea. Rev., 128, 229–243, 2000.

Kinne, S., Lohmann, U., Feichter, J., Schulz, M., Timmreck, C., Ghan, S., Easter, R., Chin, M., Ginoux, P., Takemura, T., Tegen, I., Koch, D., Herzog, M., Penner, J., Pitari, G., Holben, B., Eck, T., Smirnov, A., Dubovik, O., Slutsker, I., Tanre, D., Torres, O., Mishchenko, M., Geogdzhayev, I., Chu, D. A., and Kaufman, Y.: Monthly averages of aerosol properties: A global comparison among models, satellite data, and AERONET ground data, J. Geophys. Res., 108, 4634, doi:10.1029/2001JD001 253, 2003.

Kirchstetter, T., Novakov, T., and Hobbs, P.: Evidence that the spectral dependence of light absorption by aerosols is affected by organic carbon, J. Geophys. Res., 109, D21 208, doi:10.1029/2004JD004 999, 2004.

Koepke, P., Hess, M., Schult, I., and Shettle, E.: Global Aerosol Data Set, Report 243, Max Planck Institute for Meteorology, Hamburg, iSSN 0937-1060, 1997.

Kohfeld, K. E. and Harrison, S. P.: DIRTMAP: the geological record of dust, Earth-Science Reviews, 54, 81–114, 2001.

Köhler, H.: Zur Kondensation von Wasserdampf in der Atmosphäre, Geofys. Publ., 2, 3–15, 1921.

Korhonen, P., Kulmala, M., Laaksonen, A., Viisanen, Y., McGraw, R., and Seinfeld, J. H.: Ternary nucleation of H_2SO_4, NH_3, and H_2O in the atmosphere, J. Geophys. Res., 104, 26 349–26 354, 1999.

Krüger, O. and Graßl, H.: The indirect aerosol effect over Europe, Geophys. Res. Lett., 29, 1925, doi:10.1029/2001GL014 081, 2002.

Krüger, O. and Graßl, H.: Albedo reduction by absorbing aerosols over China, Geophys. Res. Lett., 31, L02 108, doi:10.1029/2003GL019 111, 2004.

Kulmala, M.: How Particles Nucleate and Grow, Science, 302, 1000–1001, 2003.

Kulmala, M., Laaksonen, A., and Pirjola, L.: Parameterizations for sulfuric acid/water nucleation rates, J. Geophys. Res., 103, 8301–8307, 1998.

Kulmala, M., Kerminen, V., Anttila, T., Laaksonen, A., and O'Dowd, C. D.: Organic aerosol formation via sulphate cluster activation, J. Geophys. Res., 109, D04 205, doi:10.1029/2003JD003 961, 2004.

Langner, J. and Rhode, H.: A global three-dimensional model of the global sulfur cycle, J. Atmos. Chem., 13, 225–263, 1991.

Lelieveld, J., Berresheim, H., Borrmann, S., Crutzen, P. J., Dentener, F. J., Fischer, H., Feichter, J., Flatau, P. J., Heland, J., Holzinger, R., Korrmann, R., Lawrence, M. G., Levin, Z., Markowicz, K. M., Mihalopoulos, N., Minikin, A., Ramanathan, V., de Reus, M., Roelofs, G. J., Scheeren, H. A., Sciare, J., Schlager, H., Schultz, M., Siegmund, P., Steil, B., Stephanou, E. G., Stier, P., Traub, M., Warneke, C., Williams, J., , and Ziereis, H.: Global air pollution crossroads over the mediterranean, Science, 298, 794–799, doi:10.1126/science.1075457, 2002.

Lesins, G., Chylek, P., and Lohmann, U.: A study of internal and external mixing scenarios and its effect on aerosol optical properties and direct radiative forcing, J. Geophys. Res., 107, 4094, doi:10.1029/2001JD000 973, 2002.

Li, W. and Gao, J. X.: Acid deposition and integrated zoning control in China, Environmental Management, 30, 169–182, 2002.

Liepert, B. G., Feichter, J., Lohmann, U., and Roeckner, E.: Can aerosols spin down the water cycle in a warmer and moister world?, Geophys. Res. Lett., 31, L06 207, doi:10.1029/2003GL019 060, 2004.

Likens, G. E. and Bohrmann, F. H.: Acid rain: a serious regional environmental problem, Science, New Series, 184, 1176–1179, 1974.

Lin, H. and Leaitch, R.: Development of an in-cloud aerosol activation parameterization for climate modelling, in WMO Workshop on measurement of cloud properties for forcasts of weather, pp. 328–335, World Meteorological Organization, Geneva, 1997.

Lin, S. J. and Rood, R. B.: Multidimensional flux form semi-Lagrangian transport, Mon. Wea. Rev., 124, 2046–2068, 1996.

Liousse, C., Penner, J. E., Chuang, C., Walton, J. J., Eddleman, H., and Cachier, H.: A global three-dimensional model study of carbonaceous aerosols, J. Geophys. Res., 101, 19 411–19 432, 1996.

Lippmann, M.: Association of Particulate Matter Components with Daily Mortality and Morbidity in Urban Populations, HEI Research Reports 95, The Health Effects Institute, Boston, USA, available from: http://www.healtheffects.org, 2000.

Lohmann, U.: A glaciation indirect aerosol effect caused by soot aerosols, Geophys. Res. Lett., 29, 1052, doi:10.1029/2001GL014 357, 2002.

Lohmann, U. and Feichter, J.: Impact of sulfate aerosols on albedo and lifetime of clouds: A sensitivity study with the ECHAM4 GCM, J. Geophys. Res., 102, 13 685–13 700, 1997.

Lohmann, U. and Feichter, J.: Global indirect aerosol effects: a review, Atm. Chem. Phys. Discuss., 4, 7561–7614, sRef-ID: 1680-7375/acpd/2004-4-7561, 2004.

Lohmann, U. and Kärcher, B.: First interactive simulations of cirrus clouds formed by homogeneous freezing in the ECHAM general circulation model, J. Geophys. Res., 107, 4105, doi:10.1029/2001JD000 767, 2002.

Lohmann, U. and Roeckner, E.: Design and performance of a new cloud microphysics scheme developed for the ECHAM4 general circulation model, Clim. Dyn., 12, 557–572, 1996.

Lohmann, U., Feichter, J., Chuang, C. C., and Penner, J. E.: Predicting the number of cloud droplets in the ECHAM-GCM, J. Geophys. Res., 104, 9169–9198, 1999a.

Lohmann, U., von Salzen, K., McFarlane, N., Leighton, H. G., and Feichter, J.: Tropospheric sulfur cycle in the Canadian general circulation model, J. Geophys. Res., 104, 26 833–26 858, 1999b.

Lohmann, U., Kärcher, B., and Timmreck, C.: Impact of the Mount Pinatubo eruption on cirrus clouds formed by homogeneous freezing in the ECHAM4 GCM, J. Geophys. Res., 108, 4568, doi:10.1029/2002JD003 185, 2003.

Mahowald, N. and Luo, C.: A Less Dusty Future?, Geophys. Res. Lett., 30, 1903, doi:10.1029/2003GL017 880, 2003.

Maier-Reimer, E., P.Wetzel, Kriest, I., Jungclaus, J., and Botzet, M.: Effects of ocean biology on the penetrative radiation in a coupled climate model, J. Clim., submitted, 2005.

Maki, L. and Willoughby, K.: Bacteria as biogenic sources of freezing nuclei, Journal Of Applied Meteorology, 17, 1049–1053, 1978.

Marsland, S. J., Haak, H., Jungclaus, J. H., Latif, M., and Röske, F.: The Max-Planck-Institute global ocean/sea ice model with orthogonal curvilinear coordinates, Ocean Modelling, 5, 91–127, 2003.

Marti, J. J., Weber, R. J., McMurry, P. H., Eisele, F., Tanner, D., and Jefferson, A.: New particle formation at a remote continental site: Assessing the contributions of SO_2 and organic precursors, J. Geophys. Res., 102, 6331–6340, doi:10.1029/96JD02545, 1997.

Marticorena, B. and Bergametti, G.: Modeling the atmospheric dust cycle: 1. Design of a soil-derived dust emission scheme, J. Geophys. Res., 100, 16 415–16 430, 1995.

Martin, J. H. and Fitzwater, S. E.: Iron deficiency limits phytoplankton growth in the northeast Pacific subarctic, Nature, 331, 341–343, 1988.

Martonchik, J., Diner, D., Crean, K., and Bull, M.: Regional aerosol retrieval results from MISR, IEEE Trans. Geosci. Remote Sens., 40, 1520–1531, 2002.

Martonchik, J., Diner, D., Kahn, R., Gaitley, B., and Holben, B.: Comparison of MISR and AERONET aerosol optical depths over desert sites, Geophys. Res. Lett., 31, L16 102, doi:10.1029/2004GL019 807, 2004.

Mayol-Bracero, M.-O., Guyon, P., Graham, B., Roberts, G., Andreae, M., Decesari, S., Facchini, M., Fuzzi, S., and Artaxo, P.: Water-soluble organic compounds in biomass burning aerosols over Amazonia - 2. Apportionment of the chemical composition and importance of the polyacidic fraction, Journal Of Geophysical Research-Atmospheres, 107, 8091, doi:10.1029/2001JD000 522, 2002.

McCormic, R. A. and Ludwig, J. H.: Climate modifications by atmospheric aerosols, Science, 156, 1358–1359, 1967.

Metzger, S., Dentener, F., Pandis, S., and Lelieveld, J.: Gas/aerosol partitioning, 1, A computationally efficient model, J. Geophys. Res., 107, 4312, doi:10.1029/2001JD001 102, 2002.

Minikin, A., Petzold, A., Strom, J., Krejci, R., Seifert, M., van Velthoven, v. P., Schlager, H., and Schumann, U.: Aircraft observations of the upper tropospheric fine particle aerosol in the Northern and Southern Hemispheres at midlatitudes, Geophysical Research Letters, 30, 1503, doi:10.1029/2002GL016 458, 2003.

Mishchenko, M. I., Geogdzhayev, I. V., Cairns, B., Rossow, W. B., and Lacis, A. A.: Aerosol retrievals over the ocean by use of channels 1 and 2 AVHRR data: sensitivity analysis and preliminary results, Applied Optics, 38, 7325–7341, 1999.

Mlawer, E. J., Taubman, S. J., Brown, P. D., Iacono, M. J., and Clough, S. A.: Radiative transfer for inhomogeneous atmospheres: RRTM, a validated correlated-k model for the longwave, J. Geophys. Res., 102, 16 663–16 682, 1997.

Monahan, E., Spiel, D., and Davidson, K.: Oceanic whitecaps and their role in air-sea exchange, chap. A model of marine aerosol generation via whitecaps and wave disruption, pp. 167–174, D. Reidel, Norwell, Massachusetts, 1986.

Morcrette, J.-J., Clough, S. A., Mlawer, E. J., and Iacono, M. J.: Impact of a validated radiative transfer scheme, RRTM, on the ECMWF model climate and 10-day forecasts, ECMWF, Reading, UK, technical memorandum 252 edn., 1998.

Moulin, C., Dulac, F., Lambert, C. E., Chazette, P., Janowiak, I., Chatenet, B., and Lavenu, F.: Long-term daily monitoring of Saharan dust load over ocean using Meteosat ISCCP-B2 data, 2, Accuracy of the method and validation using Sun photometer measurements, J. Geophys. Res., 102, 16 959–16 969, 1997.

Murphy, D. M., Thomson, D. S., Middlebrook, A. M., and Schein, M. E.: In situ single-particle characterization at Cape Grim, J. Geophys. Res., 103, 16 485–16 491, 1998.

Nenes, A., Pandis, S. N., and Pilinis, C.: ISORROPIA: A new thermodynamic equilibrium model for multiphase multicomponent inorganic aerosols, Aquatic Geochemistry, 4, 123–152, 1998.

Nightingale, P., Malin, G., Law, C., Watson, A., Liss, P., Liddicoat, M., Boutin, J., and Upstill-Goddard, R.: In situ evaluation of air-sea gas exchange parameterizations using novel conservative and volatile tracers, Global Biogeochem. Cycles, 14, 373–387, 2000.

Nober, F., Graf, H., and Rosenfeld, D.: Sensitivity of the global circulation to the suppression of precipitation by anthropogenic aerosols, Global and Planetary Change, 37, 57–80, 2003.

Nordeng, T. E.: Extended versions of the convective parameterization scheme at ECMWF and their impact on the mean and transient activity of the model in the tropics, ECMWF, Reading, UK, technical memorandum edn., 1994.

O'Dowd, C. D., Aalto, P., Hämeri, K., Kulmala, M., and Hoffmann, T.: Aerosol formation: Atmospheric particles from organic vapours, Nature, 416, 497–498, 2002a.

O'Dowd, C. D., Jimenez, J. L., Bahreini, R., Flagan, R. C., Seinfeld, J. H., Hämeri, K., Pirjola, L., Kulmala, M., Jennings, S. G., and Hoffmann, T.: Marine aerosol formation from biogenic iodine emissions, Nature, 417, 632–636, 2002b.

O'Dowd, C. D., Facchini, M. C., Cavalli, F., Ceburnis, D., Mircea, M., Decesari, S., Fuzzi, S., Yoon, Y. J., and Putaud, J.-P.: Biogenically driven organic contribution to marine aerosol, Nature, 431, 676–680, 2004.

Okin, G., Mahowald, N., Chadwick, O., and Artaxo, P.: Impact of desert dust on the biogeochemistry of phosphorus in terrestrial ecosystems, Global Biogeochemical Cycles, 18, GB2005, doi:10.1029/2003GB002 145, 2004.

Olson, J.: World ecosystems (WE1.4): Digital raster data on a 10 minute geographic 1080 (2160 grid square), Global Ecosystem Database, Version 1.0: DISC A, edited by NOAA National Geophysical Data Center, Boulder, CO, 1992.

Penner, J. E., Andreae, M., Annegarn, H., Barrie, L., Feichter, J., Hegg, D., Jayaraman, A., Leaitch, R., Murphy, D., Nganga, J., and Pitari, G.: Climate change 2001: the scientific basis, chap. Aerosols, their direct and indirect effects, pp. 298–248, Cambridge University Press, 2001.

Pham, M., J.-F.Muller, Brasseur, G., Granier, C., and Megie, G.: A three-dimensional study of the tropospheric sulfur cycle, JGR, 100, 26 061–26 092, 1995.

Pruppacher, H. and Jaenicke, R.: The processing of water-vapor and aerosols by atmospheric clouds, a global estimate, Atmospheric Research, 38, 283–295, 1995.

Pruppbacher, H. R. and Klett, J. D.: Microphysics of clouds and precipitation, Kluwer Academic Publishers, 1997.

Putaud, J., van Dingenen, R., Baltensperger, U., Bruggemann, E., Charron, A., Facchini, M., Decesari, S., Fuzzi, S., Gehrig, R., H. H.-C., Harrison, R. M., Jones, A. M., Laj, P., Lorbeer, G., Maenhaut, W., Mihalopoulos, N., Müller, K., Palmgren, F., Querol, X., Rodriguez, S., Schneider, J., Spindler, G., ten Brink, H., Tunved, P., Torseth, K., Wehner, B., Weingartner, E., Wiedensohler, A., Wahlin, P., and Raes, F.: A european aerosol phenomenology, Report EUR 20411 EN, European Comission Joint Research Centre, Ispra, Italy, available from: http://carbodat.ei.jrc.it/ccu/, 2003.

Putaud, J., Raes, F., Van Dingenen, R., Bruggemann, E., Facchini, M., Decesari, S., Fuzzi, S., Gehrig, R., Huglin, C., Laj, P., Lorbeer, G., Maenhaut, W., Mihalopoulos, N., Müller, K., Querol, X., Rodriguez, S., Schneider, J., Spindler, G., ten Brink, H., Torseth, K., and Wiedensohler, A.: European aerosol phenomenology-2: Chemical characteristics of particulate matter at kerbside, urban, rural and background sites in Europe, Atmos. Environ., 38, 2579–2595, 2004.

Quaas, J., Boucher, O., and Bréon, F.-M.: Aerosol indirect effects in POLDER satellite data and the Laboratoire de Météorologie Dynamique-Zoom (LMDZ) general circulation model, J. Geophys. Res., 109, D08 205, doi:10.1029/2003JD004 317, 2004.

Raes, F., Dingenen, R. V., Vignati, E., Wilson, J., Putaud, J.-P., Seinfeld, J. H., and Adams, P.: Formation and cycling of aerosols in the global troposphere, Atmos. Environ., 34, 4215–4240, 2000.

Ramanathan, V., Crutzen, P. J., Kiehl, J. T., and Rosenfeld, D.: Aerosols, climate, and the hydrological cycle, Science, 294, 2119–2124, 2001.

Ramaswamy, V., Boucher, O., Haigh, J., Hauglustaine, D., Haywood, J., Myhre, G., Nakajima, T., Shi, G. Y., and Solomon, S.: Climate Change 2001: The Scientific Basis, Contribution of Working Group I to Third Assessment Report of the Intergovernmental Panel on Climate Change, chap. 6, Radiative forcing of climate change, pp. 349–416, Cambridge University Press, Cambridge, UK, 2001.

Rasch, P. J., Barth, M. C., Kiehl, J. T., Schwartz, S. E., and Benkovitz, C. M.: A description of the global sulfur cycle and its controlling processes in the National Center for Atmospheric Research Community Climate Model, J. Geophys. Res., 105, 1367–1386, 2000.

Ravishankara, A. R.: Heterogeneous and multiphase chemistry in the troposphere, Science, 276, 1058–1066, 1997.

Remer, L. A., , Tanré, D., Kaufman, Y. J., Ichoku, C., Mattoo, S., Levy, R., Chu, D. A., Holben, B., Dubovik, O., Smirnov, A., Martins, J. V., Li, R. R., and Ahmad, Z.: Validation of MODIS aerosol retrieval over ocean, Geophys. Res. Lett., 29, 8008, doi:10.1029/2001GL013 204, 2002.

Roderick, M. L. and Farquhar, D.: The cause of decreased pan evaporation over the past 50 years, Science, 298, 1410–1411, 2002.

Roeckner, E., Baeuml, G., Bonventura, L., Brokopf, R., Esch, M., Giorgetta, M., Hagemann, S., Kirchner, I., Kornblueh, L., Manzini, E., Rhodin, A., Schlese, U., Schulzweida, U., and Tompkins, A.: The atmospheric general circulation model ECHAM5. PART I: Model description, Report 349, Max Planck Institute for Meteorology, Hamburg, Germany, available from http://www.mpimet.mpg.de, 2003.

Roeckner, E., Brokopf, R., Esch, M., Giorgetta, M., Hagemann, S., Kornblueh, L., Manzini, E., Schlese, U., and Schulzweida, U.: The atmospheric general circulation model ECHAM5: Sensitivity of simulated climate to horizontal and vertical resolution, J. Clim., submitted, 2005.

Roelofs, G.-J., Lelieveld, J., and Ganzeveld, L.: Simulation of global sulfate distribution and the influence on effective cloud drop radii with a coupled photochemistry sulfur cycle model, Tellus B, 50, 224–242, 1998.

Rosenfeld, D.: TRMM Observed First Direct Evidence Of Smoke From Forest Fires Inhibiting Rainfall, Geophys. Res. Lett., 26, 3105–3108, 1999.

Rotstayn, L. D. and Penner, J. E.: Indirect aerosol forcing, quasi forcing, and climate response, J. Clim., 14, 2960–2975, 2001.

Saarnak, C. F.: A shift from natural to human-driven fire regime: implications for trace-gas emissions, Holocene, 11, 373–375, 2001.

Schaap, M., Gon, H. A. C. D. V. D., Dentener, F. J., Visschedijk, A. J. H., Loon, M. V., ten Brink, H. M., Putaud, J.-P., Guillaume, B., Liousse, C., and Builtjeses, P. J. H.: Anthropogenic black carbon and fine aerosol distribution over Europe, J. Geophys. Res., 109, D18 207, doi:10.1029/2003JD004 330, 2004.

Schnitzler, K.-G., Knorr, W., Schnur, R., Reick, C., Raddatz, T., and Roeckner, E.: The modular land surface vegetation framework 'JSBACH' coupled to the ECHAM5-GCM: A model study of physiological feedback processes under elevated atmospheric CO_2., J. Clim., submitted, 2005.

Schulz, M., Balkanski, Y. J., Guelle, W., and Dulac, F.: Role of aerosol size distribution and source location in a three dimensional simulation of a Saharan dust episode tested against satellite-derived optical thickness, J. Geophys. Res., 103, 10 579–10 592, 1998.

Schulz, M., de Leeuw, G., and Balkanski, Y.: Emission Of Atmospheric Trace Compounds, chap. Sea-salt aerosol source functions and emissions, pp. 333–359, Ed. Kluwer, 2004.

Seinfeld, J. H. and Pandis, S. N.: Atmospheric chemistry and physics: from air pollution to climate change, Wiley-Interscience, 1998.

Seinfeld, J. H., Carmichael, G. R., Arimoto, R., Conant, W. C., Brechtel, F. J., Bates, T. S., Cahill, T. A., Clarke, A. D., Doherty, S. J., Flatau, P. J., Huebert, B. J., Kim, J., Markowicz, K. M., Quinn, P. K., Russell, L. M., Russell, P. B., Shimizu, A., Shinozuka, Y., Song, C. H., Tang, Y. H., Uno, I., Vogelmann, A. M., Weber, R. J., Woo, J. H., and Zhang, X. Y.: ACE-ASIA - Regional climatic and atmospheric chemical effects of Asian dust and pollution, Bull. Am. Meteorol. Soc., 85, 367–380, 2004.

Shettle, E. P. and Fenn, R. W.: Models of the aerosols of the lower atmosphere and the effects of humidity variations on their optical properties, Tech. rep., Air Force Geoph. Lab., Massachusetts, project 7670, 1979.

Simmons, A. J. and Gibson, J. K.: The ERA-40 project plan, ERA-40 Project Report Series 1, ECMWF, Shinfield Park, Reading, UK, 2000.

Slinn, S. A. and Slinn, W. G. N.: Predictions for particle deposition on natural waters, Atmos. Environ., 14, 1013–1016, 1980.

Slinn, W. G. N.: Atmosphere-surface exchange of particulate and gaseous pollutants, chap. Dry deposition and resuspension of aerosol particles - a new look at some old problems, pp. 1–40, U. S. DOE Tech. Info. Center, Oak Ridge, TN, USA, 1976.

Slinn, W. G. N.: Predictions for particle deposition to vegetative canopies, Atmos. Environ., 16, 1785–1794, 1982.

Smith, M. and Harrison, N.: The sea spray generation function, J. Aerosol Sci., 29, 189–190, 1998.

Sokolik, I. N. and Toon, O. B.: Direct radiative forcing by anthropogenic airborne mineral aerosols, Nature, 381, 681–683, 1996.

Stier, P., Feichter, J., Kinne, S., Kloster, S., Vignati, E., Wilson, J., Ganzeveld, L., Tegen, I., Werner, M., Schulz, M., Balkanski, Y., and Boucher, O.: The aerosol-climate model ECHAM5-HAM, Atm. Chem. Phys. Discuss., 4, 5551–5623, 2004.

Stoddard, J. L., Jeffries, D. S., Lkewille, A., Clair, T. A., Dillon, P. J., Driscoll, C. T., Forsius, M., Johannessen, M., Kahl, J. S., Kellogg, J. H., Kemp, A., Mannio, J., Monteith, D. T., Murdoch, P. S., Patrick, S., Rebsdorf, A., and Skjelkv, B. L.: Regional trends in aquatic recovery from acidification in North America and Europe, Nature, 401, 575–578, 1999.

Stokes, R. H. and Robinson, R. A.: Interactions in aqueous nonelectolyte solutions. I. Solute-solvent equilibria, J. Phys. Chem., 70, 2126–2130, 1966.

Swap, R., Garstang, M., Greco, S., Talbot, R., and Kallberg, P.: Saharan dust in the amazon basin, Tellus B, 44, 133–149, 1992.

Takemura, T., Okamoto, H., Maruyama, Y., Numaguti, A., Higurashi, A., and Nakajima, T.: Tropospheric global three-dimensional simulation of aerosol optical thickness distribution of various origins, J. Geophys. Res., 105, 17 853–17 873, 2000.

Tang, I. N.: Thermodynamic and optical properties of mixed-salt aerosols of atmospheric importance, J. Geophys. Res., 102, 1883–1893, 1997.

Tanré, D., Kaufman, Y. J., Herman, M., and Mattoo, S.: Remote sensing of aerosol properties over oceans using the MODIS/EOS spectral radiances, J. Geophys. Res., 102, 16 971–16 988, 1997.

Taylor, K., Williamson, D., and Zwiers, F.: The sea surface temperature and sea-ice concentration boundary conditions for AMIP II simulations, PCMDI Report No. 60, Program for Climate Model Diagnosis and Intercomparison, Lawrence Livermore National Laboratory, Livermore, California, USA, 25 pp., 2000.

Tegen, I. and Lacis, A. A.: Modelling the particle size distribution and its influence on the radiative properties of mineral dust aerosol, J. Geophys. Res., 101, 19 237–19 244, 1997.

Tegen, I., Hollrig, P., Chin, M., Fung, I., Jacob, D., and Penner, J.: Contribution of different aerosol species to the global aerosol extinction optical thickness: Estimates from model results, J. Geophys. Res., 102, 23 895–23 915, 1997.

Tegen, I., Harrison, S. P., Kohfeld, K., Prentice, I. C., Coe, M., and Heimann, M.: Impact of vegetation and preferential source areas on global dust aerosol: Results from a model study, J. Geophys. Res., 107, 4576–4597, 2002.

Tegen, I., Werner, M., Harrison, S. P., and Kohfeld, K. E.: Relative importance of climate and land use in determining present and future global soil dust emission, Geophys. Res. Lett., 31, L05 105, doi:10.1029/2003GL019 216, 2004.

Tiedtke, M.: A comprehensive mass flux scheme for cumulus parameterization in large scale models, Mon. Wea. Rev., 117, 1779–1800, 1989.

Timmreck, C. and Schulz, M.: Significant dust simulation differences in nudged and climatological operation mode of the AGCM ECHAM, J. Geophys. Res., 109, D13 202, doi:10.1029/2003JD004 381, 2004.

Tompkins, A.: A prognostic parameterization for the subgrid-scale variability of water vapor and clouds in large-scale models and its use to diagnose cloud cover, J. Atmos. Sci., 59, 1917–1942, 2002.

Toon, O. B. and Ackerman, T. P.: Algorithms for the calculation of scattering by stratified spheres, Appl. Optics, 20, 3657–3660, 1981.

Torres, O., Bhartia, P., Herman, J., Sinyuk, A., and Holben, B.: A long term record of aerosol optical thickness from TOMS observations and comparison to AERONET measurements, J. Atmos. Sci., 59, 398–413, 2002.

Tsigaridis, K. and Kanakidou, M.: Global modelling of secondary organic aerosol in the troposphere: a sensitivity analysis, Atm. Chem. Phys., 3, 1849–1869, 2003.

Twomey, S.: Pollution and the planetary albedo, Atmos. Environ., 8, 1251–1256, 1974.

Twomey, S.: The Influence of Pollution on the Shortwave Albedo of Clouds, J. Atmos. Sci., 34, 1149–1152, 1977.

Unsworth, J., Wauchope, R., Klein, A., Dorn, E., Zeeh, B., Yeh, S., Akerblom, M., Racke, K., and Rubin, B.: Significance of long-range transport of pesticides in the atmosphere, Pure Appl. Chem., 71, 1359–1383, 1999.

van der Werf, G. R., Randerson, J. T., Collatz, G. J., and Giglio, L.: Carbon emissions from fires in tropical and subtropical ecosystems, Global Change Biology, 9, 547–562, 2003.

van Pul, W., de Leeuw, F., van Jaarsveld, J., van der Gaag, M., and Sliggers, C.: The potential for long-range transboundary atmospheric transport, Chemosphere, 37, 113–141, 1998.

Vehkamäki, H., Kulmala, M., Napari, I., Lehtinen, K. E. J., Timmreck, C., Noppel, M., and Laaksonen, A.: An improved parameterization for sulfuric acid water nucleation rates for tropospheric and stratospheric conditions, J. Geophys. Res., 107, 4622–4632, 2002.

Vignati, E., Wilson, J., and Stier, P.: M7: a size resolved aerosol mixture module for the use in global aerosol models, J. Geophys. Res., 109, D22 202, doi:10.1029/2003JD004 485, 2004.

Vink, S. and Measures, C.: The role of dust deposition in determining surface water distributions of Al and Fe in the South West Atlantic, Deep See Research, 48, 2782–2809, 2001.

West, J. J., Ansari, A. S., and Pandis, S. N.: Marginal $PM_{2.5}$: Nonlinear Mass Response to Sulfate Reductions in the Eastern United States, J. Air & Waste Manage. Assoc., 49, 1415–1424, 1999.

Whitby, E. R., McMurry, P. H., Shankar, U., and Binkowski, F. S.: Modal Aerosol Dynamics Modeling, Report 60013-91/020, U.S. Environmental Protection Agency, Research Triangle Park, NC, 27711, 1991.

Whitby, K. T.: The physical characteristics of sulfur aerosols, Atmos. Environ., 12, 135–159, 1978.

WHO: Health aspect of air pollution with particulate matter, ozone and nitrogen dioxide, http://www.euro.who.int, WHO Working Group Report, 2003.

Wiedinmyer, C., Guenther, A., Harley, P., Hewitt, N., Geron, C., Artaxo, P., Steinbrecher, R., and Rasmussen, R.: Emissions of Atmospheric Trace Compounds, chap. Global Organic Emissions from Vegetation, pp. 115–170, Kluwer Academic Publishers, Dordrecht, The Netherlands, 2004.

Wilemski, G.: Composition of the critical nucleus in multicomponent vapor nucleation, J. Chem. Phys., 80, 1370–1372, 1984.

Wilson, J., Cuvelier, C., and Raes, F.: A modelling study of global mixed aerosol fields, J. Geophys. Res., 106, 34 081–34 108, 2001.

WMO: Atmospheric Ozone: 1985, Report 16, Global ozone research and monitoring project, World Meteorological Organization, Geneva, Switzerland, chapter 15, 1986.

Wolf, M. E. and Hidy, G. M.: Aerosols and climate: Anthropogenic emissions and trends for 50 years, J. Geophys. Res., 102, 11 113–11 122, doi:10.1029/97JD00199, 1997.

Wurzler, S., Reisin, T., and Levin, Z.: Modification of mineral dust particles by cloud processing and subsequent effects on drop size distributions, J. Geophys. Res., 105, 4501–4512, 2000.

Zadanovskii, A. B.: New methods for calculating solubilities of electrolytes in multicomponent systems, Zhur. Fiz. Kim., 22, 1475–1485, 1948.

Zhang, J., Lohmann, U., and Stier, P.: A microphysical parameterization for convective clouds in the ECHAM5 climate model: 1. Single column model results evaluated at the Oklahoma ARM site, J. Geophys. Res., in print, 2004.

Acknowledgements

First and foremost I would like to thank my supervisors Dr. Johann Feichter and Prof. Dr. Hartmut Graßl for their constant support, for inspiring and teaching me, and for the interesting projects they involved me in. The positive spirit in the aerosol group made work fun.

The Max Planck Institute for Meteorology, and in particular Prof. Dr. Guy Brasseur in whose department Atmosphere in the Earth System this work was conducted, are thanked for giving me the opportunity to perform this study. It was a pleasure to work in this vivid and inspiring environment.

The support of the German Climate Research Project DEKLIM, of the International Max Research School on Earth System Modelling, and the Bucerius Zeit Stiftung is greatly acknowledged, as are the many fruitful co-operations within the EU project PHOENICS.

My sincere thanks includes all my colleagues, in particular Silvia Kloster and Stefan Kinne for their help and all the fun, as well as the rest of our group. Luis Kornblueh, Uwe Schulzweida, Monika Esch, and Andreas Rhodin (now at German Weather Service) are greatly thanked for helping me with the ECHAM environment. Many conversations with Erich Roeckner, Martin Schulz, Sebastian Rast, Rene Hommel, and Claudia Timmreck inspired my work.

For our good co-operation I would further like to thank Elisabetta Vignati, Julian Wilson, and Frank Dentener (Joint Research Centre of the European Commission, Ispra, Italy), Laurens Ganzeveld (Max Planck Institute for Chemistry, Mainz, Germany), and Ina Tegen and Martin Werner (Max Planck Institute for Biogeochemistry, Jena, Germany), Ulrike Lohmann and Junhua Zhang (ETH Zürich, Switzerland / Dalhousie University, Halifax, Canada), Olivier Boucher (CNRS, USTL, Villeneuve d'Ascq, France), as well as Michael Schulz and Ives Balkanski (Laboratoire des Sciences du Climat et de l'Environnement, Gif-sur Yvette, France).

Many thanks also to Beate Liepert from Columbia University as well as to Jim Hansen and Mike Mishchenko from the NASA Goddard Institute for Space Science, New York, USA, for hosting me for an inspiring research stay. This stay was made possible by a fellowship of the German Academic Exchange Service DAAD that is greatly acknowledged.

Further I am grateful to the Joint Research Centre of the European Commission, the Laboratoire des Sciences du Climat et de l'Environnement, the Dalhousie University, and the University of Sao Paulo for hosting me for research sojourns. The stay at the Laboratoire des Sciences du Climat et de l'Environnement was supported by the German-French scientific exchange program PROCOP.

Many thanks also to all my friends, in particular to Michael and Patrizia, Judith and Joachim, and Jan for all the wonderful distraction, but also for having been there when I needed it. Heide and Fritz are thanked for their support and great encouragement when I thought I am on the wrong track.

Last but not least sincere thanks to my parents Sabine and Jürgen, to my grandmother Momi, and to my sister Carolin and her husband Alex for their love and support on all levels.

MPI-Examensarbeit-Referenz:

Examensarbeit Nr. 1-79 bei Bedarf bitte Anfragen:
MPI für Meteorologie, Abtlg.: PR, Bundesstr. 53, 20146 Hamburg

Examensarbeit Nr. 80 November 2000	**Vertikalmessungen der Aerosolextinktion und des Ozons mit einem UV-Raman-Lidar** Volker Matthias
Examensarbeit Nr. 81 Dezember 2000	**Photochemical Smog in Berlin-Brandenburg: An Investigation with the Atmosphere-Chemistry Model GESIMA** Susanne E. Bauer
Examensarbeit Nr. 82 Juli 2001	**Komponenten des Wasserkreislaufs in Zyklonen aus Satellitendaten – Niederschlagsfallstudien-** Klepp Christian-Philipp
Examensarbeit Nr. 83 Juli 2001	**Aggregate models of climate change: development and applications** Kurt Georg Hooss
Examensarbeit Nr. 84 Februar 2002	**Ein Heterodyn-DIAL System für die simultane Messung von Wasserdampf und Vertikalwind: Aufbau und Erprobung** Stefan Lehmann
Examensarbeit Nr. 85 April 2002	**Der Wasser- und Energiehaushalt der arktischen Atmosphäre** Tido Semmler
Examensarbeit Nr. 86 April 2002	**Auswirkungen der Assimilation von Meereshöhen-Daten auf Analysen und Vorhersagen von El Niño** Sigrid Schöttle
Examensarbeit Nr. 87 Juni 2002	**Atmospheric Processes in a young Biomass Burning Plume - Radiation and Chemistry** Jörg Trentmann
Examensarbeit Nr. 88 August 2002	**Model Studies of the Tropical 30 to 60 Days Oscillation** Stefan Liess
Examensarbeit Nr. 89 Dezember 2002	**Influence of Sub-Grid Scale Variability of Clouds on the Solar Radiative Transfer Computations in the ECHAM5 Climate Model** Georg Bäuml
Examensarbeit Nr.90 Mai 2003	**Model studies on the response of the terrestrial carbon cycle to climate change and variability** Marko Scholze
Examensarbeit Nr.91 Juni 2003	**Integrated Assessment of Climate Change Using Structural Dynamic Models** Volker Barth

MPI-Examensarbeit-Referenz:

Examensarbeit Nr. 1-79 bei Bedarf bitte Anfragen:
MPI für Meteorologie, Abtlg.: PR, Bundesstr. 53, 20146 Hamburg

Examensarbeit Nr.92 Juli 2003	**Simulations of Indonesian Rainfall with a Hierarchy of Climate Models** Edvin Aldrian
Examensarbeit Nr.93 Juli 2003	**ENSO Teleconnections in High Resolution AGCM Experiments** Ute Merkel
Examensarbeit Nr.94 Juli 2003	**Application and Development of Water Vapor DIAL Systems** Klaus Ertel

---

Beginn einer neuen Veröffentlichungsreihe des MPIM, welche die vorherigen Reihen "Reports" und "Examensarbeiten" weiterführt:

„Berichte zur Erdsystemforschung" , „Reports on Earth System Science", ISSN 1614-1199
Sie enthält wissenschaftliche und technische Beiträge, inklusive Dissertationen.

Berichte zur Erdsystemforschung Nr.1 Juli 2004	**Simulation of Low-Frequency Climate Variability in the North Atlantic Ocean and the Arctic** Helmuth Haak
Berichte zur Erdsystemforschung Nr.2 Juli 2004	**Satellitenfernerkundung des Emissionsvermögens von Landoberflächen im Mikrowellenbereich** Claudia Wunram
Berichte zur Erdsystemforschung Nr.3 Juli 2004	**A Multi-Actor Dynamic Integrated Assessment Model (MADIAM)** Michael Weber
Berichte zur Erdsystemforschung Nr.4 November 2004	**The Impact of International Greenhouse Gas Emissions Reduction on Indonesia** Armi Susandi
Berichte zur Erdsystemforschung Nr.5 Januar 2005	**Proceedings of the first HyCARE meeting, Hamburg, 16-17 December 2004** Edited by Martin G. Schultz
Berichte zur Erdsystemforschung Nr.6 Januar 2005	**Mechanisms and Predictability of North Atlantic - European Climate** Holger Pohlmann
Berichte zur Erdsystemforschung Nr.7 November 2004	**Interannual and Decadal Variability in the Air-Sea Exchange of CO2 - a Model Study** Patrick Wetzel
Berichte zur Erdsystemforschung Nr.8 Dezember 2004	**Interannual Climate Variability in the Tropical Indian Ocean: A Study with a Hierarchy of Coupled General Circulation Models** Astrid Baquero Bernal


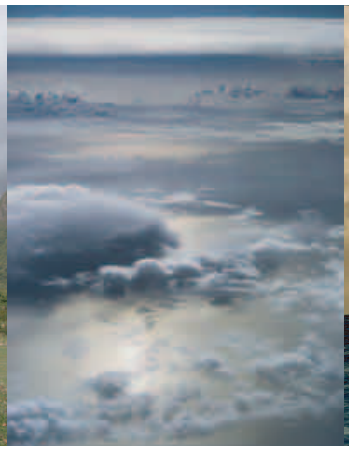


ISSN 1614-1199